UNIVERSITÀ DEGLI STUDI DI TRIESTE

XXIX CICLO DEL DOTTORATO DI RICERCA IN CHIMICA

Novel carbon nanostructured based materials for energy related catalysis and electrochemical sensing of small biomolecules

Settore scientifico-disciplinare: Chimica Organica

DOTTORANDA
Angela Giuliani

COORDINATORE
Chiar.mo Prof. Mauro Stener Mauro Stener

SUPERVISORE DI TESI
Chiar.mo Prof. Maurizio Prato

CO-SUPERVISORE DI TESI
Dr. Michele Melchionna

ANNO ACCADEMICO 2015/2016

To my grandmother Teresa

Abstract

The interest for carbon nanostructure-based hierarchical materials for electrochemical applications has been growing continuously in the last decade, from both an energy and sensing perspective. The use of carbon nanostructures is permitting to explore new opportunities in these research fields. Graphene, carbon nanotubes (CNTs) and single-walled carbon nanohorns (SWCNHs) can contribute to the design of revolutionary devices thanks to their special electronic and structural properties. This dissertation discusses the opportunity of carbon nanostructures integration into the assembly of hierarchical nanomaterials for electrochemical catalysis and electrochemical sensing applications. In particular, the major efforts have been focused in the use of SWCNHs due to their high purity, high conductivity, morphology and porosity, which can considerably aid to enhance performances. The hybrid materials have been synthetized using a hierarchical approach in order to achieve multicomposite-multifunctional nanomaterials able to orchestrate energy related processes such as O_2 reduction reaction (ORR) and CO_2 reduction reaction (CO_2RR) or allow specific H_2O_2 sensing. In particular, two catalytic systems named t-Fe@MWCNTs (featuring Fe-filled functionalized multi-walled carbon nanotubes) and g-N-SWCNHs (featuring N-doped graphitized carbon nanohorns) have been employed for the O_2 reduction reaction catalysis. On the other hand, ternary systems named Pd/TiO_2@ox-SWCNHs (integrating oxidized SWCNHs, Pd and TiO_2 in a precise hierarchical order) and NiCyclam@BMIM/p-SWCNHs (based on the heterogenization of molecular NiCyclam by embedding into pristine SWCNHs-supported ionic liquids) have been employed for the CO_2 reduction catalysis. Finally, a catalyst based on the coating of oxidized SWCNHs with CeO_2 (named ox-SWCNHs/CeO_2) has been employed for the catalysis of H_2O_2 reduction exploited for H_2O_2 amperometric sensing. In all cases, the nanocarbon scaffold may play a multi-role, facilitating electron transfer steps, bringing up specific textural properties, and contributing to physically adsorb gaseous reactants. The result is an enhancement of the catalytic performance in terms of activity, selectivity and stability, which has been communicated through publication (or in the process of being published) in peer-reviewed journals.

Table of contents

Chapter 1. Introduction 1

Chapter 2. Novel carbon nanostructured based hierarchical material as electrocatalysts for CO_2RR 29

CHAPTER 1: INTRODUCTION

1.1 Global energy challenges: The importance of CO_2 and O_2 reduction reactions

During the last century, the population growth and the economic rise following industrialization of countries such as India, China and Brazil, have represented the main contribution to the world energy consumption (WEC). At the end of 2008, the WEC was evaluated as 14TW, and projections have estimated that will reach 20TW by 2030 and it will be three times higher by the end of the century. (1)Up to now, the energetic demand increase has been related to the increase of fossil fuel consumption, which indeed supplies the 85% of the energy consumed, with important consequences for the environment and the living beings' life. The carbon dioxide (CO_2) evolved by the fossil fuels use is the main player of the greenhouse effect, and its rising concentration in the environment has been related to climate change (temperature increase) and environmental issues such as increasing of sea water acidity and gradual erosion of coral reef. (2) Given the imminent posed risk, the 2016 Paris Agreement on climate change has established strict rules for the decreasing of CO_2 emission, which is however still hard to achieve. The strategies to abate CO_2 levels in the atmosphere are based on the replacement of fossil fuels with renewable energy sources such as hydrogen, and the capture and stocking of CO_2 in permanent stocks (sandstone layer). (2) In this scenario, considering also that fossil fuels are non-renewable and in fast depletion, the great challenge for scientists is the research of a new strategy for the efficient exploitation of renewable and alternative energy sources, allowing a more sustainable development.

In this perspective, several efforts are made to obtain energy with negligible emission of CO_2. Two possible ways that have been subjected to many studies are:

a) Developing novel power source devices such as fuel cells (FCs);
b) Establishing a CO_2 neutral energy cycle based on the reduction of CO_2 (CO_2RR) to produce carbon fuels through a sustainable process, generally involving photocatalytic or electrocatalytic activations.

FCs are electrochemical energy devices that convert chemical energy into electricity. They consist of an electrochemical cell where an oxidation (of a certain fuel) and a reduction reactions simultaneously occur in two separate compartments, generating electron flow (i.e. electricity) between the two electrodes immersed in each compartment The two compartments are in contact through a membrane, which allows ions crossing. One of the typical reduction reaction exploited is the oxygen reduction reaction (ORR). During this thesis, the electrocatalytic ORR and the CO_2RR by heterogeneous nanostructured catalysts have been investigated. In addition, part of the focus of the thesis has been given to the preparation of electrosensors for a specific relevant molecule such as H_2O_2.

ORR is essential in the development of FCs, occurs in the cathodic compartment.

The reduction may lead to two different products: H_2O_2 or H_2O, depending on the number of the electrons involved, respectively $2e^-$ or $4e^-$, and it is a process generally occurring through a proton coupled electron transfer (PCET) mechanism. (3)

CO_2RR, as well as ORR, is a multi-electron process occurring generally through PCET, able to yield a range of different products, depending on the number of electrons participating in the reduction, which can span from 2 to 8. Hence, products such as CO and HCOOH are associated to a 2e- reduction, while CH_4 is formed through a 8e-reduction. HCOH and CH_3OH are respectively evolving by a 4 and 6-electron reduction. Moreover, more complex products rising from C-C coupling reactions can be also formed under certain conditions. (4)

Although there are a number of possible mechanisms for both ORR and CO_2RR, typically the reduction hinge on a first one-electron transfer, to form respectively O_2^- and $CO_2^{\bullet -}$. (4) (3)In both cases, the energetic barrier for such first electron transfer is very high, requiring an opportune catalyst.

The ideal electrocatalysts for both reactions share common specific features:

a) Being a gas/solid reaction, the catalyst must be able to adsorb selectively the substrate gas in order to increase the concentration of reactant around the active sites;
b) it must be selective towards a single reduction product;
c) it must be stable over long time usage;
d) it must be able to operate at low overpotentials;

Finally, an attractive feature is the ability to carry out the process in aqueous medium given the lower environmental impact.

In the present thesis, the establishment of novel nanostructured electrocatalysts (or sensors) for the two reactions has been explored. The design has been based on the use of a carbon nanostructure as active support, due to the outstanding properties of such nanomaterials which make them ideal candidates for electrocatalytic applications. A hierarchical concept has been applied for the synthesis of the new materials, which have resulted in the assembly of task-specific multicomponent catalytic systems.

1.2 Carbon nanostructures

During the last century, great advances on renewable and green energy technology have been reached, and carbon nanostructures have played an important role. Carbon nanostructures (CNSs) such as graphene (G), carbon nanotubes (CNTs),single walled carbon nanohorns (SWCNHs) and fullerene are characterized by fascinating mechanical, electronic, optical and thermal properties which can be fruitfully exploited in catalytic reactions. In particular, G, CNTs and SWCNHs, are considered promising candidates for materials applied for the development of transparent conductive films in solar cells, electrodes, supercapacitors and lithium batteries due to their high conductivity, which makes them competitive with metal based materials. (5)

1.2.1 Graphene

Although the present thesis has focused on the use of CNTs and SWCNHs as scaffolds, a few general concepts on graphene are presented, given that G can be considered from a structural point of view as the simplest CNS. Graphene was discovered by Novoselov and Geim using a micromechanical exfoliation method in 2004 (6), and thus far it is the thinnest and strongest material ever measured by the mechanic point of view. (7) G is a two dimensional (2D) allotrope of carbon, composed of a monolayer of carbon atoms arranged in a honeycomb of hexagonal ring. Conceptually, the others nanocarbon allotropes can be derived by G foils opportunely rolled up. (8) Figure 1.1 reports the rapresentation of a graphene sheet.

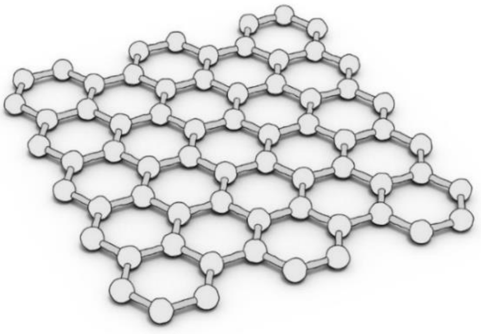

Figure 1.1 Graphene sheet representation

Apart from exfoliation methods (9), which at present affords graphene with lowest number of defects, there are a number of several other procedures:
a) epitaxial growth on insulating surface (such as SiC); (10)
b) By reduction of graphene oxide (GO) sheets, obtained by acid exfoliation treatment of graphite; (11)
c) or using a top-down method by unzipping CNTs obtaining graphene nanoribbons. (12)
Because of its outstanding properties, G has created a sensation among scientists, with number of publications exponentially growing. Thanks to the tensile strength and Young modulus, respectively 125 and ~1100 GPa, graphene appears an excellent component in the formulation of ultrastrong and composite material development. On the other hand, electrical conductivity and charge mobility $1x10^8$ S m^{-1} and $2x10^5$ cm^2 V^{-1} s^{-1}, respectively, render G interesting for electronic devices preparation. (13) In particular, novel materials for energy storage including lithium ion batteries and supercapacitors are a widely explored application for G-based materials, taking advantage of its high specific surface area. (14)
A great challenge for the application of G is the processing of great amount of graphene, given that it has a strong tendency to reaggregate via π-stacking of the layers, with concomitant deterioration of its properties. (15)This drawback, and the difficulties to obtain highly pure single graphene sheets, have slowed the application of G, favoring the research on others CNSs, such as CNTs and SWCNHs.

1.2.1.1. Chemical functionalization of graphene

G sheets can be functionalized by both covalent and non-covalent approaches.
Covalent functionalization can be obtained using several strategies, starting from pristine graphene:

a) Adding free radicals to sp^2 carbon atoms of graphene, heating diazonium salt, used by Tour and coworkers (16) (17) ;
b) Adding dienofiles to C-C bonds. Azomethine ylides, react through a 1,3 dipolar cycloaddition to form pyrrolidine rings (18). This type of functionalization has been also used to synthetize a variety of organic materials, including carbon nanotubes, which display interesting applications in several areas including biotechnology, nanoelectronic devices, drug delivery, and solar cells. (19) (20).

Alternatively, it is possible to use graphene oxide (GO), as starting material, which is graphene functionalized by oxygen containing groups (mainly carboxylic) and that can be handled more easily in liquid phase chemistry. A post modification can be effected by addition of molecules with amino or hydroxyls groups able to react with the carboxylic groups of the GO. Polymers functionalization uses this strategy: grafting of amino or hydroxyl-terminated polymers reacting with oxygen containing groups onto GO forming amide or ester bonds respectively. (21) (22) (23)
It must be noted, however, that GO does have significantly diminished electronic properties as compared to pristine graphene, due to the extensive damage of the polyaromatic pattern
G can also undergo covalent functionalization by attachment of hydrogen atoms or halogens atoms, giving graphane and fluorographene (graphene fluoride). (24) (25) It must be noted, however, that this type of functionalization also, severely disrupts the π-network, changing the characteristic properties: graphane and fluorographene are insulator materials because of the π-network breakage, with sp^2 carbons of graphene are rehybridized sp^3. (26) (27) The deterioration of the properties of graphene is in general deriving from the covalent functionalization, to different extent depending on the number of introduced functional groups.

Non-covalent functionalization involves π-interaction, which strength is determined by the combined effect of attractive forces and repulsive forces. In particular, π-π interactions, cation- π interactions and anion- π interactions have been investigated in depth playing a pivotal role for the self-assembly and supramolecular derived nanomaterials. (28) (29) Non-covalent functionalization preserves the aromatic structure and can result an effective strategy for the development of electrodic materials. However, the drawback is that detachment of the functional molecule can occur much more easily than a covalently linked group.

1.2.2. Carbon Nanotubes

CNTs were discovered in 1991 by Ijima, and since then, they have been used in several scientific areas, such as photovoltaics (30) (31) (32) integrated circuits (33) (34), biosensors (35) (36), nanomedicine (37) (38) (39) (40) (41) (42) and during the last period in catalysis, either alone, and as catalyst support (43) (44). They can be conceptually derived from rolling up graphene sheets into a tubular shape. Depending on the number of concentric cylindrical graphite layers, they can be classified as single walled carbon nanotubes (SWCNHs) and multi-wall carbon nanotubes (MWCNTs). Currently, the preparative methods of CNTs are arc discharge (45) (46) (47), chemical vapor deposition (CVD) (48) (49), high pressure carbon monoxide (HiPco) (50) (51), and laser ablation (52) (53), which afford medium-to-large scale production. Their mechanic and electronic properties are similar to those of G, making them a good alternative . However, as well as graphene, CNTs suffer from low solubility in the common solvents, they form bundles due to the van der Walls forces which are not easy to dismantle. A strategy to improve liquid phase dispersibility and processability is to carry out functionalization of the outer wall, which aids to unbundle and isolate individual tubes.

Unlike G, CNTs can also undergo endohedral functionalization, namely introduction of entities within their inner space, which present interesting additional features, related to the so called “confinement effect” (54).

1.2.2.1 Exohedral functionalization of CNTs

As for G, exohedral functionalization of CNTs can be distinguished into covalent and non-covalent.
Covalent functionalization, can influence and improve their dispersability and change their electronic properties cause of the π-network removal. The strategies more commonly used for CNTs functionalization are:

a) Oxidation treatment using mineral acids and reaction of the introduced carboxylic groups with amino or hydroxyl-functionalized organic molecules. However, this is an harsh procedure and can bring to the opening of the tips; (55) (56)
b) b) Functionalization by means of aryl-diazonium salts can introduce several different kind of organic molecules. (57) (58)
c) c) 1,3 dipolar cycloaddition of azomethyne ylides onto CNTs surface. This strategy allows to obtain useful building blocks for the construction of novel hybrids for nano- and bio-technological applications. (59) (60)

However, several other types of functionalization have been performed. (61) Non-covalent functionalization can be achieved taking advantage of π-π stacking, van der Walls forces, electrostatic force and wrapping interaction. (62) (63)Typically, small aromatic molecules such as pyrene can be readily stacked and if they are equipped with appropriate functionalities, they can be a platform for further more complex modification (64)

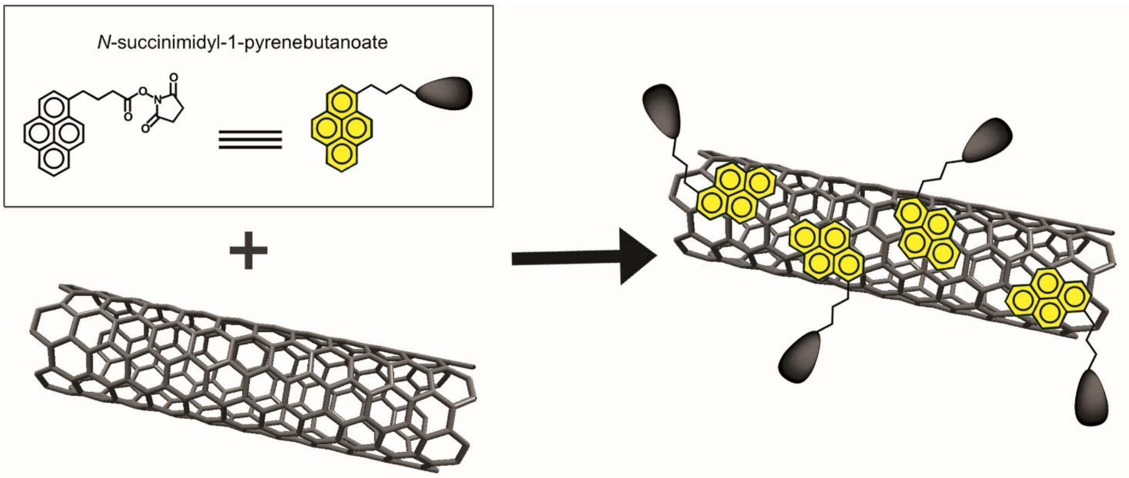

Figure 1.2 Reprinted with permission from M. Melchionna, M. Prato, *ECS J. Solid State Sci. Technol.***2013** *volume 2, issue 10,* ***M3040-M3045***). Copyright 2017, The Electrochemical Society.

For noncovalent functionalization the situation is similar to that of graphene. The advantages brought by a non-destructive type of modification, are counterbalanced by a less strong anchoring as compared to the covalent approach.

1.2.2.2 Endohedral functionalization of CNTs

A fascinating property owned by CNTs is the opportunity for an endohedral functionalization: catalytic species, such as metal nanoparticles, can fill the inner cavity of CNTs, experiencing what is known as confinement effect. (62) This strategy is particularly useful in catalysis, because the graphitic shell represented by CNTs scaffold, can provide protection for the metal particle avoiding leaching problems or selective poisoning. Nguyen et al. demonstrated that it is possible to modulate the filling yield between 10 and 80 % by controlling the CNT tip opening and exploiting the molecular recognition of the inner/outer surfaces by the metal molecular precursor. Moreover, they applied the hybrids obtained using Co, Ru and Pd for the hydrogenation reaction of cinnamaldehyde, finding that there was a clear correlation between the catalytic performances and the filling yields. (65) Several studies, investigated the particles' behavior confined inside or outside the CNTs, confirming the stark differences. As reported, the catalytic behavior of two hybrids based on conjugation of Pt and CNTs, with Pt nanoparticles inside the cavity or outside the cavity did not display equal performance. The effectiveness towards asymmetric hydrogenation of ethyl pyruvate in presence of chinconidine as a chiral modifier, when Pt nanoparticles were inside CNTs cavity exhibited TOF of 100 000 h^{-1} and an enantiomeric excess (ee) of 96%, while when Pt nanoparticles were attached to the outer wall, TOF of 15 000 h^{-1} and ee of 75% were obtained. (66) As reported by several other studies, (65) (66) (67) (68) metal nanoparticle inside the CNTs cavity showed diminished agglomeration tendency and increase of the catalytic effectiveness, with the CNTs basically acting as a nanoreactor. Other examples are available, spanning from classical Suzuki C-C couplings where the internalization of Pd resulted in diminished sintering of the nanoparticles (69) to production of etanol from syngas by endohedral Rh catalyst (70) .

Other than being a protecting shell, endohedrally modified CNTs can actively partecipate to the reaction, due to the π-network of the CNTs graphitic framework. Application in electrocatalysis have enjoyed particular success. The electronic comunication between the endohedral metal and the substrate involved in the electrocatalytic reaction adsorbed onto the outer graphene layer of the CNTs benefits from high charge mobility of the polyaromatic walls, improving the elctrocatalytic property. Deng et al.,reported a material based on Fe nanoparticles filling SWCNTs cavity able to catalyze the ORR in acidic media acting either as an electron shuttle than a protecting scaffold preventing the Fe leaching in acidic media. (71)

1.2.3 Single Wall Carbon Nanohorns

Recently, single wall carbon nanohorns (SWCNHS) have become the new rising star among the wide variety of nanocarbon materials, particularly in electrocatalytic applications. They structurally consist of single-graphene tubules (lengths: 2-5 nm) with highly strained conical ends (72). These nanostructures do not exist as discrete units. Assemblies of about 2000 SWCNHs form aggregates (diameters: 80-100nm), in which the SWCNHs protrude from the aggregate surface, or appear to develop a "spherical" particle. In the first case, the aggregates are called dahlia-like SWCNHs, in the second case the SWCNHs are called bud-like or seed-like. (73) (74)

SWCNHs are synthesized by CO_2 laser ablation of graphite under an argon gas flow at 760 Torr without the aid of metals catalysts, therefore their purity in terms of metals content is much higher than other CNSs. The pore size distribution of SWCNHs has been evaluated by combining nitrogen porosimetry measurements and molecular simulation techniques. The average internal pore radius of the tubular parts in SWCNHs is about 1.69–1.78 nm. The formation of aggregates leads to specific microposity and mesoporosity. They are expected to bring improved perfomances in the field of gas adsorption and separation due to their unique structures, distinctive nanoporosity and high surface-volume ratio. (75)

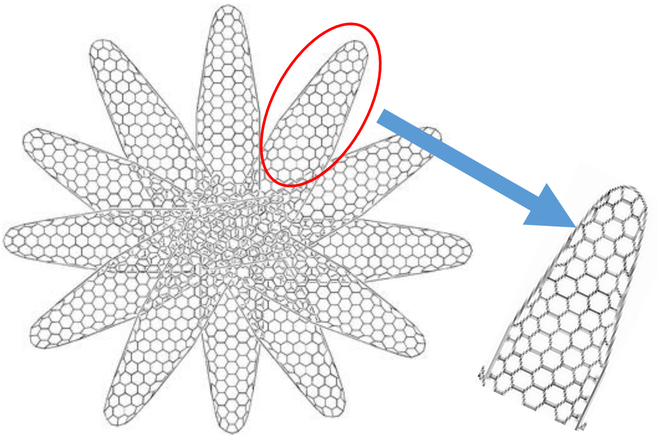

Figure 1.3. SWCNHs graphical representation

Inspection of HR-TEM images reveals that the end of the tubular part is closed by a horn-shaped tip with an apex angle of about 20°. The opening angle of the wedge, namely disclination angle, is $n\ (\pi/3)$ with $0 \leq n \leq 6$. The value of n is 0 for graphene foils, which is a two-dimensional structure, whereas for the cylindrical structures like nanotubes its value is 6. The other cone shaped graphite structures exhibit a value comprises between 0 and 6. In agreement with the Euler's rule, the terminating cap of a cone with a disclination angle $n\ (\pi/3)$, contains n pentagon rings in place of hexagonal rings allowing the conical shape. Hence, SWCNHs with an apex angle of 20° corresponding to $5\ (\pi/3)$ disclination, implies that all the nanohorns contain five pentagon rings near the tip. (76) By using a parametrized linear combination of atomic orbitals calculation Berber et al reported that the pentagon moieties can be placed along the cylinder mantle and at the apex of the tips, with no large difference in stability. The pentagon sites constitute defect sites for carbon nanohorns affecting also the material's electronic properties. Scanning tunneling microscopy (STM) showed a net excess of electrons on the pentagonal sites as compared to the hexagonal sites. (76) The features deriving from the pentagon moieties make this material interesting for the deriving chemical and the electronic properties.

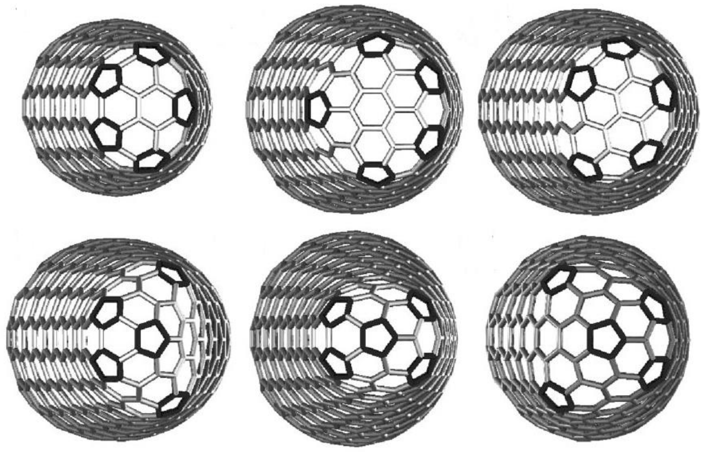

Figure 1.4 Detailed representation of SWCNHs tips: by the different position of pentagons moieties onto the tips of SWCNHs, six different and possible tips stem from. Reprinted with permission from Berber et al., Phy. Rev., 2000, B, 62, R2291. ©2000 American Physical Society

SWCNHs are finding application in every field of material science thanks to their easy chemical functionalization and physical properties.

1.2.3.1 Chemical functionalization of SWCNHs

The most common covalent chemical functionalization of SWCNHs can be achieved using the same strategies described above for G and CNTs:

a) The 1,3 dipolar cyclic addiction of azomethine leading to a large number of pyrrolidine was reported to preferentially occur in the vicinity of the tips, the more reactive sites; (77) (78)

b) Typical oxidation protocols, in particular oxygenated groups introduced by a mild oxidation treatment with diluted HNO_3. This second approach is useful when metals NPs or oxides need to be attached to the carbon nanostructure surface and in case of polymer grafting. (79) (73)

c) Aryl-diazonium functionalization is used to introduce substituted anilines, increasing the variety of functionalized nanomaterial achievable. (80) (78)

A different approach to functionalize SWCNHs with minimum degradation of their electronic properties is the non-covalent functionalization, performed by means of π-π stacking interactions between the side walls of SWCNHs with aromatic organic materials. As for CNTs, a typical unit exploited for this purpose is the pyrene molecules, which can in turn bear several functionalities, making possible post modification with other entities. However, supramolecular functionalization could be reversible, thus, less stable than the covalent one. (73)

1.3 Carbon nanostructures in electrocatalytic application

The advantageous electronic properties of carbon nanostructures such as graphene, CNTs, SWCNHs and other carbon allotropes make them interesting and important for the design of novel materials for electrochemical applications. Wide potential window and electrocatalytic activity for many redox reactions make them an alternative to metal modified electrodes. In comparison with the metal electrodes, they can also provide a platform for easy modification, supplying additional benefits for electrocatalysis and sensing.

1.3.1 Energy related application: CO_2RR features and state-of-the-art

CO_2 is at the basis of a paradox, being a double-faced coin with possible negative and positive impacts on society. In fact, while from an environmental point of view CO_2 is perceived as a dangerous molecule, from an economy perspective, it can be regarded as a potential largely available source of carbon for the synthesis of useful compounds. Electrochemical CO_2RR is a very appealing strategy for concomitantly reduce the CO_2 levels and access valuable carbon fuels, envisioned to lead to a new industrial concept for energy distribution. This new concept can be represented by a carbon neutral energy cycle. Electrochemical CO_2 reduction has the advantage that it may be an approach to utilize excess energy from intermittent renewable sources in lieu of large scale energy storage. (81)

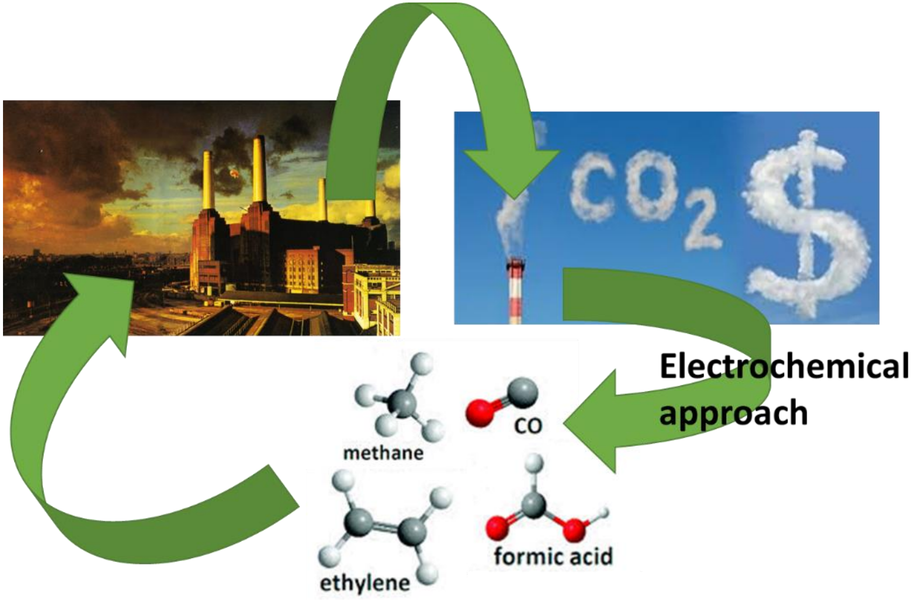

Figure 1.5. CO_2 recycle process

As mentioned above, CO_2 reduction reaction is a complex process, operated only by the nature with high performance. A proton source is normally needed to trig the process, and since the proton reduction occurs at potentials close to the CO_2 reduction reaction, the hydrogen evolution reaction (HER) is a competitive process. (4)

When the reaction is investigated in water, the pH can strongly affect the reactive pathway and the product selectivity. (4)

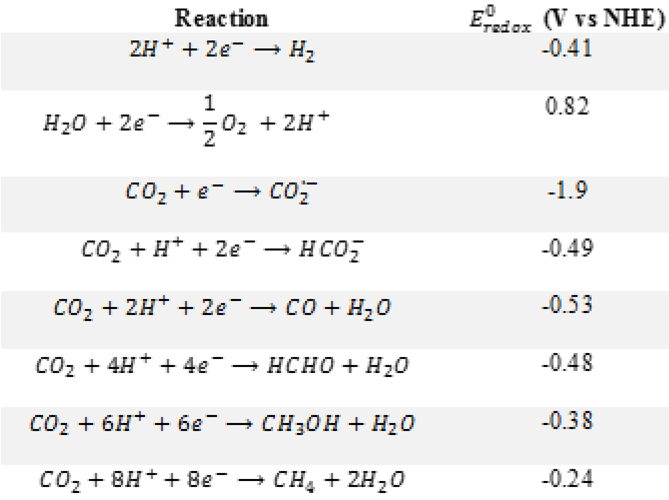

Reaction	E^0_{redox} (V vs NHE)
$2H^+ + 2e^- \rightarrow H_2$	-0.41
$H_2O + 2e^- \rightarrow \frac{1}{2}O_2 + 2H^+$	0.82
$CO_2 + e^- \rightarrow CO_2^{\cdot-}$	-1.9
$CO_2 + H^+ + 2e^- \rightarrow HCO_2^-$	-0.49
$CO_2 + 2H^+ + 2e^- \rightarrow CO + H_2O$	-0.53
$CO_2 + 4H^+ + 4e^- \rightarrow HCHO + H_2O$	-0.48
$CO_2 + 6H^+ + 6e^- \rightarrow CH_3OH + H_2O$	-0.38
$CO_2 + 8H^+ + 8e^- \rightarrow CH_4 + 2H_2O$	-0.24

Table 1.1. CO_2 reduction half-reactions

As table 1.1 shows above, the kind of product achievable depends on the number of the electrons involved during the reduction process. The catalyst nature is also of paramount importance, as it can crucially influence selectivity, as Hory et al. reported in a depth study on metal based electrocatalysts for CO_2 reduction. (82)
As a general rule, the catalysts can be distinguished in the following categories according to the typical product that they tend to yield:

a) metals that mainly form formic acid, HCOOH (Pb, Hg, In, Sn, Cd, Tl);
b) metals that mainly form carbon monoxide, CO (Au, Ag, Zn, Pd, Ga);
c) metals that form significant amounts of hydrocarbons such as methane and ethylene (Cu);
d) metals that mainly form H_2 (Pt, Ni, Fe, Ti).

Taking as example the formic acid, it can be produced with high faradaic efficiency using electrodes based on Pb and Hg, through a mechanism involving the formation of the mono-electronic reduction product $CO_2^{\cdot-}$. (82) (81)However, advances in catalysts design have allowed to synthetize and prepare new catalysts, bulk or molecular, based on other metals able to perform the conversion of CO_2 in HCOOH with low overpotentials and high FE. Berben et al, reported a Fe carbonyl cluster as molecular electrocatalyst for the reduction of CO_2 to formate in water with low applied potential, high current density and faradaic efficiency. (83) However, molecular catalysts present the drawback that product separation from the reacting medium without catalyst loss is difficult. Hod et al. reported heterogenization of a molecular catalyst based on a Fe-porphyrin-based metal-organic framework (MOF) films deposited onto ITO electrode for the reduction of CO_2 in DMF to CO and H_2 mixture with faradaic efficiency (FE)of ~100%, (41% in CO and 60% in H_2). The catalytic activity persisted over 5 hours. (84)
Min et al., investigated the catalytic properties of Pd/C electrodes as electrocatalyst for the reduction of CO_2 to formate in $NaHCO_3$, with high current density (80mA for mg of Pd), high faradaic efficiency (~90 %) and at low overpotentials. Pd/C produced CO as minor product, which poisoned the electrocatalyst during the electrolysis causing a decrease in current and FE in formate. They demonstrated that the catalyst was renewable keeping it for brief time in air, allowing the CO oxidation and restoring the

catalytic activity. (85) These results suggested that supported metal nanoparticles are more advantageous than heterogenized molecular catalyst such as the Fe-porphyrin based MOF because the former can be recycled over more catalytic cycles after a brief regeneration interval.

During the last decades, hierarchical synthetic strategy, found application in CO_2 electrocatalysis, due to the wide available surface, increase of selectivity, and in particular increase of catalytic system stability. In particular, Won et al., reported a hierarchical Tin dendrite electrode consisting of a multi-branched conifer-like structure with an enlarged surface area able to convert CO_2 to formate over 18 hours of experiments without any considerable catalytic degradation. It was demonstrated that CO_2 conversion selectivity on Sn electrodes was correlated to the native oxygen content at the subsurface, and the high oxygen content in the dendritic component of the hierarchical material was effective in $CO_2^{\cdot-}$ stabilization, a key intermediate for the formate production. (86)

Nowadays, due to the high fuels demand, the conversion of CO_2 to CH_4 and hydrocarbons is highly desirable. Up to now, the most promising catalysts for CH_4 and hydrocarbon production have been based on Cu catalyst. The key enabling the formation of hydrocarbons on Cu surface electrode is the protonation of adsorbed CO to form CHO. If adsorbed CHO is enough stable, the necessary overpotential to more efficient process to more than two electrons reduction products is lower. (87) However, there is still no full understanding of all the parameters involved in the CHO adsorption and the further reduction reactions. Studies have focused on the investigation of the effects of exposing different Cu crystal facets (88),on the local pH effects (89) (90); or local ion concentration, as well as the effect of surface coverage (87). Recently, particular attention has been devoted to the assembly and use of Cu catalyst structured at the nanoscale, which lead to improved characteristics toward CO_2 reduction. Sen et al. have reported the electrochemical reduction of CO_2 at a Cu-nanofoam characterized by hierarchical porosity. The high porosity and higher electroactive area of the material influenced the product distribution: the percentage FE in HCOOH was 26%, higher than the Cu smooth electrode (2%), while the concentration of methane and ethylene decreased in favor of propylene and ethane. (91) Following a similar concept, Roberts et al proposed copper nanocubes electrocatalysis with the ability to favor the conversion of CO_2 to multicarbon products, in particular ethylene, over methane. The high amount of (100) facets exposed and the roughness of the catalyst surface were responsible for such selectivity. (92) Obviously, studies have also been extended to metals other than copper, including both noble metal and earth abundant metals. Literature reported only few example of metal free catalysts based on carbonaceous materials, conductive polymers and non-metallic homogeneous catalysts. (93)

1.3.1.1 Carbon nanostructures application in CO_2RR

CNSs have been investigated either as metal free electrocatalyst and electrocatalysts support applied to CO_2RR catalysis. N-containing materials have gained growing interest, due to the natural affinity with CO_2, directly involved in CO_2 capture and concentration. Recently, Zhang et al., reported metal free N-doped carbon nanotubes (NCNTs), modified NCNTs with polyethylenimine (PEI) able to promote the CO_2 reduction to formate in aqueous medium at low potential (-1.2V vs Ag/AgCl). Their study demonstrated that NCNTs alone, can convert CO_2 to formate at -1.4V vs Ag/AgCl and PEI acted as a co-catalyst stabilizing the singly reduced intermediate and $CO_2^{\bullet -}$ and concentrating CO_2 in the PEI overlayer. (94). Similarly, Kumar et al. demonstrated the successful use of N-doped carbon nanofiber for CO_2 reduction to CO in ionic liquids. (95) However, the main use of carbon nanostructures, is as support for the active catalytic phases.

Maurin et al, demonstrated that CNTs can be used as scaffold for the non covalent attachment of a Fe porphyrin modified with a pyrene pendant, able to anchor by non-covalent interaction Fe porphyrin to the carbon surface. The Fe porphyrin itself had been previously reported (96), exhibiting good activity for the conversion of CO_2 to CO in organic solvent. After supporting it onto CNTs, the process in a neutral pH unbuffered water became viable, outweighing the concurrent water reduction, and entering in the short list of catalysts able to perform CO_2RR in aqueous medium with high efficiency, such as NiCyclam. (97) Kang et al., using a similar strategy, reported an iridium pincer dihydride catalyst supported on carbon nanotube surface. The catalyst had a pyrenic moiety enabling the anchoring on the carbon nanostructure by means of π-π stacking interactions. (98) These are successful examples of transfer of catalytic activity of a molecular catalyst onto a heterogenous system taking advantage of the reactive flexibility of carbon nanostructures. (99)

Nevertheless, the number of examples of molecular catalysts supported is still limited. In contrast, the supporting of metal oxide (100), or metal nanoparticle (101) (102) have enjoyed better fortune. In the context of supported nanoparticles or metal oxides for CO_2RR, carbon nanostructures have emerged as superior supporting phases. In the first instance, the CNSs guarantee a structural stabilization of the metal and aid a better dispersion of the nanoparticles, thus allowing lower loadings of metals.

Huan et al., reported a nanohybrid based on monodispersed gold nanoparticles on CNTs based electrode, anchored through a layer-by-layer method allowing a very little Au loading, reducing the catalyst cost, with high mass activity, and high faradaic efficiency, 70% of CO. (102)

Lu et al., performed the electroreduction of CO_2 to acetic acid and formic acid using a nanohybrid made by nanostructured Pd supported onto MWCNTs, finding that the interplay between Pd and carbon nanostructure phase was essential for the high efficiency of the CO_2 conversion. (103)

Liu et al. in end reported a novel system based on Pd-Cu NPs supported on N-doped graphene sheet. The bimetallic specie worked in synergy decreasing the CO_2 activation potential, suppressing the reaction of protons reduction and favoring the high selective conversion of CO_2 to formate using really low metals amount, 1% Pd and 2% Cu. (104)

In many cases, the CNSs play a more complex role than a simple physical stabilizer, facilitating the trafficking of electrons around the active phase. (71) (105)

1.3.2 Energy related application: ORR catalysis features and state-of-the-art

The ORR is one of the most studied reactions in electrochemistry. Originally, the interest in this reaction was merely focused on gaining deeper understanding of the cellular respiratory chain reactions mechanism. The reduction of O_2, as table 2 reports, can in general lead to two different products: H_2O_2 through a 2 electrons reduction and H_2O through a 4 electrons reduction reaction. (3) Over the years, this process has gained increasing interest in resonance with the rising and establishment of fuel cell devices, where it represent a crucial half reaction for many FC configurations. In addition, the reaction has been exploited for the selective electrochemical production of H_2O_2, an industrially relevant molecule. (106)

As for the CO_2RR, ORR is a very challenging process, proceeding through a PCET mechanism, too. Moreover, the rate of the proton transfer compared to the electron transfer rate can strongly affect the selectivity of the process. Indeed, it has been shown that the pH has a strong effect on the selectivity. (3)

Reaction	**E^0_{redox} (V vs NHE)**	
$O_2 + 4H^+ + 4e^- \longrightarrow 2H_2O$	1.229	**Acidic aqueous electrolyte solution**
$O_2 + 2H^+ + 2e^- \longrightarrow H_2O_2$	0.70	
$H_2O_2 + 2H^+ + 2e^- \longrightarrow 2H_2O$	1.76	
$O_2 + 2H_2O + 4e^- \longrightarrow 4OH^-$	0.401	**Alkaline aqueous electrolyte solution**
$O_2 + H_2O + 2e^- \longrightarrow HO_2^- + OH^-$	-0.065	
$HO_2^- + H_2O + 2e^- \longrightarrow 3OH^-$	0.867	

Table 1.2. O_2 reduction half-reactions in acidic and alkaline aqueous medium.

Tse et al. have highlighted how the control of proton transfer kinetic can affect the selectivity of the ORR. Using a lipid-modified electrode to tune the proton transport to the Cu-based ORR catalyst, they found that products such as H_2O_2 and O_2^- were generated from a mismatch between proton and electron transfer rates. Fast proton transfer favors H_2O_2 evolution, sluggish proton flux favors O_2^- formation. H_2O is produced when the proton transfer rate is comparable to the breaking rate of O-O bond. These findings support the necessity of a hierarchical design for this process in order to modulate the proton transfer rate and increase the selectivity towards only one product. (107)

At present, the state-of-the-art catalyst for ORR are based on precious metals, and in particular on Pt: the selective O_2 reduction to H_2O can be achieved using Pt/C, (108) (109) (110) while, the selective reduction of O_2 to H_2O_2 can be achieved using Pt-Hg nano-alloy. (111)

Pt/C catalysts for the selective reduction of O_2 to H_2O, in particular with E-TEK, Pt supported on carbon black, (108) (109) (110) is currently used as reference in most studies of O_2 reduction because it performs the best current (~5 mA cm^{-2}) at lowest potential (~0V vs Ag/AgCl) and high selectivity. However, it works only at basic pH (13-14), and large-scale commercial utilization is hindered by prohibitive cost of the Pt. Moreover, the catalyst suffers from poor durability and low tolerance to most fuel-impurities. (108) (109) (110)

Despite the H_2O_2 has traditionally been regarded as an undesirable product of the ORR, in the last decades scientists recognized an important opportunity to exploit the ORR for synthetic purposes, given the many industrial uses of H_2O_2. The current H_2O_2 manufacturing is mainly carried out by using the antraquinone process developed by BASF company. (112) However, such process involves a multistep sequence consisting of a hydrogenation step over Pd, followed by oxidation and extraction; therefore, it is an energy-demanding method, associated to low sustainability. An explored alternative is to directly combine H_2 and O_2 reaction onto Pd/C or Pd/Au at acidic pH, but this is a highly dangerous strategy due to the risk of explosion of H_2/O_2 gas mixture, which has to be maintained at specific percentage regimes, and considering the low yields of H_2O_2 (<30%). (113) (111) (114) (115) In this context, the electrocatalytic approach has emerged as a greener and more economically sustainable strategy considering the mild operating condition and the opportunity to generate H_2O_2 in aqueous medium.

There is only a handful of example of catalysts able to selectively drive ORR through a 2 electrons mechanism to yield H_2O_2.The selectivity is determined by the ability of the catalyst to split O-O bond preventing H_2O formation. The most successful catalysts are Co porphyrins and Pd-Au alloys. These catalysts are characterized by isolated sites of reactive atoms, surrounded by inert atoms, such as N, C and Au. These sites are unable to promote the breaking of O-O bond ensuring the high selectivity towards H_2O_2 evolution. (111)

Verdaguer-Casadevall et al., reported novel electrocatalysts consisting of Pd-Hg and Ag-Hg electrodes, designed using theoretical descriptors characteristics of ORR to H_2O_2. They found that the electrodeposition of Ag or Pd on Hg allowed the formation of isolated Ag or Pd atoms surrounded by Hg, which is inert towards the O-O bond breaking. Despite the high selectivity and the high yields in H_2O_2, these catalyst present high cost. Furthermore, the use of Hg is environmentally undesirable, compromising catalysts utilization in large-scale industrial setups. (111)

In order to avoid the employment of precious metals or environmentally unfriendly elements, scientists move their attention to new materials, based on either non-precious metals or on opportunely doped nanocarbons.

1.3.2.1 Carbon nanostructures application in ORR

The application of carbon nanostructures to ORR has been widely studied over recent years, with several examples with or without transition metals (TMs) reported research groups. (116) (117)

In the first instance, CNSs can be combined with metal components, to create hybrids or composites with improved performance toward ORR. Liang et al., employed N-doped graphene (N-G) as carbon nanoscaffold for nanostructured CoO_3 as ORR catalyst. CoO_3, is well known in literature as poor catalyst for ORR. However, supporting it on N-G, a high catalytic performance was achieved, taking advantage by the synergy between CoO_3 and the N-G electronic properties. (118)

Carbon nanostructures have been widely investigated as nanoscaffold for Pt nanoparticles by Wang et al.. They carried out a systematic study on the influence of the type of carbon nanoscaffold (amorphous carbon, CNTs and G) in relation to ORR activity. They found that activity of graphene based material was compromised by the fast stacking of G sheets, which locked the Pt-catalytic sites to O_2. The materials based on CNTs, instead, performed ORR with high-performance due to the tridimensional (3D) structure creating a porous architecture, increasing the contact between the catalytic sites and the O_2 gas molecules. (119)

Even if there are several studies regarding CNSs as ORR catalysts for H_2O formation, the examples selective for H_2O_2 are only a few. Literature reported mainly mesoporous materials obtained by pyrolysis of MOF based porous carbon nanostructure at higher temperature (120), or N-containing molecules supported onto silica NPs graphitized at high temperature. (121) These catalysts are able to produce H_2O_2 only in acidic environment with high faradaic efficiency.

From an applicative point of view, the opportunity to use totally metal free catalyst to perform ORR is of immense value. CNTs have been widely investigated as metal free catalysts for ORR showing very promising results. However, special care must be given, as CNTs are prepared using metals catalyst, and the electrocatalytic activity of the neat carbon nanostructures can be dependent on the presence of metals traces (i.e. Fe, Ni, Co, Mo). This aspect was demonstrated by Wang et al, who found that traces of metals elements in carbon nanotubes were responsible for the electrocatalytic activity towards the reduction of O_2 to H_2O (122).

As it appears, pure carbon catalysts are not efficient in catalyzing ORR. Doping of the carbon with heteroatom, particularly N, is instrumental to secure good selectivity and activity. N-doping can be achieved by means of several protocols: arc discharge, (123) laser ablation, (124) chemical vapor deposition (CVD) injection, (125) autoclave systems (126) and pyrolysis (127) are all viable methods introducing different levels and types of N atoms depending also on conditions. Among these methods, pyrolysis of N-containing organic molecules is the easiest procedure. Usually, the carbon nanostructure, used as nanoscaffold, reacts with a N-containing precursor, which forms upon high temperature in inert atmosphere a N-doped graphitic layer. The choice of the temperature to use is essential for the doping quality. N-doping can generate different types of N-species: a) graphitic N, pyridinic N, pyrrolic N, pyridonic N. All these N-species can affect in a different ways ORR catalysis, and many studies are being carried out to unravel the intimate role of the N atoms. Modern research trends have asserted that the catalytic properties of these materials towards O_2 activation is likely to be ascribed to the electron deficiency of the C atoms near the N moieties, attracting electrons from the anode and facilitating the ORR. (128) Overall, the modified band structure resulting from the N-doping lowers the work function at the C/O_2 interface as compared to undoped nanocarbons. (129) As mentioned before, the different types of N atoms have different ORR activity. Qu et al., reported a system based on polydopamine-graphene oxide derived N-doped mesoporous system for O_2 reduction to H_2O. They investigated the pyrolysis temperature and the thickness of the N-doped graphitic layer on the catalyst selectivity, demonstrating that higher temperatures decreased the N content with negative influence on the catalytic performance. On the other hand, using a temperature as high as 900°C the major part of pyridinic and pyrrolic N, which are not thermally stable, was converted to graphitic N, with positive effects on ORR catalysis, which became more selective towards water. (130) Other investigations, however, seem to point to pyridinic atoms as the most effective for ORR (131), and recently some studies have called into intervention the adjacent C-atoms (132). Another crucial factor affecting selectivity of N-doped nanocarbon catalysts is their porosity. The porosity of the material is strongly correlated with the conductivity of the catalyst, influencing also mass and electron transfer processes. (133) Another interesting feature of these materials is the high stability for long time experiment and to poisoning, unlike Pt/C catalyst. (130)

1.3.3 Sensing related application: H_2O_2 sensing state-of-the-art

As mentioned elsewhere, H_2O_2 is widely used in several factory manufacturing, such as food factory as sanitizing agent, water treatments, cosmetic and personal care, pharmaceutical and clinical products. H_2O_2 with concentration higher than 8% in weight are considered dangerous substances, in agreement with Global Harmonized System (GHS) and the European Commission regulation No. 1272/2008, and they must be handled correspondingly. H_2O_2 concentration in final products, such as food, must be absent, because it could change food flavor. While for cosmetic and personal care products it must not overcome concentration higher than 0.1% for oral hygiene products, and 12% in hair care product as bleaching agent. (134) For this reason, developing a fast and highly sensitive method for H_2O_2 detection is highly important. (135)

Several protocols have been developed for H_2O_2 detection, however the electrochemical approach, in comparison with the other procedures, is especially appealing because it is simple, rapid, sensitive, and cost effective. (136) (137) (138) (139) The detection of H_2O_2 by means electrochemical approach can occur through oxidation of H_2O_2 to O_2 or through the reduction process of H_2O_2 to H_2O. However, both these reactions carried out onto conventional solid electrodes, such as glassy carbon electrode (GCE), suffer from slow electrode kinetics and high overpotentials. (135) A great challenge in H_2O_2 detection is the underestimation or overestimation due to the interference of electroactive substances usually present in real samples including ascorbate, urate, glucose, paracetamol and bilirubin. (135) In order to improve the kinetics of the H_2O_2 sensing at the electrode surface and avoid interference issues, the design of novel electroactive materials has gained great interest.

For a long time, Ferric hexacyanoferrate, known as Prussian Blue (PB), has been used for H_2O_2 detection, due to its behaviour as “artificial peroxidase enzyme” able to perform H_2O_2 reduction with low overpotential. (140) (141) (142) Electrodes modified with PB have revealed high selectivity due to the particular polycrystalline structure which may allow the penetration of small molecules, including H_2O_2, while excluding larger molecules such as ascorbate. (140) (141) (142) (143) (144) Due to the particular features of PB, other metals hexacyanoferrates have been investigated showing performance comparable to PB. This class of compounds has been considered highly prominent due to the wide range of pH in which they can carry out the H_2O_2 detection. Importantly, the operation can be performed near neutral pH, making them a comfortable platform for enzyme modification and biosensors development. (128) (145) (146)

Biosensors development and the application of heme-protein, such as horseradish peroxidase (HRP), catalase (CAT), cytochrome c (Cyt c), hemoglobin (Hb), microperoxidase (MP) and myoglobin (Mb) for H_2O_2 sensing has been considered a promising approach because of the high selectivity towards H_2O_2. (147) (148)However, it is hard to establish direct electron transfer between protein and electrode surface as the active site of the redox enzyme is shielded into a polypeptide cavity, which severely affects the redox reaction kinetic. (149) (150) In additions, aspects such as costs, low stability over long time use and low stability due to denaturation have considerably slowed down the implementation of enzyme based systems, and moved the scientific efforts to non-enzymatic sensors based onto nanostructured metals and metals oxide.

(136) Enhancement of the direct electron transfer rate has been achieved through the use of precious metals based electrode, metal oxide or carbon nanostructure platforms, which are able to facilitate electron transfer. (151) (152) (153)

The employment of nano-sized TMs for electrosensing and electrocatalysis takes advantages of their ability to adopt different oxidation states, ability of absorb and activate molecules on their surface. (154) (155)Au nanoparticles have represented the benchmark catalyst for the electrochemical sensing of H_2O_2 for long time. (156) The change of nanosized Au morphology has been extensively investigated, and catalysts consisting of Au nanowires, (140) nanoporous Au, (157) Au nanocages (158) and Au nanoparticles (159), have been prepared and tested. The performance of Au nanocages and nanoporous Au have displayed better electrocatalytic properties compared with the other Au shapes. (157) (158) Apart from Au, other metals including Pt, (160) Cu, (161) (162) (163)Rh (147) (148) and Fe (164) have been investigated for the H_2O_2 sensing. Nano-alloys based on these metals have been prepared and investigated. Xiao et al. investigated Pt-Au nanoalloys and found an advantageous synergy between the metals . (165) In particular, Au favored the formation of Pt-OH species, moving the potential of the reduction of H_2O_2 to lower values, and increasing the sensitivity too. (166) (167)Metal oxides such as manganese oxide (168) (169), cobalt oxide, (170) titanium oxide, (171) copper oxide (172) (173) and iridium oxide (174) have also been screened as electrocatalysts for the detection of H_2O_2 working in particular for the oxidation of H_2O_2. A general problem with metal oxides, however, is that the operating potential is generally too high to be used in real samples, where interference issues become critical. (135) Despite all the advancements made in the field of electrocatalytic H_2O_2 detection, there are still several aspects to address for a real implementation. The required overpotentials to trig the H_2O_2 detection must be minimized, and the currents involved maximized; the cost of the electrocatalysts, especially in case of enzyme or precious metal based sensors, are economically unsustainable, and finally, the selectivity towards H_2O_2 detection must be very high, possibly with low limits of detection.

1.3.3.1 Carbon nanostructures application in H_2O_2 sensing

The surge of CNSs has also embraced the field of electrochemical sensors, and the sensing of H_2O_2. Zhou et al developed and reported a sensor made by chemically reduced graphene-oxide (CR-GO). CR-GO showed an increase of the electron transfer rate and shift of the onset potential of H_2O_2 oxidation to lower voltages. (175) The sensitivity of this system was higher than the systems based on carbon nanotubes previously reported (176) (135). The authors suggested that this behavior was due to the high density of edge-plane-like defective sites on graphene, providing several active centers for the electron transfer. (175)

Xu et al. carried out an interesting study on the effect of the N-doping of CNTs (NCNTs) in H_2O_2 sensor development. (177) They compared NCNTs with MWCNTs. NCNTs can yield a large number of defective sites on nanotube surfaces providing better electrocatalytic performances. (178) (179)

However, reported activities with metal free CNSs are until now still modest. The conjugation of CNSs with nanostructured metals and metal oxides, or with enzymes, has displayed a much enhanced performance. Niu's group reported a sensor based on Au nanoparticles dispersed in chitosan and supported on graphene. This material showed selectivity and reduction currents for H_2O_2 detection higher than the reference electrodes modified with graphene/chitosan, Au nanoparticles in chitosan or chitosan alone. This finding suggested that the electrocatalytic activity stemmed from the synergy between graphene and gold nanoparticles. (180) The role of CNSs is to boost the electron transfer rate between the catalytic sites and the electrode surface, while simultaneously preserving the nanoparticles from aggregation and thus extending stability and operation lifetimes. Carbon nanostructures, in particular G and CNTs, found also wide application in enzyme-based H_2O_2 amperometric sensors, due to their strong conductive properties, making them a functional platform able to trig the direct electron transfer from the electrode surface to the redox catalytic center of the enzymes. (135) In end the support of metal oxide such as MnO_2 (181), TiO_2 (182) on MWCNTs, displayed that the interplay between carbon nanostructure and nanostructured metal oxide were associated to an increase of sensitivity and to the shift of H_2O_2 detection potential at lower anodic potentials with concomitant increase of anti-interference properties. (135)

1.4 Motivation and research objectives

The interest for carbon nanostructure based hierarchical materials for electrochemical application has been growing continuously in last decade, from both an energy and sensing perspective. The use of carbon nanostructures is permitting to explore new opportunities in this research field. Graphene, CNTs and SWCNHs can contribute to the design of revolutionary devices thanks to their special electronic and structural properties.

The first objective of this research is develop novel electrocatalysts based on carbon nanostructures for use in the electrochemical activation of small molecules, in particular CO_2 and O_2. CO_2 and O_2 reduction reactions share several features: the general intervention of PCET mechanism, the low selectivity towards the products, and a high energetic barrier for the first electron transfer, which often isnecessary for the following cascade of catalytic events. Hence, the project embraces both synthetic and electrochemical work, and it is therefore structured in two distinct phases: 1) the synthesis and complete characterization of new materials; 2) the accurate evaluation of their potential in electrocatalytic CO_2RR and ORR.

The second objective of this research is develop an amperometric sensor for the detection of H_2O_2. Currently the amperometric detection of H_2O_2 is performed using precious metal based sensors or enzyme based sensors, which are respectively expensive and not stable over long time. The goal of this section is find a cheap, highly sensitive and fast sensor competitive with the state of art reported in literature.

1.5 The scope of the dissertation

This dissertation discusses the opportunity of carbon nanostructures application in hierarchical materials developing for electrochemical catalysis and electrochemical sensing applications. In particular, the major efforts have been focused in the development of hierarchical materials based on SWCNHs due to their specific properties: purity, high conductivity and porosity, which are fascinating for our purposes. Moreover, the electrochemical properties of Fe@MWCNTs have been studied within the SACS (Self-Assembly in Confined Spaces) project which gathers together different chemistry groups and with a common objective: the technologic advancing in the field of smart materials for energy application and phosphorescent devices manufacturing.

1.6 References

1. J. Barber. *Chem. Soc. Rev.,.* **2009**, Vol. 38, p. 185-196.

2. D. L. Damm., A. G. Federov,. *Energ. Conv. Menag.* **2008**, Vol. 49, p. 1674-1683.

3. W. Xing, G. Yin, J. Zhang,. *Rotating Electrode Methods and Oxygen Reduction Electrocatalysts.* s.l. : Elsevier, **2014**.

4. B. P. Sullivan. *Electrochemical and the Electrocatalytic Reducyion of Carbon Dioxide.* s.l. : ELSEVIER SCIENCE PUBLISHERS B.V., **1993**.

5. Z. Yang, J. Ren, Z. Zhang, X. Chen, G. Guan, L. Qiu, Y. Zhang, H. Peng,. *Chem. Rev.,.* **2015**, Vol. 115, p. 5159-5223.

6. K. S. Novoselov, A. K. Geim, S. Morozov, D. Jiang, Y. Zhang, S. Dubnos, I. Grigorieva, A. Firsov,. *Science,.* **2004**, Vol. 306, p. 666-669.

7. D. Chen, L. Tang, J. Li,. *Chem. Soc. Rev.,.* **2010**, Vol. 39, p. 3157-3180.

8. A. Geim, K. Novoselov,. *Nat. Nanomat.* **2007**, Vol. 6.

9. Y. Hernandez, . Nicolosi, M. Lotya, F. M. Blighe, Z. Sun, S. De, I. T. McGovern, B. Holland, M. Byrne, Y. K. Gun'Ko, J. J. Boland, P. Niraj, G. uesberg, S. Krishnamurthy, R. Goodue, J. Hutchinson, V. Scardaci, A. C. Ferrai, J. N. Colemann,. *Nat. Nanotech.,.* **2008**, Vol. 3, p. 563-568.

10. P. W. Sutter, J. I. Flege, E. A. Sutter,. *Nat. Mater.,.* **2008**, Vol. 7, p. 406-411.

11. D. A. Dikin, S. Stankovich, E.J. Zimney, R. D. Piner, G.H. Dommet, G. Evmeneko, S. T. Nguyen, R. S. Ruoff,. *Nat.* **2007**, Vol. 448, p. 457-460.

12. D. V. Kosynkin, A.L. Higginbotham, A. Sinitiskii, J. R. Lomeda, A. Dimiev, B. K. Price, J. M. Tour,. *Nat.* **2009**, Vol. 458, p. 872-876.

13. K. I. Bolotin, K. Sikes, Z. Jiang, M. Klima, G. Fundenberg, J. HOne, P. Kim, H. Stormer,. *Solid State Commun.,.* **2008**,, Vol. 146, p. 351-355.

14. M. D. Stoller, S. Park, Y. Zhu, J. An, R. S. Ruoff,. *Nano Lett.,.* **2008**, Vol. 8, p. 3498-3502.

15. H. C. Schniepp, J. Li, M. J. McAllister, H. Sai, M. Herrera-Alonso, D. H. Adamson,R. K. Prud'homme, R. Car, D.A. Saville, I. A. Aksav,. *J. Phys. Chem. B,.* **2006**, Vol. 110, p. 8535-8539.

16. D. V. Kosynkin, A. L. Higginbotham, A. Sinitsskii, J. R. Lomeda, A. Dimiev, B. K. Price, J. M. Tour,. *Nat.* **2009**, Vol. 458, p. 872.

17. A. Sinitskii, A. Dimiev, D.A. Corley, A. A. Fursina, D. V. Kosinkin, J. M. Tour,. *ACS NAno.* **2010**, Vol. 4, p. 1949.

18. M. Quintana, A. Lopez Montellano, S. Rapino, F. M. Toma, M. Iurlo, M. Carraro, A. Sartorel, C. Maccato, X. Ke, C. Bittencourt, T. Da Ros, G. Vn Tendeloo, M. Marcaccio, F. Paolucci, M. Prato, M. Bonchio,. *ACS Nano,.* **2013**, Vol. 7, p. 811.

19. V. Georgakilas, A. B. Bourlinos, D. Gournis, T. Tsoufis, C. Trapalis, A. M. Prato,. *J. Am. Chem. Soc.,.* **2008**, Vol. 130, p. 8733.

20. K. Kostaroles, L. Lacerda, G. Pastorin, W. Wu, S. Wiekowski, L. Luangsilivay, S. Godefroy, D. Pantarotto, J. P. Briand, S. Muller, M. Prato, A. Bianco,. *Nat. Nanothenol.,.* **2007**, Vol. 2, p. 108.

21. Y. Liu, J. Zhou, X. Zhang, Z. Liu, X. Wan, J. Tian, T. Wang, Y. Chen, *Carbon.* **2009**, Vol. 47, p. 3113.

22. C. E. Hamilton, J. R. Lorneda, Z. Sun, J. M. Tour,A. R. Barron,. *Nano Lett.,.* **2009**, Vol. 9, p. 3460.

23. Y. Cao, J. Feng, P. Wu,. *Carbon,.* **2010**,, Vol. 48, p. 1670.

24. J. O. Sofo, A. S. Chaudhari, G. D. Berber,. *Phys. Rev. B.* **2007**, Vol. 75, p. 153401.

25. V. Georgekilas, M. Otypka, A. B. Bourlinos, V. Chandra, N. Kim, K. C. Kemp, P. Hobza, R. Zboril, K. S. Kim,. *Chem. Rev.* **2012**, Vol. 112, p. 6156-6124.

26. R. R. Nair, W. C. Ren, R. Jalil, I. Riaz, V. G. Kravets, L. Britnell, P. Blake, F. Schedin, A. S. Mayorov, S. J. Yuan, M. I. Katnelson, H. M. Cheng, W. Strupinski, L. G. Bulusheva, A. V. Okotrub, I. V. Grigorieva, A. N. Grigorenko, K. Novoselov, A. Geim. *Small.* **2010**, Vol. 6, p. 2887.

27. V. Georgakilas, M. Otyepka, A.B. Bourlinos, V. Chandra, N. Kim, K. C. Kemp, P. Hobza, R. Zboril, K. S. Kim,. *Chem. Rev.* **2012**, Vol. 112, p. 6156-6214.

28. A.V. Okotrub, I. V. Grigorieva, A. N. Grigorenko, K. S. Novoselov, A. K. Geim. *Small.* **2010**, Vol. 6, p. 2887.

29. V. Georgakilas, M. Otyepka, A. B. Bourlinos, V. Chandra, N. Kim, K. C. Kemp,P. Hobza, R. Zboril, K. S. Kim,. *Chem. Rev.* **2012**, Vol. 112, p. 6156-6214.

30. L. M. Dai, D. W. Chang, J. B. Baek, W. Lu,. *Small.* **2012**, Vol. 8, p. 1130-1166.

31. S. Cataldo, P. Salice, E. Menna, B. Pignataro,. *Energ. Env. Sci.* **2012**, Vol. 5, p. 5919-5940.

32. A. J. Ferguson, J. L. Blackburn, N. Kopidakis,. *Materials Lett.,.* **2013**, Vol. 90, p. 115-125.

33. Z. Liu, L. Jiao, Y. Yao, X. Xian, J. Zhang,. *Adv. Mat.,.* **2010**, Vol. 22, p. 2285-2310.

34. P. Avouris. *Phys. Today.* **2009,** Vol. 62, p. 34-40.

35. Z. Chen, X. Zhang, R. Yang, Z. Zhu, Y. Chen, W. Tan,. *Nanoscale.* **2011**, Vol. 3, p. 1949-1956.

36. P.Barone, S. Baik , D.A. Heller, M. S. Strano. *Nat. Mat.* **2005**, Vol. 4, p. 86-92.

37. C. Fabbro, H. Ali-Boucetta, T. Da Ros, K. Kostarelos, A. Bianco, M. Prato,. *Chem.. Commun.* **2012**, Vol. 48, p. 3911-3926.

38. A. Fabbro, S. Bosi, L. Ballerini, M. Prato,. *ACS. Chem. NeuroSci.,.* **2012**, Vol. 3, p. 611-618.

39. A. Montellano, T. Da Ros, A. Bianco, M. Prato, M. *Nanoscale.* **2011**, Vol. 3, p. 4035-4041.

40. A. Bianco, K. Kostarelos, M. Prato,. *Chem. Commun.,.* **2011**, p. 10182-10188.

41. S. MArchesan, S. Bosi, A. Alshatwi, M. Prato,. *Nano Today,.* **2016**, Vol. 11, p. 398-401.

42. S. Usmani, E. R. Aurand, M. Medelin, A. Fabbro, D. Scaini, J. Laishram, F. B. Rosselli, A. Ansuini, D. Zoccolan, M. Scarselli, M. De Crescenzi, S. Bosi, M. Prato, L. Ballerini. *Sci. Adv.* **2011**, Vol. 2, p. e1600087.

43. M. Melchionna, S. Marchesan, M. Prato, P. Fornasiero,. *Catal. Sci. Technol.* **2015**, Vol. 5, p. 3859-3875.

44. G. Valenti, A. Boni, M. Melchionna, M. Cargnello, L. Nasi, G. Bertoni, R. J. Gorte, M. Marcaccio, S. Rapino, M. Bonchio, P. Fornasiero, M. Prato F. Paolucci,. *Nat. Commun.* **2016**, Vol. 2, p. 13549.

45. T. W. Ebbensen, P. M. Ajayan,. *Nat.* **1992**, Vol. 358, p. 220-222.

46. D. S. Bethune, C. H. Kiang, M. S. Vries, G. Gorman, R. Savoy, J. Vazquez, R. Beyers,. *Nat.* **1993**, Vol. 363, p. 605-607.

47. S. Iijima, T. Ichicashi. *Nat.* **1993**, Vol. 363, p. 603-605.

48. M. J. Yacaman, M. M. Yoshida, L. Rendon, J. G. Santiesteban. *Appl. Phys. Lett.* Vol. 62, p. 202-204.

49. M. Stadermann, S. P. Sherlock, J. B. In, F. Fornasiero, H. Gyu Park, A. B. Artyukhin, Y. Wang, J. J. Yoreo, C. P. Grigoropoulos, O. Bakajin, A.A. Chernov, A. Noy. *Nano Lett.* **2009**, Vol. 9, p. 738-744.

50. P. Nikolaev, M. J. Bronikowski, R. K. Bradley, F. Rohmund, D. T. Colbert, K. A. Smith, R. E. Smalley,. *Chem. Phys. Lett.* **1999**, Vol. 313, p. 91-97.

51. J. A. Isaac, A. Tanwani, M. L. Healy, L. J. Dahlben,. *J. Nanopart. Res.* **2010**, Vol. 12, p. 551-562.

52. C. Journet, W. K. Maser, P. Bernier, A. Loiseau, M. L. De La Chapelle, S. Lafrant, P. Deniard, R. Lee, J. E. Fisher,. *Nat.* **1997**, Vol. 388, p. 756-758.

53. T. Guo, P. Nikolaev, A. G. Rinzler, D. Tomanek, D. T. Colbert, R.E. Smalley,. *J. Phys. Chem.* **1995**, Vol. 99, p. 10694-10697.

54. X. Pan, X. Bao,. *Acc. Chem. Res.,.* **2011,** Vol. 44, p. 553-562.

55. J. Liu, A. G. Rinzler, H. Dai, J. H. Hafner,R. K. Bradley, P. J. Boul, A. Lu, T. Iverson, K. Shelimov, C. B. Huffman,. *Science,.* **2008**, Vol. 322, p. 1253-1256.

56. K. L. Klein, A. V. Melechko, T. E. McKnight, S. T. Retters, P.D. Rack, J. D. Fowlkes, D. C. Joy, M. L. Simpson. *J. Appl. Phys.* **2008**, Vol. 103, p. 061301.

57. B. K. Price, J. M. Tour,. *J. Am. Chem. Soc.,.* **2006**, Vol. 128, p. 12899-12904.

58. C. A. Dyke, J. M. Tour,. *J. Phys. Chem. A,.* **2004**, Vol. 108, p. 11151-11159.

59. N. Tagmatarchis, M. Prato,. *J. Mater. Chem.* **2004**, Vol. 14, p. 437-439.

60. D. Tasis, N. Tagmatarchis, A. Bianco, M. Prato,. *Chem. Rev.,.* **2006**, Vol. 106, p. 1105.

61. M. Melchionna, M. Prato,. Functionalization of carbon nanotubes. [aut. libro] Dominik Eder and Rbert Schlogl. *Nanocarbon-Inorganic Hybrids. Next Generation composite for sustainable energy applications.* s.l. : DeGruyter Publlishers, Berlin/Boston , **2014**.

62. B. Pan, B. Xing,. *Env. Sci. Technol.* **2008**, Vol. 42, p. 9005-9013.

63. Y. L. Zhao, J. F. Stoddart,. *Acc. Chem. Res.* **2009,** Vol. 42, p. 1161-1171.

64. M. Melchionna, M. Prato. *ECS J. Solid State Sci.,.* **2013**, Vol. 2, p. M3040-M3045.

65. T. Nguyen, P. Serp. *Chem. Cat. Chem.* **2013**, Vol. 5, p. 3595–3603.

66. Z. Chen, z. Guan, M. Li, Q. Yang, J. Zao, C. Li. *Angew. Chem. Int. Ed.,.* **2011**, Vol. 16, p. 4913-4917.

67. Ji Xiao, X Pan*, S Guo, P Ren, X Bao. *J. Am. Chem. Soc.* **2015**, Vol. 137, p. 477-482.

68. Y. Zing, X. Zheng, Y. Wu, M. Li, W. H. Zhang,C. Li. *Chem. Comm.* **2015**, Vol. 21, p. 8146-8149.

69. H. Liu, L. Zhang, N. Wang, D. S. Su,. *Angew. Chem. Int. Ed.,.* **2014**, Vol. 53, p. 12634-12638.

70. X. Pan, Z. Fan, W. Chen, Y. Ding, H. Luo, X. Bao,. *Nat. Mater.,.* **2007**, Vol. 6, p. 507-511.

71. D. Deng, L. Yu, X. Chen, G. Wang, L. Jin, X. Pan, J. Deng, G. Sun, X. Bao,. *Angew. Chem. Int. Ed.,.* **2013**, Vol. 52, p. 371-375.

72. S. Iijima, M. Yudasaka, R. Yamada, S. Bandow, K. Suenaga, F. Kokai, K. Takashi,. *Chem. Phys. Lett.* **1999**, Vol. 309, p. 165-170.

73. S. Zhu, G. Xu, *Nanoscale.* **2010**, Vol. 2, p. 2358-2549.

74. Z. Zhang, S. Han, C. Wang, J. Li, G. Xu, *Nanomat.* **2015,** Vol. 5, p. 1732-1755.

75. Furmaniak. *Phys. Chem. Chem. Phys.* **2013,** Vol. 16, p. 16468.

76. Berber et al. *Physical Rev.* **2000**, p. R2291-R2294.

77. N. Rubio, M. A. Herrero, M. Meneghetti, A. D. Ortiz, M. Schiavon, M. Prato, E. Vazquez, *J. Mater. Chem.,* **2009**, Vol. 19, p. 4407-4413.

78. S. Zhu, G. Xu, *Nanoscale,.* **2010**, Vol. 2, p. 2538-2549.

79. C. Cioffi, S. Campidelli, C. Sooambar, M. Marcaccio, G. Marcolongo, M. Meneghetti, D. Paoucci, F. Paolucci, C. Ehli, G. M. Aminur Rahman, V. Sgobba, D. M. Guldi, M. Prato, *J. Am.Chem. Soc.* **2007**, Vol. 129, p. 3938-3945.

80. C. Cioffi, S. Campidelli, C. Sooambar, M. Marcaccio, G. Marcolongo, M. Meneghetti, D. Paoucci, F. Paolucci, C. Ehli, G. M. Aminur Rahman, V. Sgobba, D. M. Guldi, M. Prato, *J.Am. Chem. Soc.* **2007**, Vol. 129, p. 3938-3945.

81. H. Jhong, S. Ma, P. J. Kenis,. *Current Opinion in Chemical engineering.* **2013**, Vol. 2, p. 191-199.

82. Y. Hori, H. Wakebe, T. Tsukamoto, O. Koga,. *Electrochimica Acta.* **1994**, Vol. 39, p. 1833-1839.

83. A. Teheri, E. J. Thompson, J. C. Fettinger, L. A. Berben,. ACS Catal., Vol. **2015,** p. 7140-7150.

84. I. Hod, M. D. Sampson, P. Deria, C.P. Kubiak, O.K. Fahra, J. T. Hupp,. *ACS Catal.,.* **2015**, Vol. 5, p. 6302-6309.

85. X. Min, M. W. Kanan,. *J. Am. Chem. Soc.,.* **2015**, Vol. 137, p. 4701-4708.

86. D. H. Wong, C. H. Choi, J. Chung, M. W. Chung, E. H. Kim, S. I. Woo. *Chem. Sus. Chem.* **2015**, Vol. 8, p. 3092-3098.

87. A. Peterson, F. Abild-Pedersen, F. Studt, J. Rossmeisl, J. K. Norskov. *Energy Environ. Sci.* **2010**, Vol. 3, p. 1311-1315.

88. Y. Hori, I. Takashi, O. Koga, N. Hoshi,. *J. Mol. Catal. A.* **2003**, Vol. 199, p. 39-47.

89. K. J. P. Schouten, E. Prez Gallent, M. T. M. Koper,. *J. Electroanal. Chem.,.* **2014**, Vol. 716, p. 53-57.

90. K. J. Schouten, Z. Qin, E Perez Gallent, M. T. M. Koper,. *J. Am. Chem. Soc.,.* **2012**, Vol. 134, p. 9864-9867.

91. Sen et al. *ACS Catal.,.* **2014**, Vol. 4, p. 3091-3095.

92. F. S. Roberts, K. P. Kuhl, A. Nilsson,. *Angew. Chem.INt. Ed.,.* **2015**, Vol. 54, p. 5179-5182.

93. C. Costentin, M. Robert, J. M. Savéant. *Chem. Soc. Rev.* **2013**, Vol. 42, p. 2423-2436.

94. S. Zhang, P. Kang, S. Ubnoske, M. K. Brennaman, N. Song, R. L. House, J. T. Glass, T. J. Meyer,. *J.Am. Chem.Soc.* **2014**, Vol. 136, p. 7845-7848.

95. B. Kumar, M. Asadi, D. Pisasale, S. Sinha-Ray, B. A. Rose, R. Haasch, J. Abiadde, A. L. Yarin, A. Salehi-Khojin. *Nat. Commun,.* **2013**, Vol. 4, p. 2819.

96. C. Costentin, S. Drouet, M. Robert, J. Saveant. *Science.* **2012**, Vol. 338, p. 90-94.

97. J. D. Frohelic, J. C. Kubiak,. *Inorg. Chem.* **2012**, Vol. 51, p. 3932-3934.

98. P. Kang, S. Zhang, T. J. Meyer, M. Brookhart. *Angew. Chem. Int. Ed.* 2**014,** Vol. 53, p. 8709-8713.

99. A. Maurin, M. Robert,. *J. Am. Chem. Soc.* **2016**, Vol. 138, p. 2492-2495.

100. R. Zhang, W. Lu, G. Li, L.Lei,. *Mater. Lett.* **2015**, Vol. 141, p. 63-66.

101. Y. Koo, R. Malik, N. Alvarez, L. White, V. S. Shanov, M. Schulz, B. COllins, J. Sankar, Y. Yun,. *RSC Adv.* **2014**, Vol. 4, p. 16362-16367.

102. T. N. Huan, P. Prakash, P. Simon, G. Rousse, X. Xu, V. Artero, E. Gravel, E. Doris, M. Fontcave,. *Chem. Sus. Chem.,.* **2016**, Vol. 9, p. 2317-2320.

103. G. Lu, H. Wang, Z. Bian, X. Liu,. *Sci. World J.* **2013**, p. 424617.

104. X. Liu, L. Zhu, H. Wang, G. He, Z. Bian. *RCS Adv.* **2016**, Vol. 6, p. 38380-38387.

105. M. V. Bracamonte, M. Melchionna, A. Stopin, A. Giuliani, C. Tavagnacco, Y. Garcia, P. Fornasiero, M. Prato, D. Bonifazi. *Chem Eur. J.* **2015**, Vol. 21, p. 12769 – 12777.

106. C. Song, J. Zhang,. *PEM Fuel Cell Electrocatalysts and Catalysts Layers.* s.l. : Springer London, **2008**.

107. Tse et al. *Nat.,.* **2016**, Vol. 15, p. 754-759.

108. F. Jaouen, E. Proietti, M. Lefevre, R. Chenitz, J. P. Dodolet, G. Wu, H. T. Chung, C. M. Johnston, P. Zelenay,. *Energy Environ. Sci.* **2011**, Vol. 4, p. 114-130.

109. M. Winter, R. J. Brodd,. *Chem. Rev.* **2004**, Vol. 104, p. 4245-4269.

110. S. C. Thomas, X. Ren, S. Gottesfeld, P. Zelenay,. *Electrochim. Acta.* **2002**, Vol. 47, p. 3741-3748.

111. A. Verdaguer-Casadevall et al. *Nano Lett.* **2014**, Vol. 14, p. 1603-1608.

112. G. Goor, J. Glennesberg, S. Jacobi,. *Ulmann's Encyclopedia of Industrial Chemistry.* s.l. : Weinheim:Wiley-VCH, **2007**.

113. I. Yamada, T. Onizawa, S. Takenaka, K. Otzuka,. *Angew. chem. Int. Ed.,.* **2003**, Vol. 42, p. 3653-3655.

114. Y. Izumi. *US Patent4009252.* **1978**.

115. L. W. Gosset. *US Patent 4681751.* **1988**.

116. H. T. Chung, J. H. Wong, P. Zelenay. *Nat. Commun.* **2013**, Vol. 4, p. 1922.

117. X. Zao et al. *Adv. Funct. Mat.* **2017**, Vol. 10.1002/adfm.201605717.

118. Liang et al. *Nat. Mater.,.* **2011**, Vol. 10, p. 780.

119. J. Liu, C. T. Liu, L. Zhao, J. J. Zhang, L. M. Zhang, Z. B. Wang. *Interanational Journal of Hydrogen Energy.* **2016,** Vol. 41, p. 1859-1870.

120. Liu et al. *Angew. Chem. Int. Ed. .* **2015.**

121. *J. Am. Chem. Soc.,* **2012**,

122. Wang et al. *Angew. Chem. Int. Ed.,.* **2013**, Vol. 52, p. 13818-13821.

123. N. Li et al. *Carbon.* **2010,** Vol. 48, p. 255-259.

124. Guo et al. *Adv. Opt. Mater.* **2014**, Vol. 2, p. 120-125.

125. Weiet al. *Nano Lett.,.* **2009**, Vol. 9, p. 1752-1758.

126. Qu et al. *Sci. rep.* **2014**, Vol. 4, p. 5294.

127. Czerw et al. *Nano Lett.,.* **2001**, Vol. 1, p. 457-460.

128. D. S. Yu, Q. Zhang, L. M:. Dai,. *J. Am. Chem. Soc.,.* **2010**, Vol. 132, p. 15127.

129. S. Zhu, G. Xu,. *Nanoscale.* **2010**, Vol. 2, p. 2358.

130. K. Qu, Y. Zheng, S. Dai, Z. Qiao,. *Nano Lett.,.* **2013**.

131. G. Tuci, C. Zafferoni, P. D'Ambrosio, S. Caporali, M. Ceppatelli, A. Rossin, T. Tsoufis, M. Innocenti, G. Giambastiani, *ACS Catal.,.* **2013**, Vol. 3, p. 2108-2111.

132. D. Guo, R. Shybuya, C. Akiba, S. Saji, T. Kondo, J. Nakamura, *Science.* **2016**, Vol. 351, p. 361-365.

133. H. Yu, L. Shang, T. Bian, R. Shi, G. I. N. Waterhouse, Y. Zhao, C. Zhiu, L. Z. Wu, C. H. Tung, T. Zhang,. *Adv. MAter.* **2016**, Vol. 28, p. 5080.

134. http://www.cosmeticsinfo.org/ingredient/hydrogen-peroxide-0. [Online]

135. W. Chen, S. Cai, Q. Ren, W. Wen, Y. Zhao. *Analyst.* **2012**, Vol. 137, p. 49-58.

136. M. V. Bracamonte, M. Melchionna, A. Giuliani, L. NAsi, C. Tavagnacco, M. Prato, P. fornasiero. *Sens. Act. B.* **2017**, Vol. 239, p. 923-932.

137. A.L. Hu, Y.H. Liu, H.H. Deng, G.L. Hong, A.L. Liu, X.H. Lin, X.H. Xia, W. Chen,. *Biosen. Bioelectron.* **2014**, Vol. 61, p. 374-378.

138. Y.B. Tsaplev. *J. Anal. Chem.* **2012**, Vol. 67, p. 506-514.

139. H.A. Khorami, J.F. Botero-Cadavid, P. Wild, N. Djilali,. *Electrochim. Acta.* **2014**, Vol. 115, p. 416-424.

140. Karyakin, A. A. *Electroanalysis.* **2001,** Vol. 13, p. 813-819.

141. A. A. Karyakin, E. E. Karyakina and L. Gorton,. *Anal. Chem.* **2000**, Vol. 72, p. 1720-1723.

142. A. A. Karyakin, E. E. Karyakina and L. Gorton. *Talanta.* **1996**, Vol. 43, p. 1597-1606.

143. Palleschi, F. Ricci and G. *Biosens. Bioelectron.* **2005**, Vol. 21, p. 389-407.

144. Koncki, R. *Crit. Rev. Anal. Chem.,* **2002**, Vol. 32, p. 79-96.

145. R. Garjonyte and A. Malinauskas. *Sens. Act. B.* **1999**, Vol. 56, p. 93-97.

146. S. Milardovic, I. Kruhak, D. Ivekovic, V. Rumenjak, M. Tkalcec. *Anal. Chim. Acta,.* **1997**, Vol. 350, p. 91-96.

147. M. C. Rodriguez and G. A. Rivas. *Anal. Lett.,***.** **2001**, Vol. 34, p. 1829-1840.

148. S. A. Miscoria, G. D. Barrera and G. A. Rivas. *Sens. Actuators B.* **2006**, Vol. 115, p. 205-211.

149. Gorton, L. *Electroanalysis.* **1995**, Vol. 7, p. 23-45.

150. L. Gorton, A. Lindgren, T. Larsson, F. D. Munteanu, T. Ruzgas. *Anal. Chim. Acta.* **1999**, Vol. 400, p. 91-108.

151. Y. Wang, X. Ma, Y. Wen, Y. Xing, Z. Zhang and H. Yang,. *Biosens. Bioelectron.* **2010**, Vol. 25, p. 2442-2446.

152. Y. Z. Xian, F. H. Wu, J. J. Xu, Y. Tian, Z. C. Hu, L. W. Wang and. *Biosens. Bioelectron.* **2008**, Vol. 24, p. 198-203.

153. S. L. Luo, X. D. Zeng, X. F. Li, X. Y. Liu, Y. Liu, B. Kong,. *Biosens. Bioelectron.* **2009**, Vol. 25, p. 896-900.

154. I. Lee, J. Lu, I. Do, L. T. Drzal and R. M. Worden. *ACS Nano.* **2008**, Vol. 2, p. 1825-1832.

155. J. H. T. Luong, S. Hrapovic, Y. L. Liu and K. B. Male. *Anal.Chem.* **2004**, Vol. 76, p. 1083.

156. S. Guo, D. Wen, S. Dong and E. Wang,. *Talanta.* **2009**, Vol. 77, p. 1510-1517.

157. J. G. Liu, F. H. Meng, X. L. Yan, J. Gu and Z. G. Zou. *Electrochim. Acta,.* **2011**, Vol. 56, p. 4657-4662.

158. Y. Zhang, Y. Sun, Z. Liu, F. Xu, K. Cui, Y. Shi, Z. Wen and Z. Li,. *J. Electroanal. Chem.,.* **2011**, Vol. 656, p. 23-28.

159. R. Ramaraj and G. Maduralveeran. *J. Electroanal. Chem.* **2007**, Vol. 608, p. 52-58.

160. S. A. Miscoria, G. D. Barrera and G. A. Rivas,. *Electroanalysis.* **2002**, Vol. 14, p. 981-987.

161. M. C. Rodriguez and G. A. Rivas. *Anal. Lett.* **2000**, Vol. 33, p. 2373-2389.

162. Rivas, M. C. Rodriguez and G. A. *Electroanalysis.,.* **2001**, Vol. 13, p. 1179-1184.

163. G. L. Luque, N. F. Ferreyra and G. A. Rivas. *Microchim. Acta,.* **2006**, Vol. 152, p. 277-283.

164. F. N. Comba, M. D. Rubianes, P. Herrasti and G. A. Rivas,. *Sens. Actuators. B.* **2010**, Vol. 149, p. 306-309.

165. F. Q. Zhao, F. Xiao, Y. F. Zhang, G. P. Guo and B. Z. Zeng,. *J. Phys. Chem. C.* **2009**, Vol. 113, p. 849-855.

166. P. Hernandez-Fernandez, S. Rojas, P. Ocon, J. L. GomezdelaFuente, J. SanFabian, J. Sanza, M. A. Pena, F. J. Garcia-Garcia, P. Terreros and J. L. G. Fierro,. *J. Phys. Chem. C.* **2007**, Vol. 111, p. 2913-2923.

167. S. J. Dong, S. J. Guo and E. Wang,. *J. Phys. Chem. C.* **2008**, Vol. 112, p. 2389-2393.

168. Y. H. Lin, X. L. Cui and L. Y. Li,. *Electrochem. Commun.,.* 20**05**, Vol. 7, p. 166-172.

169. S. J. Yao, J. H. Xu, Y. Wang, X. X. Chen, Y. X. Xu and S. S. Hu,. *Anal. Chim. Acta,.* **2006**, Vol. 557, p. 78-84.

170. A. Salimi, R. Hallaj, S. Soltanian and H. Mamkhezri. *Anal. Chim.* **2007**, Vol. 594, p. 24-31.

171. L.-C. Jiang and W.-D. Zhang. *Electroanalysis,.* **2009**, Vol. 21, p. 988-993.

172. R. Yuan, X. M. Miao, Y. Q. Chai, Y. T. Shi and Y. Y. Yuan,. *J. Electroanal. Chem.,.* **2008,** Vol. 612, p. 157-163.

173. G. L. Luque, M. C. Rodriguez and G. A. Rivas. *Talanta.* **2005**, Vol. 66, p. 467-471.

174. H. Elzanowska, E. Abu-Irhayem, B. Skrzynecka and V. I. Birss,. *Electroanalysis.* **2004**, Vol. 16, p. 478-490.

175. Zhou et al. *Anal. Chem.* **2009**, Vol. 81, p. 5603.

176. Y. Shao, J. Wung, H. Wu, J. Liu, I. A. Aksay,Y. Li. *Electroanalysis.* **2010**, Vol. 22, p. 1027-1036.

177. S. Q. Liu, X. A. Xu, S. J. Jiang and Z. Hu,. *ACS Nano,.* **2010**, Vol. 4, p. 4292-4298.

178. L. M. Dai, K. P. Gong, F. Du, Z. H. Xia and M. Durstock. *Science.* **2009**, Vol. 323, p. 760-764.

179. R. G. Compton, B. Sljukic and C. E. Banks,. *Nano. Lett.* **2006**, Vol. 6, p. 1556-1558.

180. X. H. Xia, J. Li, J. D. Qiu, J. J. Xu and H. Y. Chen. *Adv. Funct. Mater.,.* **2007**, Vol. 17, p. 1574-1580.

181. S. J. Yao, J. H. Xu, Y. Wang, X. X. Chen, Y. X. Xu and S. S. Hu,. *Anal. Chim. Acta.* **2006**, Vol. 557, p. 78–84.

182. Zhang, L.-C. Jiang and W.-D. *Eectroanalysis.* 20**09**, Vol. 21, p. 988-993.

183. C. Lee, X. Wei, J. W. Kasar, J. Hone,. *Science.* **2008,** Vol. 321, p. 385-388.

184. A.M. Rawlett, T.J. Hopson, I. Amlani, R. Zhang, J. Tresek, L. Nagahara, R. K. Tsui, H. Goronkin,. *Nanotech.* **2003**, Vol. 14, p. 377-384.

185. S. Zhu, G. Xu, *Nanoscale.* **2010**, Vol. 2, p. 2538-2549.

CHAPTER 2

Novel carbon nanostructured based hierarchical material as electrocatalysts for CO_2RR

2.1 Introduction

As mentioned in the introduction chapter, the electrochemical reduction of CO_2 is a challenging process to perform. It is a multi-electron reduction process, which can yield a wide range of different products. The reduction product is dependent on the number of the electrons involved. Table 2.1 reports the reduction reactions that CO_2 can undergo. The first electron transfer is characterized by a high energetic barrier associated to a change in geometry, from the linear CO_2 to the bent $CO_2^{\cdot -}$. (1)

Reaction	E^0_{redox} **(V vs NHE)**
$CO_2 + e^- \longrightarrow CO_2^{\cdot -}$	-1.9
$CO_2 + H^+ + 2e^- \longrightarrow HCO_2^-$	-0.49
$CO_2 + 2H^+ + 2e^- \longrightarrow CO + H_2O$	-0.53
$CO_2 + 4H^+ + 4e^- \longrightarrow HCHO + H_2O$	-0.48
$CO_2 + 6H^+ + 6e^- \longrightarrow CH_3OH + H_2O$	-0.38
$CO_2 + 8H^+ + 8e^- \longrightarrow CH_4 + 2H_2O$	-0.24

Table 2.1 Half-reaction of CO_2 reduction.

As it can be observed in table 2.1, protons also play a crucial role. Typically, the CO_2RR follows a proton coupled electron transfer (PCET) mechanism, which involves the concerted transfer of a proton and an electron. Thus, a proton source is necessary to produce the reaction with appreciable rate. However, the proton source may pose a further challenge in the CO_2RR, as from a thermodynamic point of view, the E^0 for the proton reduction (E^0 =-0.41 V vs NHE) is very close to the E^0 for the reduction of CO_2. Moreover, proton reduction is kinetically more favored than CO_2 reduction, thus the hydrogen evolution (HER) through proton reduction becomes a seriously competing process, affecting the selectivity of CO_2RR. (2) Up to now, the catalysts proposed by literature for CO_2 reduction present several drawbacks such as low selectivity (towards CO_2RR or towards a certain CO_2 product), low stability (decomposition and/or poisoning), high overpotentials and low currents. Moreover, the reduction of CO_2, especially performed in aqueous medium, is affected by the low solubility of CO_2.

In nature, the enzymes Carbon Monoxide Dehydrogenases (CODHs) and Formate Dehydrogenases (FDHs) are known to reduce CO_2 to carbon monoxide (CO) and formate (HCO_2^-), respectively. These enzymes are composed by an active site, in which the reduction of CO_2 takes place, surrounded by a protective shell encharging of protect the active site and direct the substrate to it. With this strategy, the enzymes can trig the conversion of CO_2 operating close to thermodynamic potential (E (CO_2/CO) = -0.11 V; E (CO_2/HCO_2^-)=-0.02 V vs RHE at pH 7 and with a reversible electrochemical behavior. Armstrong et al. investigated the opportunity to support CODHs onto an electrode surface, with important results. However, the implementation of enzyme-based electrocatalyst becomes very complex due to the hard purification procedures needed for its preparations and it slow stability for long time experiments. (3) Nevertheless, nature is still inspiring the assembly of artificial catalytic systems that can mimic enzymes for orchestrating the CO_2 reduction with improved performances. In particular, the application of hierarchical nanostructured materials has drawn special attention due to a successful interplay of the different components with consequent increase of activity and selectivity of the CO_2 reduction process. Won et al., reported a hierarchical tin dendrite electrode consisting of a multi-branched conifer-like structure with an enlarged surface area able to convert CO_2 to formate over 18 hours of experiments without any considerable catalytic degradation. They demonstrated that CO_2 conversion selectivity on Sn electrodes was correlated with the native oxygen content at the subsurface, and the high oxygen content in the dendritic component of the hierarchical material was effective in $CO_2^{\cdot -}$ stabilization, a key intermediate for the formate production. (4) A hierarchical catalyst based on Cu_xO nanosphere particles has been reported for CO_2 reduction by Qiao et al.. The authors found that the formation of Cu metallic sites during the electrolysis experiment were correlated to an increase in formate evolution. The hierarchical structure also secured a high stability over long time experiments. (5) As a last example, Sen et al., reported a hierarchical catalyst consisting of porous copper nanofoams, where the large surface provided by this electrocatalyst was instrumental to drive selectivity towards hydrocarbon (propylene and ethane) evolution from CO_2 reduction. (6) Recently, hierarchical materials using a porous layer of metal oxides, such as TiO_2, SiO_2, CeO_2, or biodegradable polymers have been designed with the objective of mimicking the protein shell present in enzymes. In particular, the oxide layer improves stabilization of the nanoparticulate transition metal active sites, avoiding their sintering, leaching or decomposition pathways. In addition to metal oxide phases, another intriguing possibility is to use ionic liquids (ILs) or amine containing adsorbents polymers as stabilizing agents, which can chemically interact with CO_2. Among the different ILs, imidazolium salts aroused great interest because of their high affinity for CO_2. (7) Several research groups studied extensively the ability of ILs to capture CO_2 and analyzed how the nature of the constituent anion and cation affect the CO_2's adsorption rate. These studies have led to the formation of a wide library of compounds, called task specific ionic liquids (TSILs). TSILs consist on functionalized ILs' cations with special moieties (especially amines) providing much more interaction points for CO_2 than common ILs which interact mainly by mean of Lewis acid-base interactions. (8) Therefore, TSILs can exploit physical and chemical interaction, improving the CO_2 capture ability. In the last decades, ionic liquid supported on scaffold such as porous alumina, zeolite and carbon nanostructures have found fertile soil, as the presence of a support puts a remedy to some of the ILs' drawbacks such as low stability and high viscosity, while the contact area between CO_2 and ionic liquid results improved (9) (10) (11) (12)

This chapter focuses on the characterization of CO_2 activation operated by two hierarchical nanostructured materials working in aqueous medium: Pd@TiO_2/ox-SWCNHs and NiCyclam@BMIM/p-SWCNHs.

Pd@TiO_2/ox-SWCNHs comprises Pd@TiO_2 core-shells nanoparticles linked to ox-SWCNHs. This system has shown good selectivity towards the conversion of CO_2 to $HCOO^-$ at potentials as low as -0.05 vs RHE.

NiCyclam@BMIM/p-SWCNHs was obtained exploiting the dispersive forces acting between the ionic liquid and the carbon nanostructure, creating a supported ionic liquid phase (SILP). The well-known molecular catalyst NiCyclam has been successfully entrapped within the ionic liquid layer, providing an interesting example of heterogenized electrocatalyst for the reduction of CO_2 in aqueous medium. NiCyclam retains its catalytic activity towards the conversion of CO_2 to CO.

2.2 Bio-inspired SWCNH/TiO_2/Pd nanojunctions enabling electrocatalytic reduction of CO_2 to Formate in water at neutral pH

CO_2 reduction is driven by enzymes with the aid of specific structure/reactivity features. In enzymes, hetero bi-metallic arrangements of the active sites activate CO_2 via a cooperative interaction between proximal “soft” and “hard” metal centers. A proton donor/acceptor source promotes the PCET mechanism, lowering the overall required energy. Pd@TiO_2/ox-SWCNHs was designed taking into account these concepts: in Pd@TiO_2 core-shells, “hard” TiO_2 worked in synergy with the “soft” Pd promoting proton/hydride translocation and protecting from the agglomeration.

Pd@TiO_2 core-shells were conjugated with ox-SWCNHs, with the latter playing the role of conductive nano-platform facilitating the electron transport. Thus, the overall electrocatalytic process was shown to benefit from the increased charge carrier mobility implemented at the CNS/metal junctions. ox-SWCNHs did not work only as a conductive platform, but they also contributed to CO_2 adsorption. (13)

The hierarchical material therefore consisted of three components each performing specific functions. The hydrophilic TiO_2 shell promoted the proton and electron transfer steps involving the metal oxide hydration sphere, and in addition it shielded the active Pd sites from irreversible agglomeration and leaching phenomena promoting catalyst longevity. The confinement of ultra small Pd NPs (≈2 nm) enabled a fast transition to an active Pd-hydride phase under reducing conditions. The SWCNHs secured good electron conductivity facilitating electron transfer onto the active sites.

2.2.1 Results and discussion

2.2.1.1 Synthesis

In the scheme below, the synthesis of Pd@TiO_2/ox-SWCNHs is shown. In the first step, an oxidation treatment of the SWCNHs was performed, to introduce carboxylic groups onto the carbon nanostructure surface, which aided the anchoring of the Pd@TiO_2 core-shells precursor. The covalent modification also serves to improve dispersibiliy of the SWCNHs in liquid media. The solution of Pd@TiO_2 precursor was prepared dissolving the right amount of Pd nanoparticles protected with mercaptoundecanoic acid (Pd-MUA) in the required amount of Titanium Butoxide ($Ti(OBu)_4$) in order to obtain the desired ratio of Pd/TiO_2. The solution of Pd@TiO_2 precursor was added dropwise to a suspension of ox-SWCNHs in ethanol (EtOH) under continuous sonication and was kept under sonication for another 30 minutes. Finally, the material was subjected to slow hydrolysis with a mixture of H_2O/THF added dropwise to yield the final Pd@TiO_2/ox-SWCNHs. After additional 30 min of sonication, the mixture was filtered through 0.45 µm Millipore filters, washed with EtOH/H_2O 2:1 v/v and finally with neat EtOH. The final material was dried at 80 °C overnight prior to being used (Pd@TiO_2/ox-SWCNHs). A similar approach was adopted in the absence of Pd-MUA in order to obtain the corresponding Pd-free catalyst (TiO_2/ox-SWCNHs). A further reference material with only Pd NPs supported onto ox-SWCNHs was also synthetized. ox-SWCNHs were sonicated in presence of the right amount of Pd NPs precursor, reduced by adding $NaBH_4$ solution, affording isolation of Pd/ox-SWCNHs.

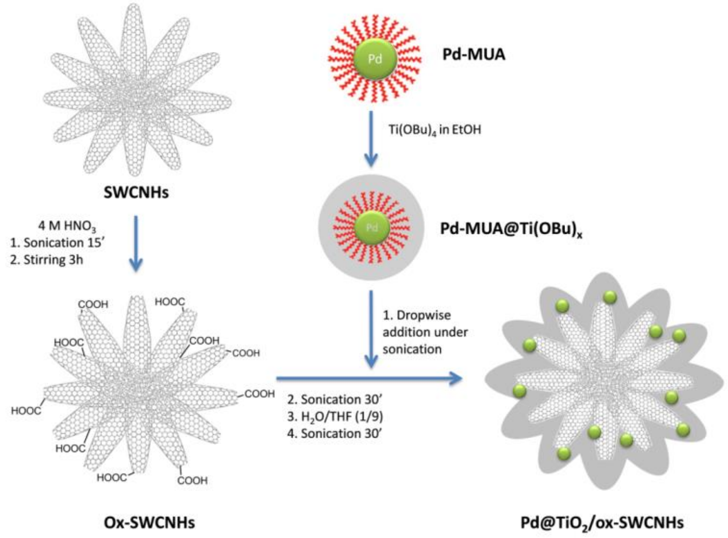

Scheme 2.1: Reaction scheme of Pd@TiO_2/ox-SWCNHs.

2.2.1.2 Macroscopic and microscopic characterization

Pd@TiO_2/ox-SWCNHs was fully characterized using several techniques. Thermogravimetric analysis (TGA) was used to evaluate the carbon/metal weight composition. The carbon accounts for about 75 wt % and the metal oxide for the remaining 25%. Moreover, TGA allowed to distinguish that the carbon phase in turns consisted of about 11% of organic functional groups which have lower combustion temperature (225°C) than the poli-aromatic structure (510°C). The organics comprised the oxygenated groups on the SWCNHs and the organic ligands of the metal precursor not hydrolyzed (figure 2.1).

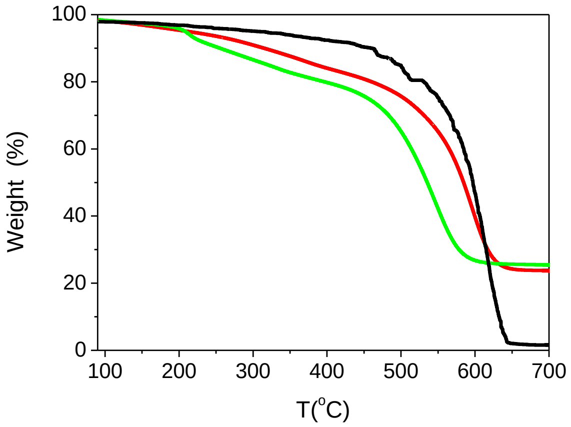

Figure 2.1. TGA plots of the ox-SWCNHs (–),TiO_2@ox-SWCNHs (–) and the Pd@TiO_2/ox-SWCNHs (–).

The successful occurrence of the reaction was also confirmed by Raman and FT-IR spectroscopy.

Raman spectra are reported in figure 2.2 A. The spectra collected for ox-SWCNHs exhibited the typical features of the carbon nanostructures (CNSs): the disorder–induced D band at ≈ 1330 cm^{-1}, its second-order harmonic (2D band) at ≈ 2665 cm^{-1} and the G band at ≈ 1580 cm^{-1} relative to the in-plane vibrational mode of the sp^2 graphitic framework. (14) The I_D/I_G ratio, 1.27, was not significantly affected after the oxidation treatment compared to the pristine material, as a result of the mild oxidation treatment used. This implies a limited disruption of the π-extended framework following covalent modification, thus preserving the electronic properties of the SWCNHs. (15) (16) In the spectra collected on TiO_2/ox-SWCNHs and Pd@TiO_2/ox-SWCNHs, no signals corresponding to TiO_2 was observed, confirming that the metal oxide layer was in an amorphous phase as expected given that no thermal treatment was carried out on the material. However, application of a higher laser power irradiation induced the local crystallization of amorphous TiO_2, leading to the appearance of the characteristic peaks of TiO_2 anatase phase at 146 cm^{-1}, 198 cm^{-1}, 395 cm^{-1}, 513 cm^{-1} and 639 cm^{-1}. (17) (18)

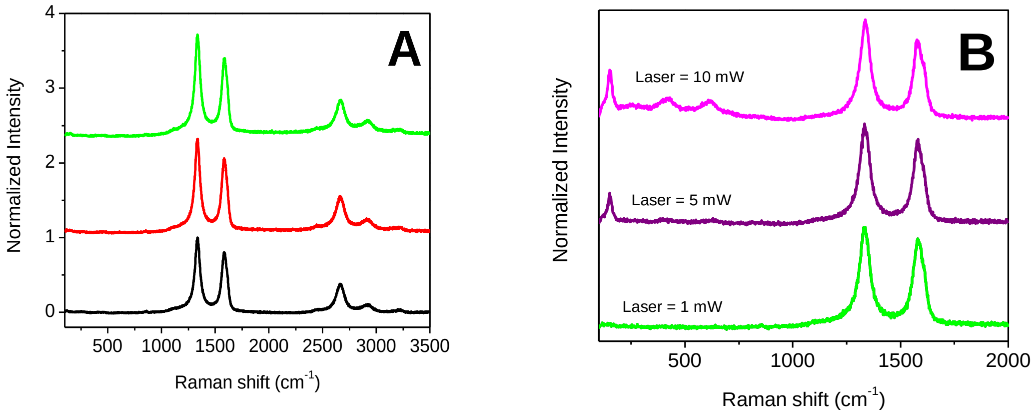

Figure 2.2. A) Raman spectra of the **(–)** ox-SWCNHs, (–) TiO_2/ox-SWCNHs and the Pd@TiO_2/ox-SWCNHs (–). B) Raman spectrum of Pd@TiO_2/ox-SWCNHs at different laser powers, 1mW, 5 mW and 10 mW.

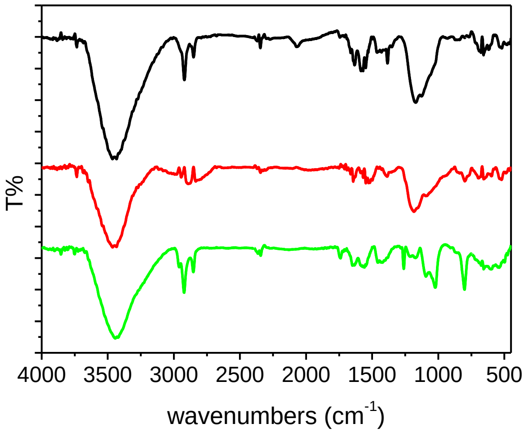

Figure 2.3. FT-IR spectra of the **(–)** ox-SWCNHs, (–) TiO_2/ox-SWCNHs and the Pd@TiO_2/ox-SWCNHs (–).

The FTIR spectra of TiO_2/ox-SWCNHs displayed, together with the peaks relative to the ox-SWCNHs scaffold, a weak sharp peak at 800 cm^{-1} which is indicative of the vibrational mode of O-Ti-O bonds, confirming the presence of the TiO_2 shell around the carbon nanostructure. The broad band at 3400 cm^{-1} was related to the Ti-O-H moieties stemming from the TiO_2 shell. The spectra of the final material Pd@TiO_2/ox-SWCNHs exhibited all the peaks observed for the precursors materials, namely peaks at ca. 800, 1100, 1400 and 1600 cm^{-1} corresponding to the vibrational modes of O-Ti-O, C–O, C=C and C=O moieties of the carbon phase, respectively. The broad band at 3400 cm^{-1}, is associated to O-H groups, coming from C-O-H, (CO)O-H and Ti-O-H functionalities. (18) (19)

The morphology and composition of Pd@TiO_2/ox-SWCNHs,ox-SWCNHs and TiO_2/ox-SWCNHs were investigated by High Resolution Transmission Electron Microscopy (HRTEM), in combination with STEM and Energy-Dispersive X-ray spectroscopy (EDX). The adhesion of the ox-SWCNHs with a thin TiO_2 shell can be noted in the TEM and STEM images, with the ultra-small Pd nanoparticles, of average size 1.5 nm, embedded in TiO_2 shell clearly visible (figure 2.4 and 2.5).

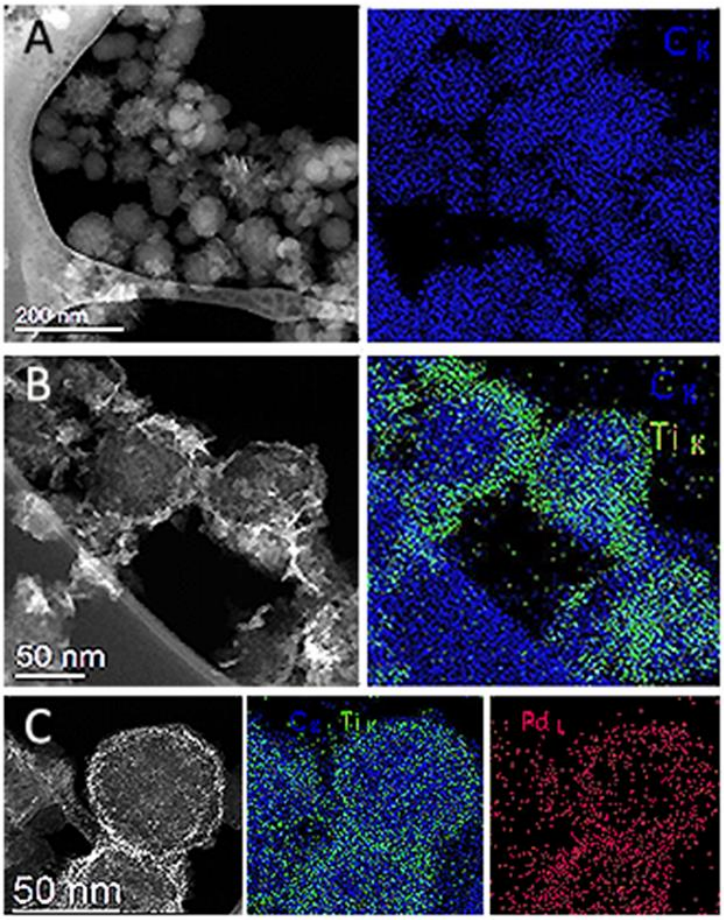

Figure 2.4. Representative HAADF (black and white) and corresponding EDX maps (colours) of the SWCNH-based hetero-structures: A) ox-SWCNHs, B) TiO_2/ox-SWCNHs, C) Pd@TiO_2/ox-SWCNHs.

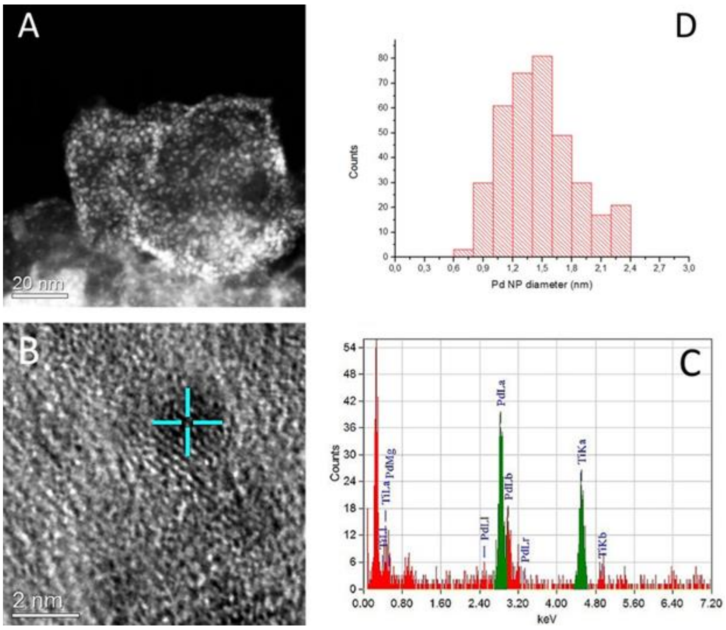

Figure 2.5. Representative HR-TEM of catalysts Pd@TiO_2/ox-SWCNHs (A) showing the size of the Pd nanoparticles (B), EDX spectrum (C) and the Pd size distribution (D).

As expected, Fast Fourier Transform (FFT) and selected area electron diffraction (SAED) analysis did not reveal any crystalline area for TiO_2, in agreement with the Raman data.

2.2.1.3 Electrochemical characterization

The electrode modified with Pd@TiO_2/ox-SWCNHs was prepared by drop casting of 20uL of 3 mg mL^{-1} Pd@TiO/ox-SWCNHs aqueous suspension. Cyclic voltammetry (CV) techniques have been used to explore the redox behavior of Pd@TiO_2/ox-SWCNHs. The CVs of the nano-hybrid Pd@TiO_2/ox-SWCNHs, ox-SWCNHs and TiO_2/ox-SWCNHs, are comparatively reported in figure 2.6. CVs have been collected in N_2-saturated 0.50 M $NaClO_4$ solution. The investigated potential window ranges from 1.5 V to -1.0 V using a scan rate of 0.03 V s^{-1}.

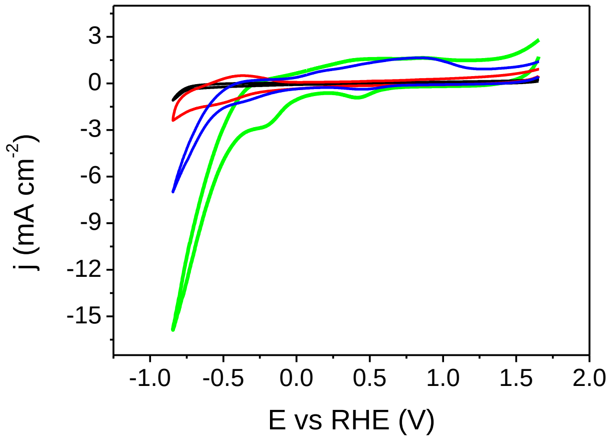

Figure 2.6. CVs obtained on GCE modified with ox-SWCNHs (–), TiO_2/ox-SWCNHs (–),Pd/ox-SWCNHs (–) and Pd@TiO_2/ox-SWCNHs (–) in 0.50 M $NaClO_4$ solution under N_2. Scan rate: 0.03 V s^{-1}.

The CV profile of ox-SWCNHs evidences no faradaic processes (or redox reaction) in the studied potential window. In contrast, the TiO_2/ox-SWCNHs CV presents a redox process with peak potentials at -0.65 V and -0.35 V for the cathodic and anodic signals, respectively. This signal could be attributed to the Ti^{4+}/Ti^{3+} interconversion, in good agreement with previously reported results. (20) (21) The CV collected on Pd/ox-SWCNHs shows a broad anodic peak at 0.65V due to the adsorption of H_2 evolved during the cathodic sweep, and a cathodic peak at -0.4 V due to the reduction of PdO species formed during the anodic sweep. The CV collected on Pd@TiO_2/ox-SWCNHs exhibits the above described behavior corresponding to Ti^{4+}/Ti^{3+} and also two more signals: a cathodic peak at -0.4 V due to the reduction of PdO species formed during the oxidation sweep, and an anodic peak at ca 0.65 V due to the desorption of H_2 evolved during the reduction sweep at negative potentials higher than -0.4 V. (22) (23) (24)

The Pd electroactive surface area (EASA) was then calculated as follows: 1) the peak associated to the reduction of PdO was first integrated, in order to obtain the charge involved; 2) knowing that the charge needed for the reduction of a PdO monolayer is 405 µC cm^{-2}, and using the equation below, the Pd EASA was finally assessed.

$$Pd\ EASA = \frac{Q}{405\ x\ 10^{-6}}$$

Q is the charge obtained by the integration of the reduction of PdO and the calculated Pd EASA was (0.22 ± 0.04) cm^2. This value suggested that Pd NPs were accessible to the redox reaction occurring at the nano-hybrid modified electrode. Importantly, the Pd EASA calculated for Pd/ox-SWCNHs was lower (0.15± 0.02) cm^2. This difference can be ascribed to aggregation of Pd NPs during the CV experiment, which yield to a reduction of the electroactive area of Pd, highlighting the benefit of protecting the Pd NPs with the titania shell.

2.2.1.4 Electrocatalytic reduction of CO_2 using Pd@TiO_2/ox-SWCNHs modified electrode

Preliminary studies on CO_2 activation have been carried out in three different electrolytes: 1) 0.10 M phosphate buffer pH 7.4; 2) in 0.50 M $NaClO_4$ solution, and 3) in 0.50 M $NaHCO_3$ under N_2 and CO_2 saturated solutions. The concentration of PBS is lower because of a specific technical necessity: the column used in the Ionic Liquid Chromatogh (ILC), for the detection of formate in solution, could not tolerate higher concentration of phosphate anions.

These three electrolytes have allowed to study CO_2 reduction simultaneously at three different pH and in three different media because saturation with CO_2 produces pH decrease. Both pH and electrolyte can profoundly influence the mechanism of the process. Since both the anion and the cation of the electrolytes can intervene in the process stabilizing key reaction intermediates, (25) (26) the same cation (Na^+) was selected for all the electrolytes.

CO_2 activation has been first studied by CV in the window potential ranging from 1V to -1V, using a scan rate of 0.05 V s^{-1} (Figure 2.7). The pH before and after CO_2 saturation for each medium are reported in see table 2.2.

	pH in N_2 saturated	pH in CO_2 saturated
0.50 M $NaClO_4$	7	4.7
0.10 M PBS	7.4	6.4
0.50 M $NaHCO_3$	8.4	7.4

Table 2.2: pH values measured before and after the CO_2 saturation of the electrolytes. Before pH measures CO_2 have been bubbled in each medium for 1hr.

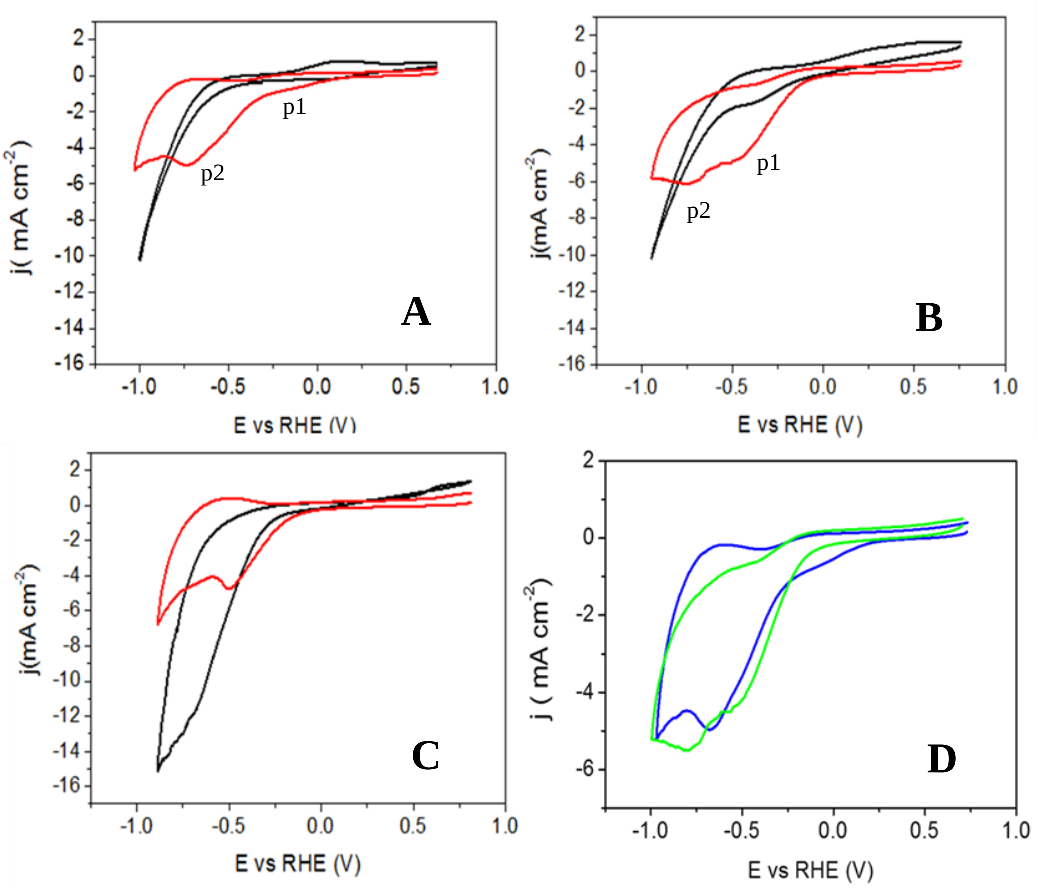

Figure 2.7. CVs of Pd@TiO_2/ox-SWCNHs in (A), 0.50 M $NaClO_4$, (B) 0.10 M PBS, C) 0.50 M $NaHCO_3$ in N_2 (–) and CO_2 (–) saturated 0.5 M $NaHCO_3$. Scan rate: 0.05 V s^{-1}. D) Comparison of the CVs collected in CO_2 saturated 0.50 M $NaClO_4$ (–) and 0.10 M PBS (–). Scan rate: 0.05 V s^{-1}.

Based on the currents observed for the three electrolytes in N_2- and CO_2-saturated solutions respectively, it can be observed that $NaHCO_3$ does not seem to be the most appropriate electrolyte (or the resulting pH conditions are not appropriate). The currents in N_2-saturated conditions are higher than those in CO_2-saturated media throughout the explored potential range, CO_2 in solution moves the equilibrium towards H^+ and HCO_3^- evolution. Probably, this HCO_3^- interacts with the electrode surface reducing the electrodes conductivity disfavoring the discharge of the electrolyte, important in N_2-saturated condition and the CO_2 reduction reaction. This makes redundant any attempt to assess the activity of the catalysts in $NaHCO_3$. On the contrary, for PBS and $NaClO_4$, there is a distinct range of potential (approximately between -0.01 and -0.8 V for $NaClO_4$ and between -0.06 and -0.8 V for PBS) where currents associated to CO_2 are significantly higher than the background currents in N_2, allowing further analysis of the CO_2 activation process. In more details, the CVs relative to $NaClO_4$ and PBS recorded in CO_2 saturated solutions show two broad cathodic signals (labeled p1 and p2 in Fig 2.7). Analyzing the two signals it is found that for experiments performed in 0.10 M PBS the distance between p1 and p2 was 0.20 V, while in 0.50 M $NaClO_4$ the first wave was very broad and was almost 0.60 V distant from the second wave. The potentials of the two peaks and current have been reported for the two electrolytes in table 2.3. These findings suggest two different processes, possibly associated with CO_2 reduction, occur in a narrower potential window in 0.10 M PBS than in 0.5M $NaClO_4$. Figure 2.7 D reports the comparison of the CVs in 0.50 M in $NaClO_4$ and 0.10 M PBS.

Electrolyte	Ep_2 [V]	Ep_1 [V]	jp_2 [mA cm^{-2}]	jp_1 [mA cm^{-2}]	$\lvert Ep_2-Ep_1 \rvert$ [V]
0.10 M PBS	-0.74	-0.50	-6.04	-4.86	0.2
0.50 M $NaClO_4$	-0.67	-0.06	-4.94	-0.7	0.6

Table 2.3. E_p: Peak potential. The values are referred to the RHE reference electrode. The current is reported as density current (j_p) normalized by the electroactive surface area.

On the basis of the above results, 0.10 M PBS and 0.50 M $NaClO_4$ were selected as promising media for CO_2 activation and next investigation were carried out in these two electrolytes. The CVs of Pd@TiO_2/ox-SWCNHs were also compared versus those of the reference materials TiO_2/ox-SWCNHs and ox-SWCNHs (figure 2.8), showing that ox-SWCNHs did not produce any CO_2 activation, while the activation is only negligible with TiO_2/ox-SWCNHs.

In more details, the CVs in both PBS and $NaClO_4$ in CO_2 saturated solution of TiO_2/ox-SWCNHs showed a redox process associated with the switch between Ti^{3+}/Ti^{4+}. This redox process can relate to the coordination of CO_2 to TiO_2. The expected mechanism on a TiO_2 phase involves the one-electron reduction of CO_2 to form the radical $CO_2^{\bullet-}$, with TiO_2 facilitating electron transfer through hybridized orbitals in the monodentate and bidentate configuration of CO_2 and contributing to the stabilization of $CO_2^{\bullet-}$. (20) (21) (22) (22) (24) However, in the specific case, activation of CO_2 by Pd-free TiO_2 active phase does not proceed significantly.

The catalytic properties have been investigated either in PBS and $NaClO_4$.

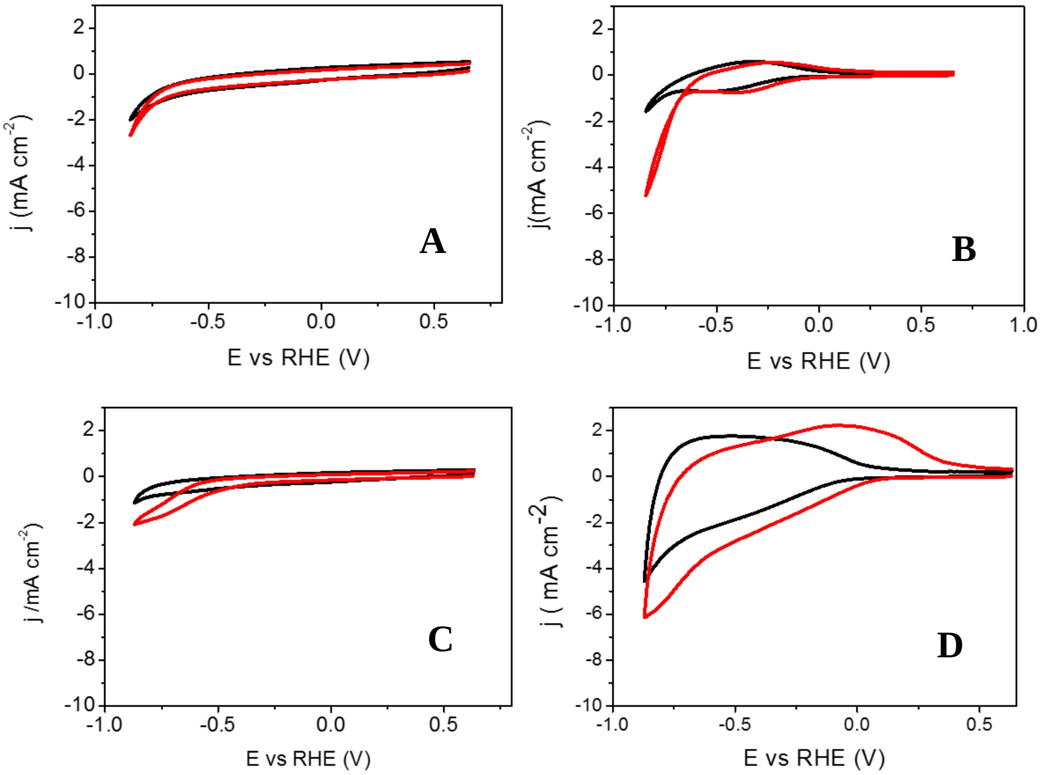

Figure 2.8. CV of A) ox-SWCNHs and B) TiO_2/ox-SWCNHs in 0.10 M in PBS and C) ox-SWCNHs and D) TiO_2/ox-SWCNHs in 0.50 M $NaClO_4$ in N_2 saturated (–) and CO_2 saturated solution (–).

2.2.1.4.1 Electrocatalytic activation of CO_2 in 0.10 M PBS

The selectivity of the electrocatalytic reduction by Pd@TiO_2/ox-SWCNHs has been first addressed by bulk-electrolysis experiments carried out at constant-potential, in CO_2-saturated phosphate buffer solution at room temperature (0.10 M PBS, pH 7.4). To this aim, a standard three-electrode cell has been assembled, integrating a Ag/AgCl (3 M KCl) reference electrode and a Pt counter electrode, with a Pd@TiO_2/ox-SWCNHs modified Toray carbon paper working electrode. The fixed potential was set at -0.15 V vs RHE, which is a value close to the onset potentials and chosen after careful optimization of the Faradaic efficiency for the CO_2 reduction product. Product analysis for the bulk electrolysis performed at -0.15 V was performed both by Ionic Liquid Chromatography (ILC) and by continuous GC sampling of the cell head-space at 20 min intervals. The schematic representation of the cell is reported below (figure 2.9). From GC analysis, only H_2 has been detected as gaseous product, suggesting the concomitant reduction of H^+ during the reduction of CO_2 in PBS. The liquid phase was analyzed by means of ILC, revealing the presence of $HCOO^-$ as sole product of CO_2 reduction. After 1 hour of electrolysis, the faradaic efficiency (FE) was 10%. In figure 2.10 the comparison between H_2 and $HCOO^-$ FE is reported.

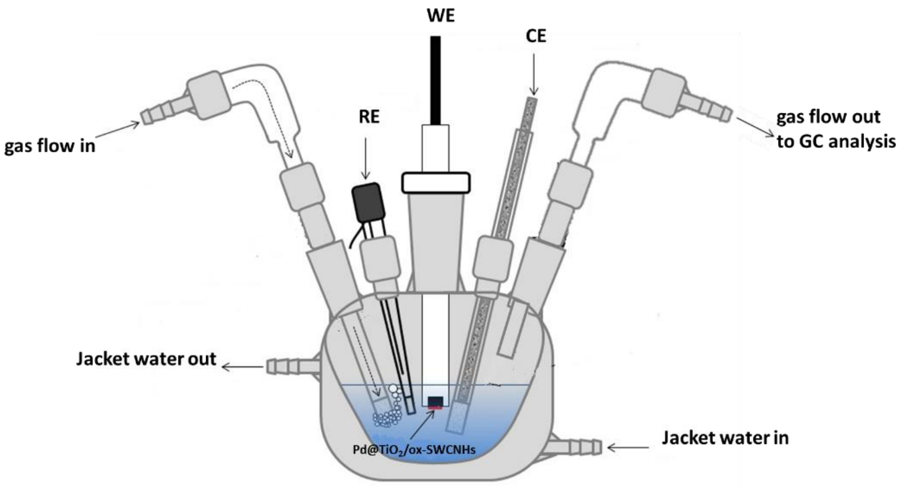

Figure 2.9. Schematic representation of the gas-tight electrochemical cell.

H_2 was observed only when the electrolyte was CO_2 saturated (not in N_2 saturated conditions), and initially this behavior was attributed to a drop of pH following saturation with CO_2. It is known that proton reduction is kinetically favoured at lower pH, where the proton is more available. However, a control experiment in absence of CO_2 but under pH conditions correspondent to the same pH value achieved after CO_2 saturation, resulted in zero H_2 production. Hence, it can be hypothesized that H_2 evolved through an intermediate involving CO_2 reduction, and not simply from water. Moreover, H_2 amount increased while moving towards more negative potentials, evidencing that CO_2 reduction was less favored at more cathodic potentials.

The trend of FE in $HCOO^-$ has been studied by bulk electrolysis over 3 hours long experiments. The FE reached the maximum values after very short electrolysis time, then dropping to very low values at the end of the 3hs, with a concomitant increase in H_2 FE (Figure 2.10).

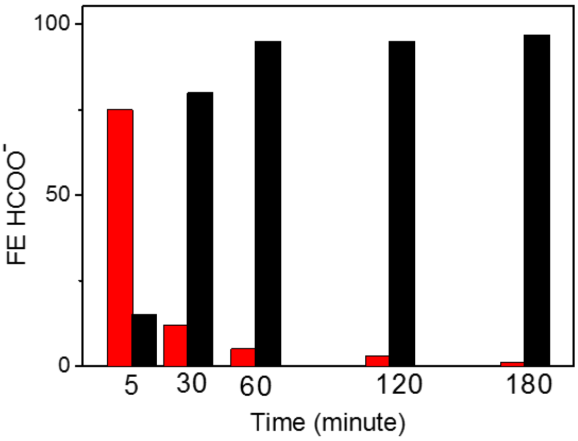

Figure 2.10. FE of $HCOO^-$ (red bar) and FE of H_2 (black bar) in function of the time in 0.10 M PBS.

FE decrease could be associated to three main aspects:1) the adsorption of $HCOO^-$ (or other CO_2 minor products) at the electrocatalyst sites which can hamper the CO_2 adsorption and activation , 2) there could be a specific interaction between TiO_2 surface and PBS anions. In fact, it has been demonstrated that phosphate anions such as $H_2PO_4^-$

$/HPO_4^{2-}$ can be strongly adsorbed onto the TiO_2 layer, with the OH groups of TiO_2 replaced by $H_2PO_4^-$ through a ligand exchange reaction, decreasing the active sites on TiO_2 surface, with concomitant decrease of the catalytic properties (27); 3) it may be that the as formed formate undergoes further catalyzed decomposition to release H_2, being this the reverse of the reduction reaction, once reached a certain concentration value, up to reaching a stationary state of formation/decomposition.

The current-time profile was evaluated over longer time electrolysis to highlight the Pd@TiO_2/ox-SWCNHs catalytic properties. In contrast with the FE decrease of $HCOO^-$, the total geometric current density (j_{tot}) reached a value of ≈ -2.00 mA cm^{-2} and maintained a very stable profile, with a negligible decrease (< 5%) over 24h of electrolysis (figure 2.11 A). On the contrary, the reference material TiO_2-free Pd/ox-SWCNH electrocatalyst underwent a fast deactivation at -0.15 V, with current density decreasing of about 50 % already after 3 hours (figure 2.11 B). Analogous results were reported for the similar Pd/amorphous carbon system. The deactivation process was ascribed to the sintering of the Pd nanoparticles, along with the formation of small amounts of CO, which poisoned the catalyst (28).

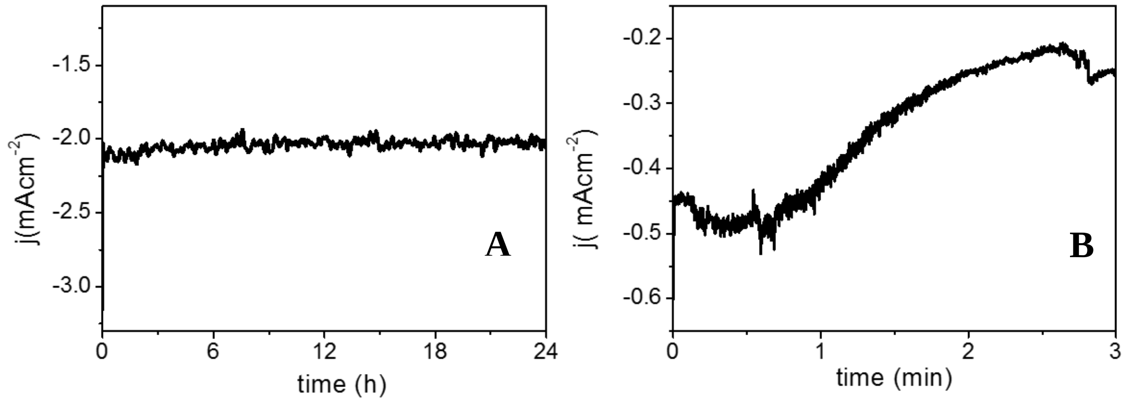

Figure 2.11 A) Pd@TiO_2/ox-SWCNHs over 24hours long bulk electrolysis experiment at -0.15V. B) Pd/ox-SWCNHs over 3hours long bulk electrolysis at -0.15 V.

Indeed, TEM analysis of the recovered Pd/ox-SWCNHs catalyst (figure 2.12) showed a significant NP aggregation after 3 hours of electrolysis, with some particles also detached from the SWCNHs support as confirmed by TEM analysis. In the case of Pd@TiO_2/ox-SWCNHs, the TiO_2 phase effectively protects the Pd NPs towards agglomeration and leaching.

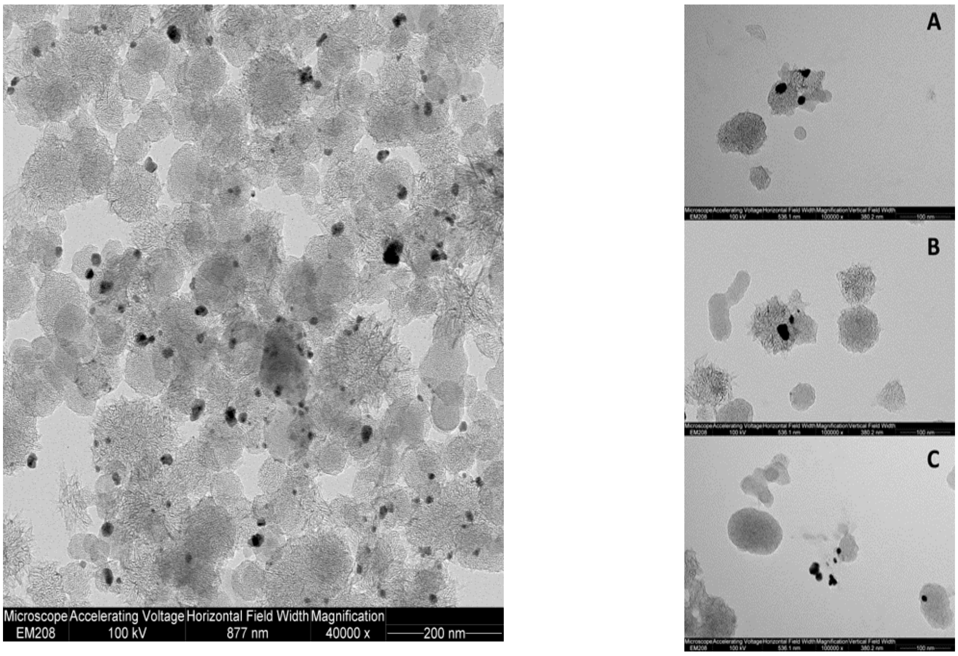

Figure 2.12 (on the left) TEM images of Pd/ox-SWCNHs before bulk electrolysis experiment at -0.15V for 3 hours, (on the right) TEM images of Pd/ox-SWCNHs after bulk electrolysis experiment at -0.15V for 3 hours.

Hence, from a current stability point of view, the embedding of the active Pd NPs within a metal oxide shell seems to be in principle a winning strategy. The drop of FE must be however further investigated. Finally, Tafel analysis, providing the dependence of the electrocatalytic rate (log *J)* on the applied potential, has been evaluated to address the possible mechanism of formation of formate. The resulting Tafel plot (figure 2.13) is characterized by two different regimes, with a calculated slope of (149 ± 6) mV·dec^{-1} at low overpotentials (E<-0.2 V), followed by a significant leveling off to a slope of (400 ± 16) mV·dec^{-1}. These values are in perfect agreement with the electrocatalytic response expected for Pd NPs as the competent hydrogenation sites. (28) In particular the Tafel slope of (149 ± 6) mV·dec^{-1}, which is consistent with a Pd-mediated hydride transfer mechanism, turns out to be the dominating regime also at higher *J* values, up to -0.2 V, with no mass transfer limitations (28).

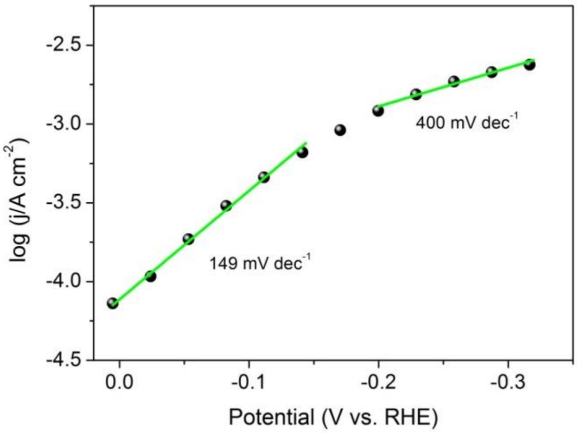

Figure 2.13. Tafel (Potential vs log j) plot in CO_2-saturated 0.10 M PBS pH 7.4.

These results are in analogy with the recent work by Kanan et al., who proposed a mechanism involving the electrochemical generation of Pd-H active sites responsible for the direct CO_2 hydrogenation to formate (Scheme 2) (28).

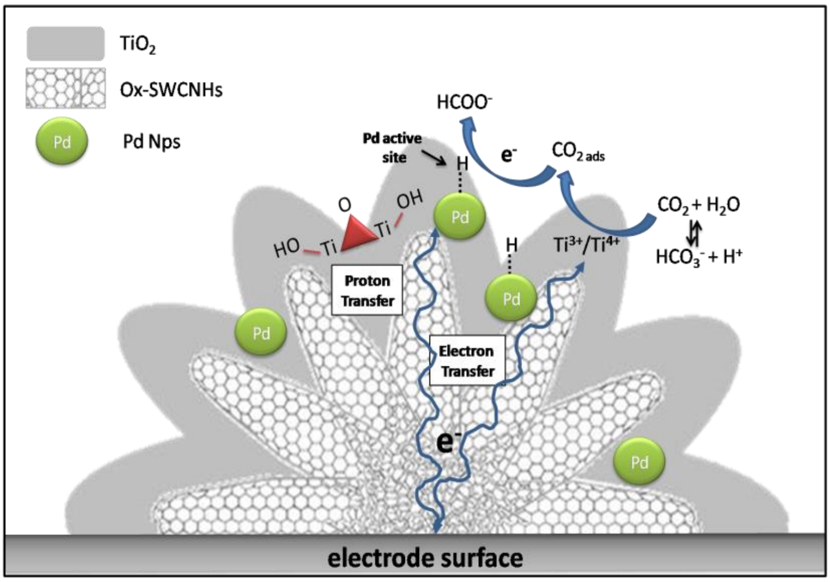

Scheme 2.2. Electrocatalytic reduction of CO_2 to formate by core-shell Pd@TiO_2/ox-SWCNHs heterostructures occurring at the hybrid organic-inorganic interface along bio-inspired guidelines, in water at neutral pH.

2.2.1.4.2 Electrocatalytic activation of CO_2 in 0.50 M $NaClO_4$

The electrocatalytic behavior of Pd@TiO_2/ox-SWNCHs has been then screened in 0.50 $NaClO_4$. Electrode preparation and electrochemical cell set-up were the same as for the PBS case. The fixed potentials for the bulk electrolysis experiments was chosen by analysis of the CV curves and was set at -0.05 V vs RHE, correspondent to the value of the middle point between the onset potential and the p1 potential. As for PBS, such value has been selected as the most appropriate in view of the obtained faradaic efficiency of the CO_2 reduction products. It must be noted that this potential is even lower than the one applied in PBS, -0.15V, implying a minimum of energy that must be supplied (in from of an overpotnatial) to trigger the reduction

Once again, from GC analysis of the cell HS, only H_2 has been detected as gaseous product, suggesting the concomitant reduction of H^+ during the reduction of CO_2, with no other gaseous CO_2 reduction products being formed. The liquid phase analyzed by means of ILC revealed again the presence of $HCOO^-$, which was the sole product of CO_2 reduction. After 1 hour of electrolysis, the faradaic efficiency (FE) was of 40% in $NaClO_4$ at -0.05V (figure 2.14 A), higher than that obtained in PBS, thus hinting that the perchlorate could be a better choice as electrolyte. Moreover, it is important to note that the working potential applied for the experiments carried out $NaClO_4$ is near the thermodynamic reduction potential at which the enzyme CODH converts CO_2 to $HCOO^-$. As for the PBS experiments, the observed H_2 was again related to a CO_2 reduction intermediate formed during electrolysis, as the analysis carried out in N_2-saturated conditions (but acidified with $HClO_4$ as to reach the same pH obtained by bubbling CO_2) yielded no H_2.

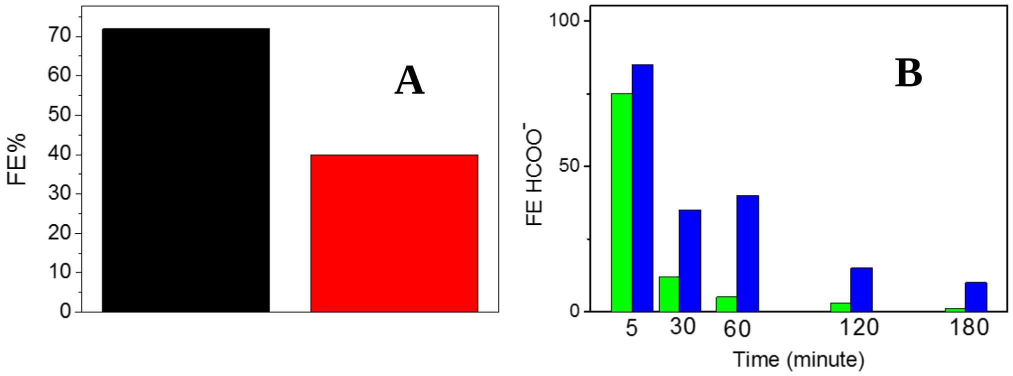

Figure 2.14. A) Bars plot reporting the comparison between FE% in H_2 (black bar) and $HCOO^-$ (red bar) in 0.10 M PBS and in 0.50 M $NaClO_4$ after 1 h of electrolysis **B)** FE of $HCOO^-$ in function of the time in 0.10 MPBS (green bar) and 0.50 M $NaClO_4$ (blue bar).

The trend of FE in $HCOO^-$ studied by bulk electrolysis over 3 hours long experiments was similar to what observed in PBS: the FE reached maximum values after very short electrolysis time, then dropping to very low values at the end of the 3hs. However, the decrease in PBS was faster than in $NaClO_4$. The comparison of FE between PBS and $NaClO_4$ is reported in Figure 2.14 B.

The faster decrease of FE in PBS compared with $NaClO_4$ may be due to the specific interaction between the catalyst surface and the electrolyte. Both cation and the anion of the electrolyte can play a crucial role in CO_2 reduction mechanism, stabilizing reaction intermediates. (26) (25) (29) (30) Since the cation is the same for both, Na^+, the different behavior is likely to be related to the anionic moiety. The most important role played by the anions is to tune the local pH close to the electrode surface, limiting the availability of the protons and increasing the number of the active sites for the CO_2 reduction. (29) In particular, specific interaction between anion and electrode surface may hinder the adsorption of CO_2 to the electrocatalyst active sites. (26) Although a similar behavior has been observed for ClO_4^-, the interaction between ClO_4^- and TiO_2 is weaker, thus justifying the slower FE drop. (31).

However, the current-time profile of the fixed potential electrolysis experiment studied over periods as long as 24 hours showed a decrease of 50%, which could be associated to deactivation pathways of the electrocatalyst (figure 2.15 A). The possible irreversible deactivation of the catalyst (i.e. irreversible structural or chemical change of the catalyst) was checked by performing recycling experiments. In more details, three consecutive bulk electrolysis (1 hour long) at -0.05V vs RHE on the same electrode were carried out, using fresh electrolyte for each experiment. . Interestingly, the catalytic properties of the material were completely restored after each test (figure 2.15B). This is noteworthy, as it pointed to a temporary deactivation, favoring the hypothesis of a reversible adsorption of some intermediate onto the catalyst, which also compromised selectivity over time and current stability. For example, Min et al. reported a Pd/C electrocatalyst, that was selective for the conversion of CO_2 to formate, exhibiting current and FE decrease during the electrolysis associated to the evolution of CO traces by CO_2 reduction which could temporary poison the Pd active sites. Performing recycling tests they found that drying the electrode at room temperature, the oxygen of the air oxidized CO absorbed on Pd restoring the catalytic properties. (32)

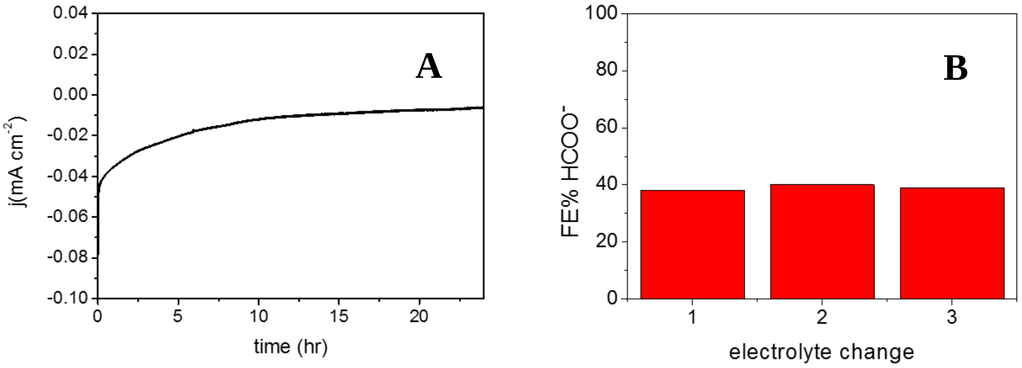

Figure 2.15. A) Current-time profile for Pd@TiO_2/ox-SWCNHs maintained at -0.05 V (vs. RHE). Supporting electrolyte: 0.50 M $NaClO_4$. B) $HCOO^-$ FE% in function of electrolyte change. FE% were calculated over 1 hour of electrolysis in 0.50 M $NaClO_4$ at -0.05V.

As emerged by the preliminary results above presented, the activation of CO_2 on Pd@TiO_2/ox-SWCNHs in both PBS and $NaClO_4$ appears a complex process. The temporary modification/poisoning of the electrocatalyst by adsorption of $HCOO^-$ or minor CO_2 reduction products, with concomitant specific interactions between the TiO_2 porous layer and the electrolyte anions, could drive the adsorption of CO_2 and its activation.

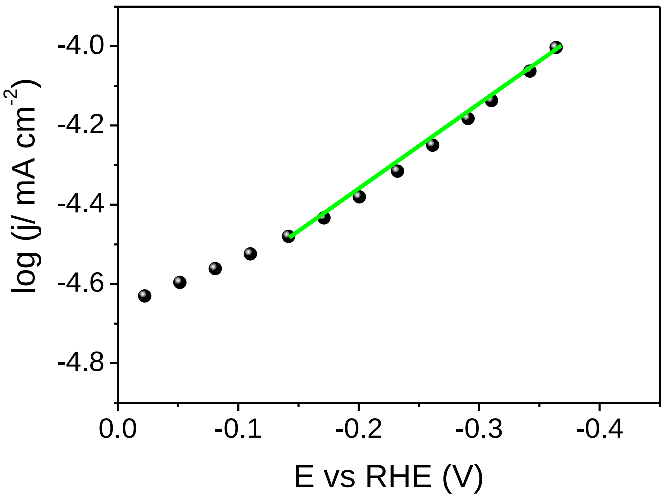

Figure 2.16. Tafel plot obtained on GCE modified Pd@TiO_2/ox-SWCNHs (experimental point (●) and fitting line (–)) in 0.50 M $NaClO_4$ solution under CO_2.

Additional mechanistic aspects for the experiments conducted in $NaClO_4$ were addressed via Tafel analysis (figure 2.16). To evaluate the dependence of the electrocatalytic rate (log j) on the applied potential. In agreement with the findings with PBS, the obtained Tafel plot for the final hybrid Pd@TiO_2/ox-SWCNHs exhibited a slope of 129 mV dec^{-1}, consistent with a mechanism of electrocatalytic hydrogenation of CO_2 mediated by Pd- hydride species.

2.2.1.5. Conclusion

The conversion of CO_2 to $HCOO^-$ is of central importance for innovative carbon-neutral energy schemes. The approach used to design Pd@TiO_2/ox-SWCNHs followed a hierarchical approach, in which each component worked in synergy with the others and with specific functions, driving CO_2 reduction to $HCOO^-$. The hybrid material was synthesized integrating ultra small Pd NPs (diameter of 1.5 nm) inside a TiO_2 shell supported on ox-SWCNHs. All techniques used to characterize Pd@TiO_2/ox-SWCNHs converged toward a perfect interfacing of the three phases, which have resulted in an improved electronic communication. Preliminary catalytic tests have been carried out. CO_2 activation has been investigated in three different electrolytes, emerging that PBS and $NaClO_4$ were the most promising, considering the CO_2 activation potential, -0.05 V in $NaClO_4$ and -0.15 V in PBS. In both the electrolytes the catalytic behavior appears very complex. Examining the catalytic properties in both the electrolytes, the optimal working conditions found were -0.05V in saturated 0.50 M $NaClO_4$, leading to FE% in HCOO- of 40% after 1 hour of bulk electrolysis at fixed potentials. The optimal working potential was very close to the thermodynamic potential, -0.02V where only enzymes are able to perform the conversion of CO_2. A decrease in FE% was observed over time, which could be due to several factors, including the adsorption of the electrolyte anions on TiO_2 surface, the adsorption of CO_2 reduction reaction intermediate onto the active sites, or stationary state decomposition of the as formed formate to release H_2 and CO_2. In any case, recycling experiments of the catalysts with fresh electrolytes indicate that the deactivation towards formate is not irreversible, and that a possible way forward could rely on the design of flow reactors where the electrolyte is continuously fed. More in-depth investigations are currently ongoing.

2.3 Supported Ionic liquid layer as strategy to confined NiCyclam on p-SWCNHs to design novel electrocatalysts for CO_2 reduction

The reduction of CO_2 using water as reduction medium represents an attractive choice because it is economically and environmentally benign. From a reactivity point of view, the presence of water facilitates the proton transport. The main challenge is posed by the competitive reduction of H_2O to H_2, which is kinetically and thermodynamically favored, as already outlined above. Molecular catalysts have been extensively studied because their catalytic properties can be tuned by altering the chemical environment surrounding the metal center. However, the use of homogeneous molecular catalysts in aqueous electrolytes is still not as competitive as resorting to heterogeneous catalysts. $NiCyclam^{2+}$ is a well-known electrocatalyst, highly effective for the conversion of CO_2 to CO. It can produce CO with faradaic efficiency as high as 90% using mercury working electrodes in KCl aqueous solution, (34) (35) (36) (37) or in mixed electrolytes such as acetonitrile/ water 4:1. (38) In the last decades, several groups investigated on the possibility to "heterogenize" molecular catalysts by supporting them onto electrode surfaces for the reduction of CO_2, achieving promising results. (39) (40) (41) Herein, a novel material based on $NiCyclam^{2+}$ is reported, NiCyclam@BMIM/p-SWCNHs, where $NiCyclam^{2+}$ was incorporated inside a matrix of BMIM PF_6, supported onto the surface of pristine carbon nanohorns (p-SWCNHs). BMIM PF_6, is a well-known ionic liquid already used as CO_2 capturing phase, (42) (43) and as solvent for the electrochemical reduction of CO_2 (44) (45). Ionic liquids can selectively interact with CO_2 molecules by means of Lewis acid-base interactions. (46) Supporting ionic liquid can improve the CO_2 trapping ability of the composite material, because the contact area between gas molecules and ILs increases. (9) (10) (11) (12) (47) Interest in ionic liquid is growing because they can act not only as capture interface, but also as co-catalyst lowering the energy of key intermediates, (48) or directly as catalysts. (49) On the other hand, p-SWCNHs nanoscaffolds can improve the electronic communication between the electrode surface and the catalytic sites. The widely available surface provided by the carbon nanostructure has allowed to obtain a material with amounts of electroactive sites per cm^2 higher than $1x10^{-8}$ mol cm^{-2}, which is so far the highest reported in literature. (39)

2.3.1 Results and discussion

2.3.1.1 Synthesis of NiCyclam@BMIM/p-SWCNHs

The synthesis of NiCyclam@BMIM/p-SWCNHs was accomplished using incipient wetting procedures. NiCyclam@BMIM was prepared by dissolving NiCyclam in the solution of $BMIMPF_6$ in anhydrous THF. When the solution appeared homogenous, it was mixed with a suspension of 1mg/mL of p-SWCNHs in anhydrous THF. This mixture has been kept under stirring overnight, and dried by vacuum evaporation. A similar procedure has been used to prepare the reference material BMIM@p-SWCNHs. The right amount of $BMIMPF_6$ solution was mixed with p-SWCNHs dispersion in order to obtain the desired composition. After one night under stirring, the mixture was dried by vacuum evaporation. Using this procedure, a library of materials were synthesized, each with a different concentration of BMIM and different concentration of NiCyclam. The optimized material (from a catalytic point of view) was named NiCyclam@BMIM/p-SWCNHs, with the following nominal percentage: 25% of NiCyclam, 23% of BMIM and 52% of p-SWCNHs.

In NiCyclam@BMIM/p-SWCNHs, the assembly of the three components took advantage of non-covalent forces. p-SWCNHs did not undergo chemical treatment, so that the carbon nano-scaffold completely preserved its π-conjugated structure and therefore the best electronic conductivity, improving the electronic communication between each component. By means of the incipient wetting methods, the $BMIMPF_6$ covered all the pores of the carbon nanostructure leading to a powder material. The electrocatalytically active species (NiCyclam) were guested within the SILP. Due to the ion conductivity property of the $BMIMPF_6$, the SILP worked as an electrical junction between the catalytic sites and the surface of the p-SWCNHs, also assisting the electron transfer.

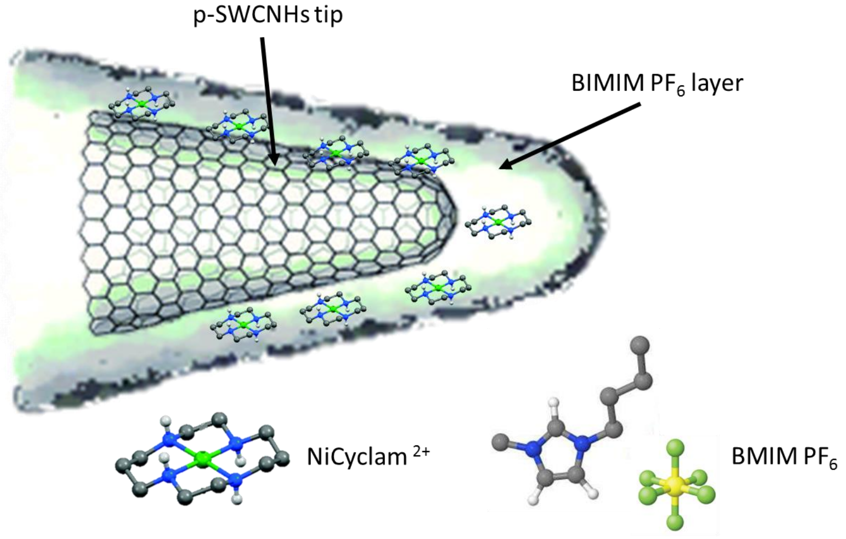

Scheme 2.3: Schematic representation of the NiCyclam@BMIM/p-SWCNHs hybrid. NiCyclam^{2+} is guested inside the ionic liquid layer, which embeds the p-SWCNHs structure. C atoms are grey, H atoms are white, N atoms are blue, P atom is yellow and F atoms are green.

2.3.1.2 Macroscopic characterization

TGA under N_2 was used to analyze the composition of BMIM/p-SWCNHs and NiCyclam@BMIM/p-SWCNHs. From the analysis, the $BMIMPF_6$ content in both material fits well the nominal amount. From the TGA profile, it was also observed that the ionic liquid phase was stable up to 350°C.

Figure 2.17 A reports a comparison between BMIM@p-SWCNHs and neat $BMIMPF_6$. The degradation temperature of the ionic liquid decreased from 430 °C to 340 °C in presence of SWCNHs. The reason for this behavior could be ascribed to the organization of the ionic liquid around the carbon nanostructure surface forming a thin layer on a wide surface. (48) Figure 2.17 B shows the TGA plots of p-SWCNHs, BMIM/p-SWCNHs and NiCyclam@BMIM/p-SWCNHs. In the final hybrid, the degradation temperature of the ionic liquids decreased again from 340 °C to 250°C. In addition to the order induced by the p-SWCNHs, the presence of the Ni catalyst might be responsible for such decrease acting as a hot spot, imparting better heat conduction and favoring the ionic liquid degradation at lower temperature. The degradation of the Cyclam ligand must occur at the same temperature of the BMIM, thus explaining the larger weight loss of the final hybrid as compared to BMIM/p-SWCNHs.

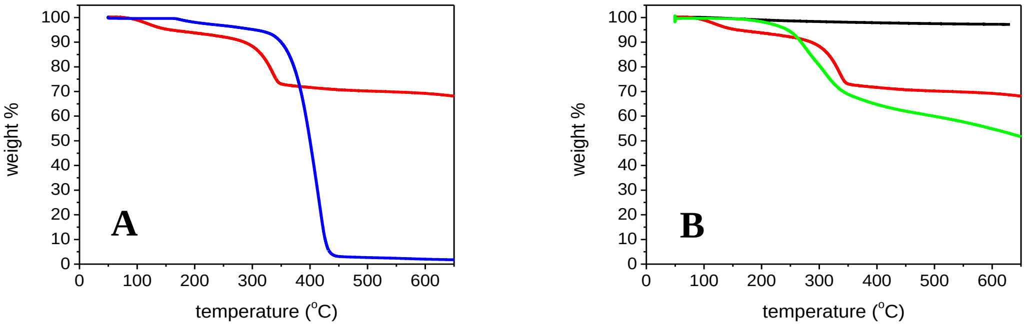

Figure 2.17 A) TGA plots of BMIM@p-SWCNHs (–) and BMIMPF$_6$ neat (–). **B** TGA plots of p-SWCNHs (–), BMIM@p-SWCNHs (–), NiCyclam@BMIM/p-SWCNHs (–).

FTIR analysis conducted on NiCyclam@BMIM/p-SWCNHs, BMIM/p-SWCNHs and p-SWCNHs (Figure 2.18) shows in all the samples a peak relative to OH- stretching, associated with adsorbed water (the commercial BMIMPF$_6$ used contains 3% of water) and umidity of KBr powder used to prepare the samples. The spectra of NiCyclam@BMIM/p-SWCNHs and BMIM/p-SWCNHs exhibited peaks at 3150 cm^{-1} and at 2932-2896 cm^{-1}, characteristic of the stretching of C-H of the imidazole ring and of the alkyl moieties, respectively. The stretching modes of the imidazolium ring, C=N and C=C are present (several peaks around 1640 cm^{-1}), while the peaks around 1570 cm^{-1} were characteristic of the stretching of C-C and C-N of the alkyl chain of the BMIMPF$_6$. The peak at 1174 cm^{-1} was typical of the deformation of the imidazole ring in the plane. Finally, the peaks at 840 cm^{-1} and 541 cm^{-1} were the distinctive stretching modes of the PF$_6^-$ counter-anion of the BMIM: the antisymmetric stretching and the symmetric stretching. (50) p-SWCNHs spectra exhibit characteristic peaks in the range 3250-2850 cm^{-1} due to stretching of C-H, while the peaks in the range between 1750 cm^{-1} and 1450 cm^{-1} were associated to the stretching C=C and C-C bonds.

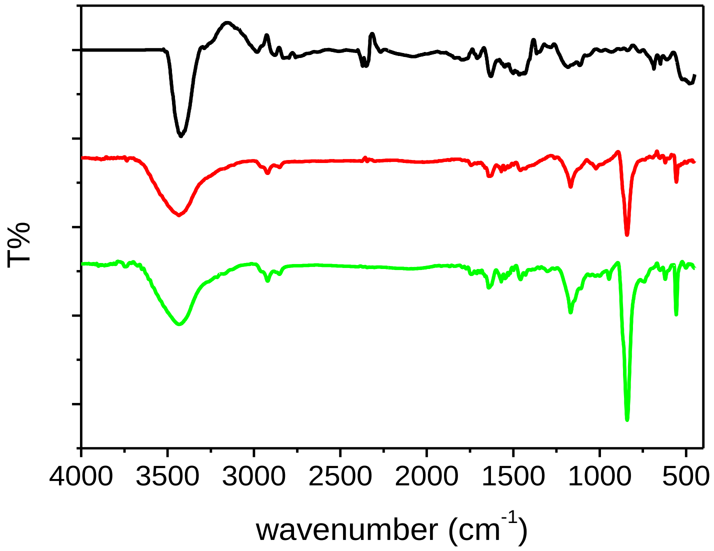

Figure 2.18. FT-IR spectra of the NiCyclam@BMIM/p-SWCNHs (–), BMIM@p-SWCNHs (–), p-SWCNHs (–).

Raman spectra of the three samples are reported in figure 2.19. The Raman shifts of D and G bands did not change after the addition of BIMIM layer, and the D/G ratio remained constant 1.03±0.02, a sign that there was no damage of the polyaromatic framework after the material assembly. This is consistent with a non-covalent functionalization of the p-SWCNHs. The other signature bands of the SWCNHs (2D and D+D') were also detected. It must be noted that the presence of BMIM on the SWCNHs results in a broadening of the nanocarbon characteristic peaks.

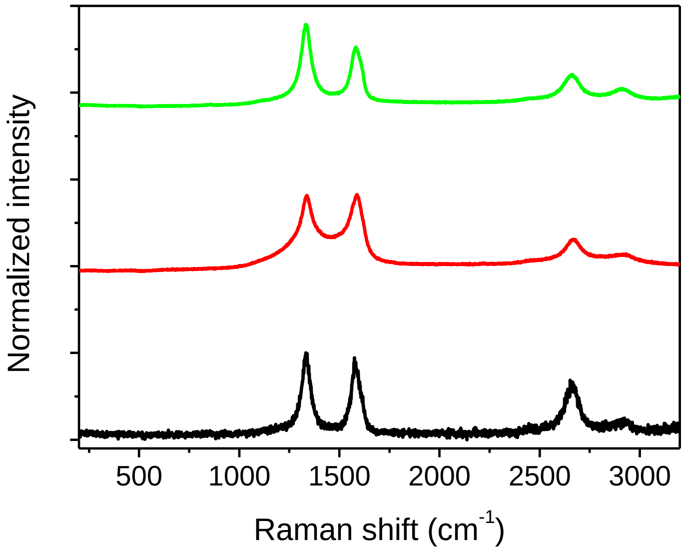

Figure 2.19. Raman spectra of the NiCyclam@BMIM/p-SWCNHs (–), BMIM@p-SWCNHs (–), p-SWCNHs (–).

2.3.1.3 Electrochemical characterization

The redox behavior of NiCyclam@BMIM/p-SWCNHs was investigated by CV and LSV. Figure 2.20 reports a comparison between the GCE modified with p-SWCNHs (A), with BMIM/p-SWCNHs (B), and with NiCyclam@BMIM/p-SWCNHs (C).

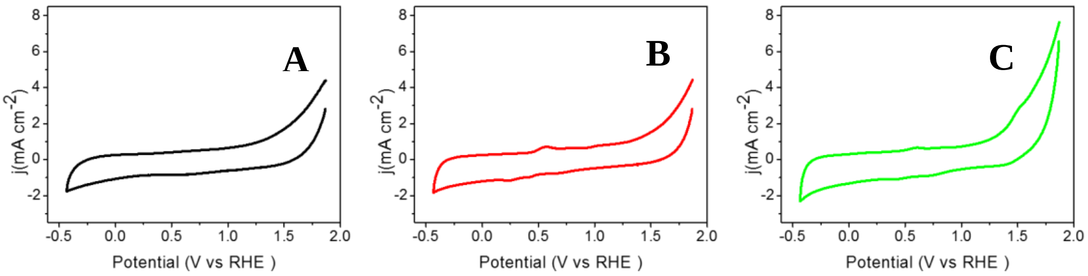

Figure 2.20. CVs obtained on GCE modified with A) p-SWCNHs (–), B) BMIM@p-SWCNHs (–) and C) NiCyclam@BMIM/p-SWCNHs (–) in 0.5M $NaHCO_3$ under N_2, scan rate: 0.025V s^{-1}.

The profile for p-SWCNHs/GCE (black trace) was associated only with a capacitive current, while that for BMIM/p-SWCNHs (red trace), showed the appearance of two peaks due to the reduction and oxidation of $BMIMPF_6$. (49) For NiCyclam@BMIM/p-

SWCNHs, in addition to the peaks relative to the reduction/oxidation of $BMIMPF_6$, an anodic peak at 1.61 V vs RHE was observed, which arouse from the oxidation of NiCyclam, with Ni(II) oxidized to Ni(III). (38) The charge involved in the oxidation process of Ni(II) to Ni(III) has been obtained integrating the oxidation peak by the CVs. Using the charge value, the surface concentration of NiCyclam (**Γ**) and the number of active sites onto the electrode surface for the final material was calculated using the following equations:

$$\Gamma = \frac{Q}{nFA}$$

$$number\ of\ active\ sites = N_A\Gamma$$

Where Q is the charge involved in the oxidation of Ni(II) to Ni(III), n is the number of electron involved, F is the Faraday constant 96485 C mol^{-1}, A is the geometric area of the electrode and N_A is the Avogadro numbers 6.02 x 10^{23} mol^{-1}.

The value obtained is **Γ** (2.7±0.2) $x10^{-7}$ mol/cm^2 correspondent to (1.6±0.1) $x10^{17}$ $sites/cm^2$. Hence, the corresponding percentage of electroactive catalyst respect to the nominal amount used during the synthesis was 60%. The heterogenization of a molecular catalyst is very challenging, however it brings numerous advantages such as high selectivity, easier products separation and opportunity to work in aqueous medium. These advantages were highlighted in several recent reports. For example, Kang et al reported an iridium pincer dihydride catalyst supported on carbon nanotube surface via the π-π stacking of a pyrenic moiety. The catalyst was able to convert CO_2 into formate with a FE of 96%. (51)Ling et al. reported a Co porphyrin combined with a covalent organic framework, and despite the percentage of active site relative to the nominal amount was only 4% and **Γ**=$1x10^{-8}$ mol cm^{-2}, the catalyst proved to be catalytically active for CO_2 reduction to CO with FE of 90%. (41) In another interesting work, a functionalized Fe porphyrin was anchored to a modified MWCNT/GCE by means of a pyrenic moiety and successfully used to catalyze the CO_2 reduction to CO with FE of 90%. In this case, the **Γ** was of $2.4x10^{-8}$ mol cm^{-2} (40). Another Fe-porphyrin was combined with a metal organic frameworks (MOF) active in CO_2 reduction to CO with **Γ**=$6.2x10^{-8}$ mol cm^{-2} and FE of 54%. (39)

Most of the examples above reported a surface concentration lower than NiCyclam@BMIM/p-SWCNHs. To the best of our knowledge, there are no heterogenized molecular electrocatalysts for the CO_2 reduction with a surface concentrations higher than 1 x 10^{-7} mol/cm^2, highlighting the advantages of the SILP strategy to achieve a surface rich with widely available active sites for the CO_2 reduction process.

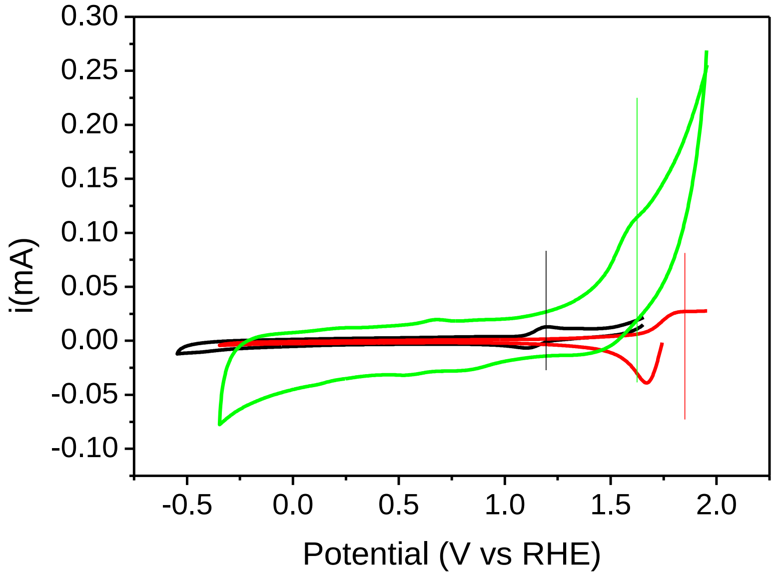

Figura 2.21. CVs obtainend on bare GCE in 0.5mM NiCyclam in 0.50 M $NaHCO_3$ (–), on GCE modified with NiCyclam@BMIM (–) and NiCyclam@BMIM/p-SWCNHs (–). Scan rate 0.025V s^{-1}

Further insights in the redox behavior of the $NiCyclam^{2+}$ when embedded into the $BMIMPF_6$ were gained through additional cyclic voltammetry experiments. The collected traces are reported in figure 2.21. Figure 2.21 shows the comparison between $NiCyclam^{2+}$, $NiCyclam^{2+}$@$BMIMPF_6$/p-SWCNHs/GCE and $NiCyclam^{2+}$@$BMIMPF_6$/GCE in 0.5M $NaHCO_3$ solution. From the CVs, the role of the carbon nanostructure appeared clear: p-SWCNHs can affect the redox behavior of the $NiCyclam^{2+}$, decreasing the energy for its oxidation. The pentagon moieties at the apex of each cone in p-SWCNHs are characterized by a higher density of negative charge, (52) that can affect the potential at which the Ni(II) oxidation is observed.

2.3.1.4 CO_2 activation

Catalytic CO_2 reduction was first investigated by LSV experiments. Figure 2.22 shows the different response of p-SWCNHs (A), BMIM@p-SWCNHs (B) and NiCyclam@BMIM/p-SWCNHs (C) modified GCE in CO_2 saturated solution (red trace) in comparison with the response in N_2 saturated solution (black trace) in 0.5M $NaHCO_3$ saturated. The activation has been investigated in the potential window ranging from 0.6 V to -1.15V vs RHE using a scan rate of 0.025 V s^{-1}. The polarization curve collected with p-SWCNHs exhibited a negligible current increase and a shift of the LSV trace in presence of CO_2 that could be ascribed to lowering of pH upon CO_2 bubbling. The pH of the buffer decrease from 8.4 to 7.4.

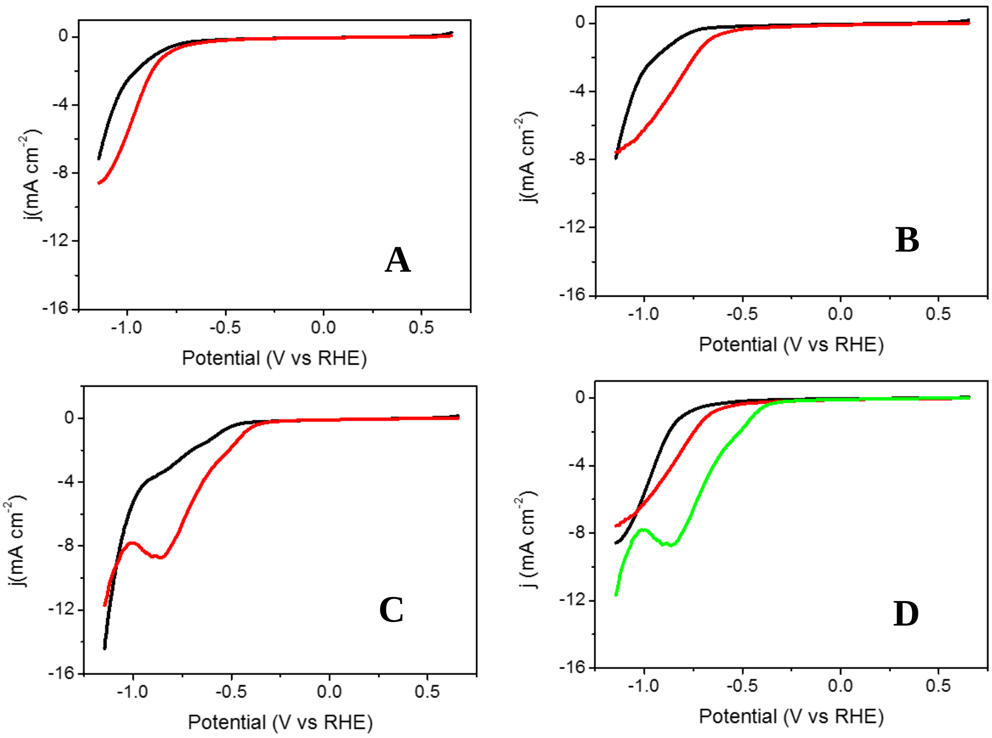

Figure 2.22. CVs at GCE modified with p-SWCNHs (A), BMIM@p-SWCNHs (B) and NiCyclam@BMIM/p-SWCNHs with (C) in N_2 (–) and CO_2 (–) saturated 0.1 M phosphate buffer solution pH 7.40. Scan rate: 0.025V s^{-1}. (D) Comparison of CO_2 activation between p-SWCNHs (–), BMIM@p-SWCNHs (–) and NiCyclam@BMIM/p-SWCNHs (–), 0.5M $NaHCO_3$ solution. Scan rate: 0.025V s^{-1}.

When $BMIMPF_6$ was supported onto p-SWCNHs, to give the SILP, the onset of the catalytic wave in CO_2-saturated system moved to -0.68±0.03V vs RHE. When the ionic liquids are supported, they can increase the contact area between the gas and the IL, presenting lower viscosity and higher stability. (11) (12) (47) Supporting $BMIMPF_6$ allowed to study the reduction of the CO_2 in water. As expected, $BMIMPF_6$ can activate the CO_2, the increase in current and the shift in potential of the LSV could be due to CO_2 coordination and activation. When a negative potential is applied to the ILs, they undergo a structural transition that occurs regardless of CO_2 presence. At enough negative potentials, the ILs organize themselves in order to have an overabundance of cation at the electrode surface and a higher degree of alignment. CO_2 interacts with the anions exposed which entrap it. The onset of the CO_2 reduction is dependent on this structural transition. (53) By supporting $BMIMPF_6$ onto the p-SWCNHs, the transition started at more positive potential than bulk ILs as literature reported. (54)

After including of NiCyclam^{2+} into SILP, the response towards CO_2 activation resulted in a significant enhancement of the catalytic current and onset potential. In particular, a well defined peak can be observed, associated to the CO_2 reduction process. Hence, Figure 2.20 C confirms that NiCyclam^{2+} preserved its catalytic activity even when transferred into the $BMIMPF_6$ layer. The catalytic current of the material containing NiCyclam^{2+} was doubled with respect to that with BMIM@p-SWCNHs/GCE and five times higher than that with p-SWCNHs/GCE. The CO_2 onset potential shifts to less cathodic potential, -0.58±0.01V vs RHE. Figure 2.20 D reports the comparison between p-SWCNHs, BMIM/p-SWCNHs and NiCyclam@BMIM/p-SWCNHs, proving the promising features of the designed catalysts.

As the results evidenced, the hybrid material showed comparatively the best characteristics for a CO_2 electrocatalyst, in virtue of the resulting multifunctional structure: a) a CO_2 capture phase opportunely supported onto a graphene based material able to provide a wide surface increasing the contact between the ionic liquid and the CO_2 molecules, as well as improving electron transfer processes. b) NiCyclam^{2+} molecules confined into the ionic liquid layer, enhancing the efficiency of the catalyst for the CO_2 activation; c) each phase is in intimate contact with the others, securing a synergistic effect driving the cascade of catalytic events.

To verify if NiCyclam^{2+} retained its selectivity, bulk electrolysis experiments have been performed, using the same 3-electrode cell configuration described earlier. The working electrode has been prepared by drop casting of two drops (100 µL each one, one per side) of NiCyclam@BMIM/p-SWCNHs aqueous dispersions on rectangular slides of glassy carbon. (more details on electrode preparation are reported in Appendix A). The counter electrode was a Pt electrode while an Ag/AgCl electrode functioned as the reference electrode. In order to recognize the gas products, the experiments have been performed in tandem with GC analysis connected in line, thus analyzing the presence of gaseous reduction products in the head-space (HS) of the electrochemical cell. The gas flow used to saturate the electrochemical cell with CO_2 was 20 mL min^{-1}.

The fixed potential chosen for the bulk electrolysis was -0.69 V because it was the value corresponding to the best FE. By the bulk electrolysis experiment conducted in 0.1M $NaHCO_3$ solution it emerged that the solely evolved product was the CO with a faradaic efficiency (FE%) of 54% after 1hr of electrolysis. The rest of the charge was involved in H_2 production. The current-time profile was constant throughout the experiment, with an average density current of -0.75mA cm^{-2} corresponding to 4mA mg^{-1} of catalyst and 36mA mg^{-1} of Ni calculated on the amount of catalyst supported and the nominal amount of Ni in the catalyst supported onto the electrode surface respectively. Bulk electrolysis experiments longer than 1hour have evidenced a decrease of FE CO with concomitant decrease of current. FE in CO was 15% after 2hours and around 8% after 3hours. This behavior could be associated to deactivation of the electrocatalyst inside the ionic liquid layer due to the evolution of carbonyl species.(56) Preliminary experiments were performed in 0.10 M PBS, but the FE in CO was much lower (around 5%), with the HER process becoming largely dominant. ILC analysis and NMR spectra on the liquid phase revealed no formation of other CO_2RR products in the liquid phase, highlighting the retention of selectivity of the catalyst. No reduction product was detected with the reference materials p-SWCNHs and BIMIM@p-SWCNHs.

2.3.1.5 Conclusion

A novel electrocatalytic hierarchical nanostructured material has been synthesized for the CO_2 reduction reaction. NiCyclam@BIMIM/p-SWCNHs was obtained by exploiting supramolecular interaction between each component. The supporting of $BMIMPF_6$ on SWCNHs provided a selective capture phase for the CO_2 adsorption and the reaction medium for NiCyclam molecules. The application of SILP as strategy for the heterogenization of a molecular catalyst has allowed to achieve the highest amount of active sites per cm^2, 2x 10^{-7} mol cm^{-2}. By preliminary studies on the catalytic properties, the results suggested that NiCyclam remained active towards CO_2 reduction, as CV experiments confirmed. The selectivity of the catalyst is high towards CO, with a FE over 1hr of bulk electrolysis of 54%, while HER appears to be a highly competitive process. These findings may inspire the investigation of “heterogenization” of other molecular catalysts allowing studies in aqueous media. Compared with other strategies reported in literature, such as MOF synthesis and chemical functionalization of molecular catalyst with anchoring moieties, the application of SILP is easier and simultaneously allows to achieve high amounts of active catalytic sites to boost the CO_2 activation.

2.4 Reference.

1. C. Amatore, J. M. Saveant *J. Am. Chem. Soc.,* **1981**, Vol. 103, p. 5021-5023.

2. Sullivan, B. P*., Electrochemical and Electrocatalytic Reduction of Carbon Dioxide*. Amsterdam : Elsevier, **1993.**

3. F. A. Armstrong, J. Hirst, *PNAS*, **2011**, Vol. 108, p. 14049-14054.

4. D. H. Wong, C. H. Choi, J. Chung, M. W. Chung, E. H. Kim, S. I. Woo, *Chem. Sus. Chem.,* **2015**, Vol. 8, p. 3092-3098.

5. J. Qiao, M. Fan, Y. Fu, Z. Bai, C. Ma, Y. Liu, X. D. Zhou, *Electrochimica Acta*. ,153, p. 559-563.

6. S. Sen, D. Liu, R. Palmore, *ACS Catal*., **2014**, Vol. 4, p. 3091-3095.

7. C. Cadena, J. L. Anthony, J. K. Shah, T. I. Morrow, J. F. Brennecke, E. J. Maginn, J. *Am. Chem. Soc.,* **2004**, Vol. 126, p. 5300-5308.

8. E. D. Bates, R. D. Mayton, I. NTai, J. H. Davis, *J. Am. Chem. Soc*., **2002**, Vol. 124, p. 926.

9. R. E. Baltus, R. M. Counce, B. H. Culbertson, H. Luo, D. W. DePaoli, S. Dai, D. C. Duckworth, *Sep. Sci. Technol*., **2005**, Vol. 40, p. 525-541.

10. US20070084344A1, **2007**.

11. S. Hanioka, T. Murayama, T. Sotani, M. Teramoto, H. Matsuyama, K. Nakashima, M. Hanaki, F. Kubota, M. Goto*, J. Memb. Sci*., **2008**, Vol. 314, p. 1-4.

12. S. Shishatskiy, J. R. Pauls, S. Pereira Nunes, K.-V. Peinemann, J. Memb. Sci., **2010**, Vol. 359, p. 44-53.

13. Furmaniak et al., **2013***, Phys. Chem. Chem. Phys*., Vol. 15, p. 16468-16476.

14. T. Fujimoro, K. Urita, Y. Aoki, H. Kanoh, T. Ohba, M. Yudasaka, S. Iijima, K. Kaneko*, J. Phys. Chem. Lett. C.*, **2008**, Vol. 112, p. 7552-7556.

15. A. Dumitru, M. Mamlouk, K. Scott*, Electrochim. Acta*, **2014**, Vol. 135, p. 428-438.

16. M. Ran, W. Sun, Y. Liu, W. Chu, C. Jiang*, J. Solid. State Chem*., **2013**, Vol. 197, p. 517-522.
17. F. Tian, Y. Zhang, J. Zhang, C. Pan*, J. Phys. Chem. C.*, **2012**, Vol. 116, p. 7515-7519.

18. J. Shen, B. Yan, M. Shi, H. Mea, N. Li, M. Ye, *J. Mater. Chem.,* **2011**, Vol. 21, p. 3415-3421.

19. U. J. Kim, C. A. Furtado, X. Liu, G. Chen, P. C. Eklund, *J. Am. Chem. Soc*., **2005**, Vol. 127, p. 15437-15445.

20. G. K. Ramesha, J. F. Brennecke, P. V. Kamat, *ACS Catal*. **2014**, Vol. 4, p. 3249-3245.

21. A. H. J. P. Y. N. Z. Robert Liang, *Nano Micro Lett.,* **2013**, Vol. 5, p. 202-212.

22. M. Grolm, M. Lukaszewski, G. Jerkiewicz, A. Czerwinski, *Electrochim. Acta*, **2008**, Vol. 53, p. 7583-7598.

23. K. Chem, D. Cao, F. Yang, L. Zhang, Y. Xu, G. Wang*, J. Mater. Chem*, **2013**, Vol. 5, p. 202-212.

24. A. Dutta, J. Datta, *J. Mater Chem A,* **2014**, Vol. 2, p. 3237-3250.

25. M. R. Thonson, K. I. Sill, P. J. A. Kenis*, J. Electrochem. Soc*., **2013**, Vol. 160, p. F69-F74.

26. S. Verma, X. Lu, S.Ma, R. Masel, P. Kenis, *Phys. Chem. Chem. Phys*., **2016**, Vol. 18, p. 7075-7084.

27. C. Comninellis, G. Chen*. Electrochemistry for the Environment*, New York : Springer, **2010**.

28. M. Xiaoquan e M. W. *Journal of the American Chemical Society*, **2015***,* Vol. 137, p. 4701-4708.

29. Y. Hori, A. Murata, R. Takashi, *J. Chem. Soc. Faraday Trans*., **1989,** Vol. 85, p. 2309-2326.

30. J. J. Wu, F. G. Risalvato, F. S. Ke, P. J. Pellecchia, X. D. Zhou*, J. Electrchem. Soc.,***201**2, Vol. 159, p. F353-F359.

31. J. Sanchez, J. Augustynski*, J. Electroanal. Chem*.,**1979**, Vol. 103, p. 423-426.

32. X. Min, M. W. Kanan, *J. Am. Chem. Soc.*,**2015**, Vol. 137, p. 4701-4708.
33. Y. Chen, C. W. Li, M. W. Kanan, *J. Am. Chem. Soc***., 2012**, Vol. 134, p. 19969-19972.

34. X. Min, M. W. Kanan*, J. Am. Chem. Soc*., **2015**, Vol. 137, p. 4701-4708.

35. J. P. Collin, A. Jouaiti, J. P. Sauvage, *Inorg. Chem*. **1988**, Vol. 27, p. 1986.

36. M. Beley, J. P. Collin, R. Ruppert, J. P. Sauvage*, J. Chem. Soc. Chem. Commun*, **1984**, p. 1315.

37. G. Neri, J.J. Walsh, C. Wilson, A. Reynal, J. Y. C. Lim, X. Li, A. J. P. White, N. J. Long, j. R. Durrant, A. J. Cowan*, J. Phys. Chem. Chem. Phys*., **2015**, Vol. 17, p. 1562.

38. G. Neri, I. M. Aldous, J. J. Walsh, L. J. Hardwick, A. J. Cowan, *J. Chemical Science*, **2016**.

39. J. D. Kubiack, C. P. Froelich, *Inorg. Chem*., **2012**, Vol. 51, p. 3932.

40. I. Hod, M. D. Sampson, P. Deria, C. P. Kubiak, O. K. Farha, J. T. Hupp, *ACS Catal,* **2015,** Vol. 5, p. 6302-6309.

41. A. Maurin, and M. Robert, *J. Am. Chem. Soc*., **2016**, 138, p. 2492–2495.

42. S. Lin, C. S. Dierks, Y. Zhang, N. Kornienko, E. M. Nichols, Y. Zhao, A. R. Paris, D. Kim, P. Yang, O. M. Yaghi, C. J. Chang, *Science*, **2015**, Vol. 349, p. 1208-1213.

43. R. E. Baltus , B. H. Culbertson , S. Dai , H. Luo , D.W. DePaoli, *J. Phys. Chem*. B, **2004**, Vol. 108, p. 721-727.

44. J. E. Bara, C. J. Gabriel, T. K. Carlisle, D. E. Camper, A. Finotello, D. L. Gin, R. D. Noble, *Chem. Eng. J*, **2009**, Vol. 147, p. 43-50.

45. Y. Oh, X. Hu, *Chem. Commun*., **2015**, Vol. 51, p. 13698-13701.

46. A. M. Rizzuto, R. Pennington, K. Sienerth, *Electrochim. Acta*, **2011**, Vol. 56, p. 5003-5009.

47. S. Baranton, D. Bélanger, *J. Phys. Chem*. B, **2005**, Vol. 109, p. 13847-1850.

48. a) R. Fehrmann, A. Riisager, M. Haumann. *Supported Ionic Liquids: Fundamentals and Applications.* s.l. : John Wiley & Sons Inc. , **2014**, b) M. Tunckol, J. Durand, P. Serp, Carbon, 2012, 50, 4303-4334

49. B. A. Mello*, J. Phys. Chem. Lett.,* **2014**, Vol. 5, p. 2033-2038.
50. A. B. Bocarsly, Q. D. Gibson, A. J. Morris, R. P. L'Esperance, Z. M. Detweiler, P. S. Lakkaraju, E. L. Zeitler, T. W. Shaw, *ACS Catal*. **2012**, Vol. 2, p. 1684-1692.

51. P. Kang, S. Zhang, T. J. Meyer, M. Brookhart, *Angew. Chem.* Int. Ed. **2014**, Vol. 53, p. 8709-8713.

52. S. Berber, Y. Kwon, D. Tomanek, *Physical Review B.* **2000,** Vol. 62, p. R2291-R2294.

53. N. G. Rey, D. D. Dlot, *J. Phy. Chem. C.* ***2015***, Vol. 119, p. 20892–20899.

54. I. Reche, G. Guirado, *RSC Adv*. **2014**, Vol. 4, p. 65176-65183.

55. H. A. Scharz, C. Creutz, N. S. Sutin, *Inorg. Chem*, **1985,** Vol. 24, p. 433-439.

56. J. D. Frohelich, C. P. Kubiack, *J. Am. Chem. Soc.,* **2015**, 137, 3565-3573

CHAPTER 3

Novel carbon nanostructured based hierarchical material as electrocatalysts for oxygen reduction reaction (ORR)

3.1 Introduction

There is currently a great deal of attention to the manufacturing of novel electrocatalysts for the O_2 activation, which is a process of high relevance for the construction of fuel cells. Fuel cells are electrochemical power source devices, where two half-reactions occurring at two separate electrodes, allowing the production of energy in the form of electricity. The anodic reaction involves the oxidation of some fuel (hydrogen, alcohols etc) while at the cathode the generally employed half reaction is the ORR. Even using Pt based catalysts, the 80% of the losses in hydrogen/oxygen fuel cells are due to loss of efficiency of the ORR electrocatalyst, therefore it turns out that ORR is generally the bottleneck in fuel cells development. (1) When developing a new electrocatalytic system for O_2 reduction, the challenges faced are multiple, as well as the factors to consider for obtaining good activity and selectivity. The energetic barrier for the first electron transfer is very high and low selectivity by most catalysts is normally observed. Moreover, there is a strict dependence on the pH that affects the reaction mechanism and consequently the products distribution. The main reduction products obtained by O_2 reduction are H_2O and H_2O_2, corresponding respectively to a 4e- reduction process and a 2e- reduction process. Both products can be useful from an energy point of view, specifically for fuel cell developing. H_2O_2 bears added value, being a highly relevant compound for several industrial sectors such as pulp and paper, food, mining, textile bleaching, waste water treatment, packaging and chemical synthesis. (2) Currently, Pt/C catalysts are the benchmark electrocatalysts for the selective reduction of O_2 to H_2O (3) (4) (5)), while there are still few examples of electrocatalysts for the selective reduction of O_2 to H_2O_2. Among them, Au-Hg and Pt-Hg have been identified as the most promising candidates leading to highly selective H_2O_2 formation. (6) However, it can be reasonably thought that the industrial viability of these catalysts is hampered by the high cost and low availability of noble metals, combined with a low long-term stability and easy poisoning.

This chapter focuses on the preparation, characterization and employment of two hierarchical nanocatalysts for ORR : a) carboxylated Fe-filled multiwalled carbon nanotubes (t-Fe@MWCNTs) and b) N-doped graphitized carbon nanohorns (g-N-CNHs). Both catalysts share the important characteristic of being noble metal free. As shown in more details below, these two systems showed different selectivity towards the O_2 reduction: t-Fe@MWCNTs was selective for H_2O production, while g-N-CNHs showed high selectivity for H_2O_2 production.

The precursor material of t-Fe@MWCNT, Fe-filled multiwalled carbon nanotube (Fe@MWCNTs), was provided by Prof. Bonifazi's group, which was co-partner in a European project, the Self-Assembly in Confined Space (SACS) project.

g-N-CNHs is a N-doped metal free nanomaterial based on SWCNHs prepared and supplied by Dott. Daniel Iglesias Esperillias.

3.2 Carboxylated Fe-filled MWCNTs (t-Fe@MWCNTs) for ORR

As mentioned above, the benchmark catalyst for this reaction is the E-TEK catalyst (20% Pt/C). (7) (8) (9) Pt is expensive, due to the low availability and geopolitical dependence of Pt, and it also suffers by low tolerance to most fuel impurities, therefore it is not stable for long-term use. (7) (8) (9) All these reasons have driven many research groups to develop more abundant metals based electrocatalysts, which could be less active than Pt but surely cheaper.

The application of Fe-based catalysts for the ORR has emerged as an interesting alternative. This metal is very effective for the ORR catalysis and has been investigated as active center in macrocycle compounds and as Fe-based hybrid nanostructured materials. (10) However, the non-precious metal catalysts generally suffer from poor stability in acidic conditions, frequently adopted for ORR, due to leaching of the metal. Several strategies have been devised to circumvent this problem.

Bao et al., investigated a Fe-Pt/C system where Fe-particles were encapsulated into Pt shells. When Fe was confined into Pt shells, the coordinatively unsaturated ferrous sites were highly active and stable in driving O_2 reduction to H_2O in acidic environment. The conjugation of Fe with Pt, could be a way to decrease Pt amounts, and exploit the interplay between Fe and Pt, achieving activity and durability comparable to Pt/C. (11) Using a similar structural concept, they extended the study to a system based on Fe encapsulated within Pod-like carbon nanotubes (CNTs) demonstrating that physically isolated Fe into single walled CNTs (SWCNTs) avoided Fe-leaching, even under strong acidic environment without hindering the catalytic sites availability for the ORR, and avoiding the use of precious metals, such as Pt. Moreover, the use of CNTs improved the electronic communication between the electrode surface and the catalytic sites on which O_2 activation occurs. (12) Recently, it was reported that the number of walls of CNTs can influence the electronic transfer rate and the catalytic properties of CNTs (13) , thus the investigation of the catalytic behavior of encapsulated Fe into MWCNTs could have interesting consequences to deepen the knowledge about the behavior of Fe confined in carbon nanostructures.

Here, the synthesis and the ORR catalytic activity of t-Fe@MWCNTs are reported. Fe was encapsulated in the inner cavity of MWCNTs. The sidewalls of the MWCNTs were then covalently modified with polar groups, as it was envisioned that appropriate engineering of the surface of CNT could cause an enhancement of performance. The electrocatalysis of ORR was investigated at physiological pH. Such pH conditions are not usually studied, but it is of great interest for engineering of various biologically compatible devices including microbial fuel cells. (14) (15) (16)

3.2.1 Result and discussion

3.2.1.1 Synthesis

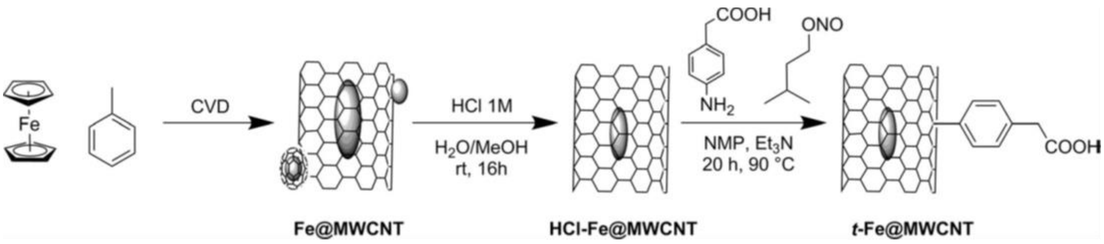

Scheme 3.1: Synthetic procedure for t-Fe@MWCNTs.

The pristine material, Fe@MWCNTs, was prepared by chemical vapour deposition (CVD) in an oven at 1173K using ferrocene (Cp_2Fe) as catalyst and Fe precursor (sublimated at 623 K), and toluene as additional carbon source. The material, as obtained, was purified by unreacted Cp_2Fe and metallic Fe aggregates adsorbed, washing it first in EtOH (to remove Cp_2Fe) and then with 1M HCl in MeOH/H_2O (3/1 v/v) (to remove exohedral Fe). Once purified, Fe@MWCNTs, named HCl-Fe@MWCNTs has undergone the exohedral functionalization by means of radical addition of benzylic acid moieties using the procedure reported by Tour and Bahr (17). The diazonium salts, prepared in situ by para-aminophenylacetic acid in presence of isoamyl nitrite and Et_3N in N-methylphenantroline, reacted with the outer wall of the HCl-Fe@MWCNTs introducing the acidic moieties. This strategy was applied in place of the more common oxidation, as the latter would induce CNTs tips opening (18), which was detrimental for our purpose because it would lead tothe escape of Fe out of the nanotubes. The final material was named t-Fe@MWCNTs. The scheme of the synthesis is reported above (scheme 3.1).

3.2.1.2 Macroscopic and microscopic characterization

Fe@MWCNTs , HCl-Fe@MWCNTs and t-Fe@MWCNTs, were fully characterized using several techniques.
To confirm the successful exohedral functionalization and to know the amount of Fe in the inner cavity, thermogravimetric analysis (TGA) were performed (figure 3.1). In order to more accurately evaluate the functionalization degree of the outer wall of t-Fe@MWCNTs, TGA was performed under N_2 flow. In figure 3.1 (A) a weight loss of 3.5% at 180°C revealed the presence of organic functional groups. In comparison, HCl-Fe@MWCNTs did not show appreciable weight loss indicating that the treatment with diluted HCl acid did not introduce any functional group . TGA under air flow was instead performed to estimate the amount of iron in the inner cavity of Fe@MWCNTs. The air flow induces the combustion of all the carbonaceous components, leaving the most stable metal oxide. The residual weight associated to Fe was 31 wt%. The percentage of Fe decreased to 27 wt% after the washing in HCl, suggesting the removal of non-encapsulated iron. The Fe content did not change after the exohedral functionalization, confirming that the reaction did not cause any leaching of the metal.

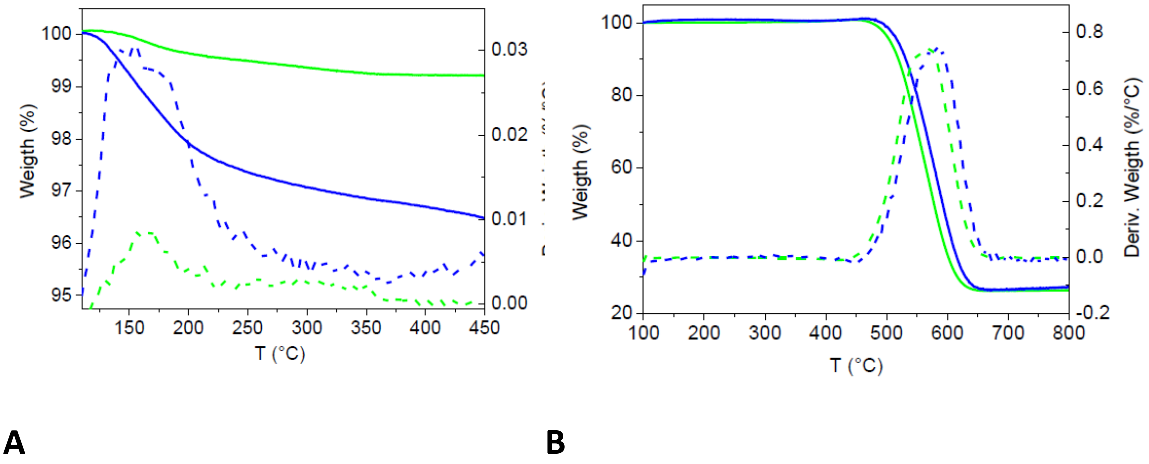

Figure 3.1: A) TGA plots of the HCl-Fe@MWCNTs (-) and t-Fe@MWCNTs (-) under N_2 flow; B) TGA plots of the HCl-Fe@MWCNTs (-) and t-Fe@MWCNTs (-) under air flow.

Raman spectroscopy and FT-IR spectroscopy revealed the successful incorporation of the benzylic acid functional groups.

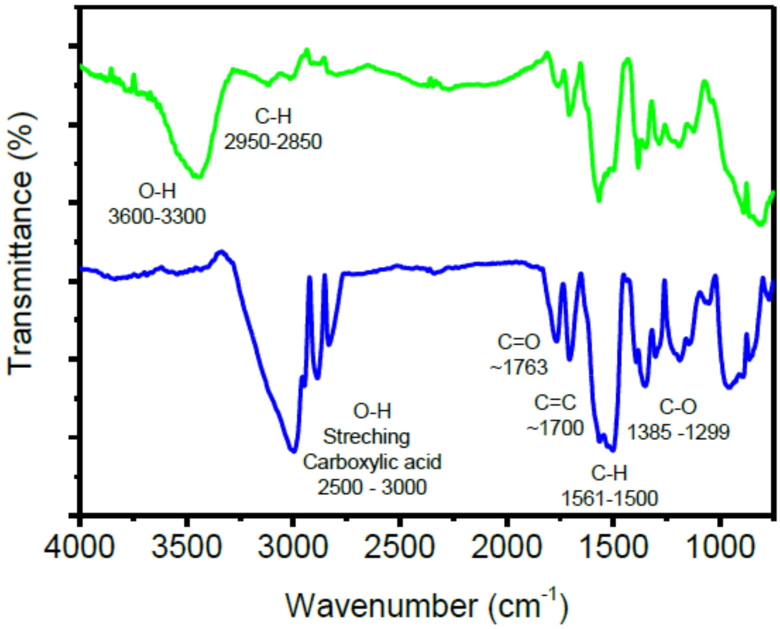

Figure 3.2: comparison between FTIR spectra of HCl-Fe@MWCNTs (-) and t-Fe@MWCNTs (-).

In figure 3.2 the comparison between IR spectra of HCl@Fe@MWCNTs and t-Fe@MWCNTs is reported. The t-Fe@MWCNTs spectrum was consistent with the benzylic acid moieties functionalization. At 3000-3500 cm^{-1} the broad band of the stretching mode for the carboxylic acid O–H group was present; the peaks at 2950 and 2850 cm^{-1} were related to the asymmetric and symmetric stretching of C–H bond; finally, the peak at 1700 cm^{-1} was due to the aromatic C=C stretching mode.

Raman analysis of HCl-Fe@MWCNTs and t-Fe@MWCNTs showed the typical fingerprint of MWCNTs framework: the defect-induced D band at 1351 cm^{-1}, the sp2 vibrational mode induced G band at 1588 cm^{-1}, and the D band harmonics D' at 1627 cm^{-1}, and 2D at 2702 cm^{-1}. No peaks associated to Fe oxides were observed, indicating that none of the reaction step cause oxidation of the metal phase, and that the CNTs act as an efficient protecting barrier.

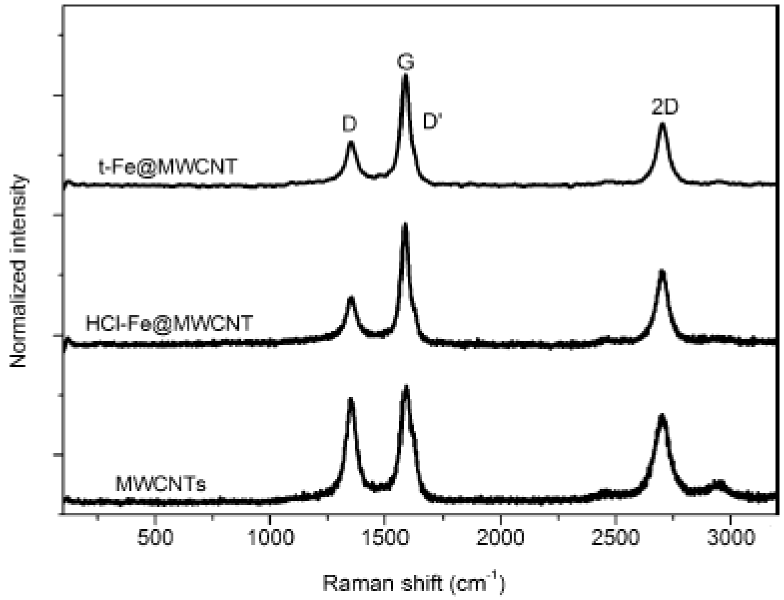

Figure 3.3: Raman spectra of MWCNTs, HCl-Fe@MWCNTs and t-Fe@MWCNTs.

To further investigate on the nature of the iron phase, powder (P) XRD and ^{57}Fe Mössbauer spectroscopy have been performed at Namur University facilities.

PXRD spectra reported in figure 3.4, have been carried out on the three different samples in order to study the iron phases and their changes after each synthetic step. The findings suggested that Fe was present as three different phases: α-Fe, γ-Fe and Fe-carbide. In the as-obtained Fe@MWCNTs, the peak of α-Fe was clearly evident (peak at 44.6° overlapping with Fe-carbide peak), and its intensity decreased after the HCl treatment. No more changes occurred in the (P) XRD spectra after the exohedral functionalization, implying that this treatment did not cause the opening of the tips, with subsequent leaching of Fe from the inner cavity of the nanotubes, in agreement with TGA analysis.

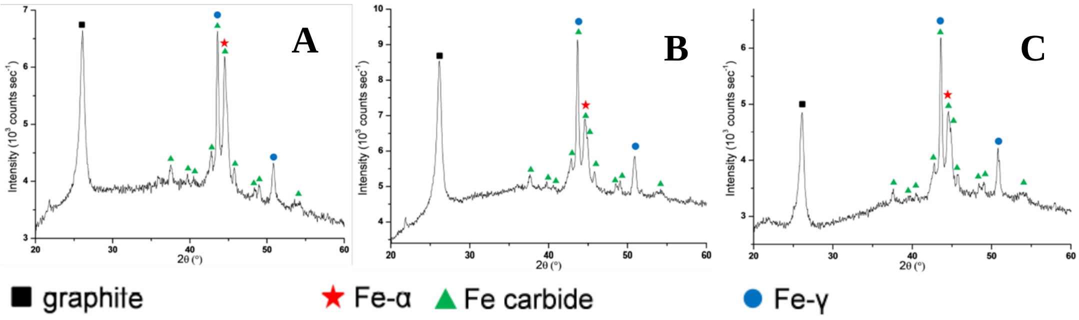

Figure 3.4: PXRD spectra of a) Fe@MWCNTs , b) HCl-Fe@MWCNTs and c) t-Fe@MWCNTs.

By means of ^{57}Fe Mössbauer, the presence of the three different phases of Fe, α-Fe, γ-Fe and Fe-carbide, was further confirmed. The spectra are reported in figure 3.5. The respective amounts of each Fe phase in the three samples are reported in Table 3.1 and, in agreement with XRD it can be observed that after the treatment in HCl, the α-Fe amount decreased.

	α- Fe%	γ-Fe%	Fe carbide%
Fe@MWCNTs	25	33	42
HCl@Fe@MWCNTs	18	40	42

Table 3.1: Percentage of the Fe phases revealed by^{57}Fe Mössbauer for the samples Fe@MWCNTs and HCl-Fe@MWCNTs.

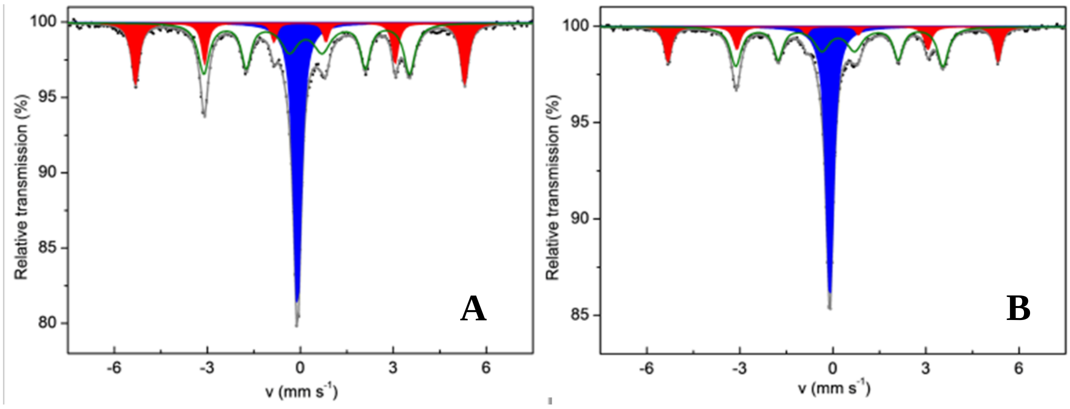

Figure 3.5: ^{57}Fe Mçssbauer spectra of a) Fe@MWCNTs and b) HCl-Fe@MWCNTs with the expected sextets of a-Fe (red) and Fe carbide (green) and the expected singlet of g-Fe (blue). The grey line is the non-deconvoluted experimental profile.

Using TEM analysis, information about the material morphology were obtained for each sample. As it is clear by the TEM images (fig 3.6), the samples consisted of MWCNTs of various diameters and lengths, in which Fe is encapsulated. Fe is located either in the tip region of the nanotubes, with a sphere-like shape (more frequent observing the TEM image) than in the middle region of the carbon nanotubes as nanorods-like shape. After the washing with HCl, considerably less amounts of exohedral Fe were observed at TEM.

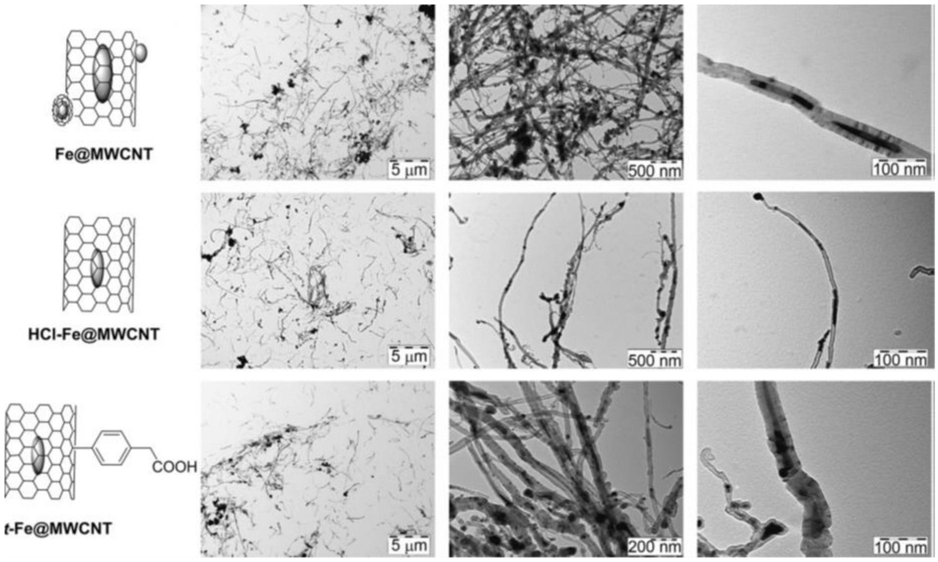

Figure 3.6. TEM images of Fe@MWCNT, HCl-Fe@MWCNTs and t-Fe@MWCNTs.

3.2.1.3 Electrochemical characterization

The electrochemical behavior of t-Fe@MWCNTs was investigated by cyclic voltammetry (CV) experiments using a t-Fe@MWCNTs modified glassy carbon electrode (t-Fe@MWCNTs-GCE) as working electrode. The electrochemical response was studied in the potential range between +1.25V (vs RHE) and -0.75 V (vs RHE) in N_2-saturated 0.10 M phosphate buffer solution (pH 7.4) at a scan rate of 0.03 V s^{-1}. The electrochemical responses of bare GCE, MWCNTs-GCE, HCl-Fe@MWCNTs-GCE were screened in the same potential window and conditions, to compare their CV signals with t-Fe@MWCNTs-GCE, and to recognize the contribute of each material constituents; the comparison is reported in figure 3.7.

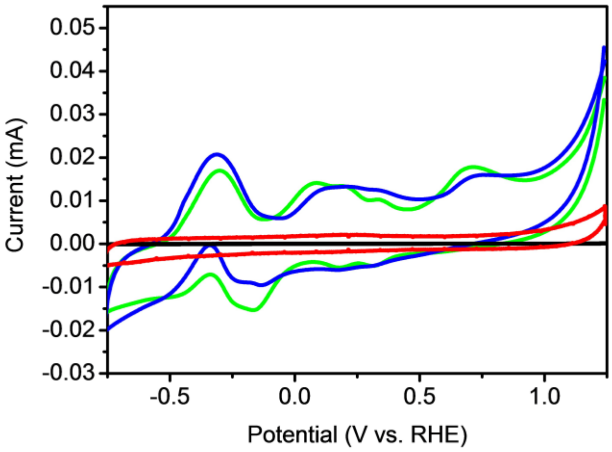

Figura 3.7. CVs obtained on bare GCE (–), GCE/MWCNT (–), GCE/Fe@MWCNT (–) and GCE/t-Fe@MWNCT (–) in N_2-saturated 0.10M phosphate buffer solution (pH 7.40). Scan rate: 0.03 Vs^{-1}.

The bare GCE CV exhibited only capacitive current (i_{cap}) in the investigated potential range. The capacitive current is the current necessary to charge and discharge the electrical double layer at the interface between electrode/electrolyte. CV of MWCNTs-GCE electrode showed an increase in i_{cap} correlated to the deposition of a modified layer onto the GCE surface. The i_{cap} further increased using HCl-Fe@MWCNTs-GCE, due to variability of charge or defects density onto the modified electrode. (19)

HCl-Fe@MWCNTs-GCE showed a broad reduction peak centered at -0.14V vs RHE and three oxidation peaks at 0.30V, 0.13V, 0.71V vs RHE. These signals were also present in the CV collected for the t-Fe@MWCNTs-GCE, hence, they can be attributed to redox processes occurring at the iron phase in the nanotubes. No new signals appeared in the CV of t-Fe@MWCNTs, meaning that the organic functionalization onto the outer wall of the nanotube component did not affect the redox behavior of the iron phase.

In order to confirm if the observed redox peaks in t-Fe@MWCNTs were related to the presence of encapsulated Fe, $FeSO_4$, as Fe reference material,was added to the electrolyte, and a CV experiment was performed. Figure 3.8 shows the CVs obtained on t-Fe@MWCNTs-GCE in absence (black line) and presence (red line) of $FeSO_4$ in solution. After the addition of the Fe salt, the cathodic current increased, indicating that the redox activity observed at -0.4 V was due to the surface confined Fe. In particular, it is possible to hypothesize that the peak at -0.4V is relative to the reduction of Fe(III) to Fe(II), originated during the oxidative sweep.

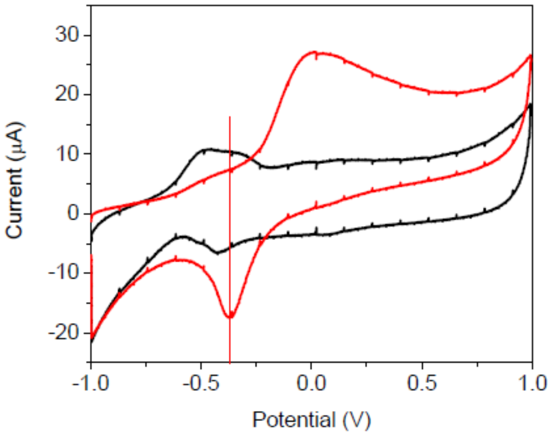

Figure 3.8: CVs of t- Fe@MWCNTs-GCE electrodes in phosphate buffer solution in absence (—) and presence (—) of $FeSO_4$ in solution.

To investigate the stability of t-Fe@MWCNTs, several consecutive CVs were performed in 0.1M phosphate buffer solution pH 7.4 at 0.03 V s^{-1}. Figure 3.9 A shows the collected CVs, while Fig 3.9 B displays the analysis of the anodic peak current at 0.13V.

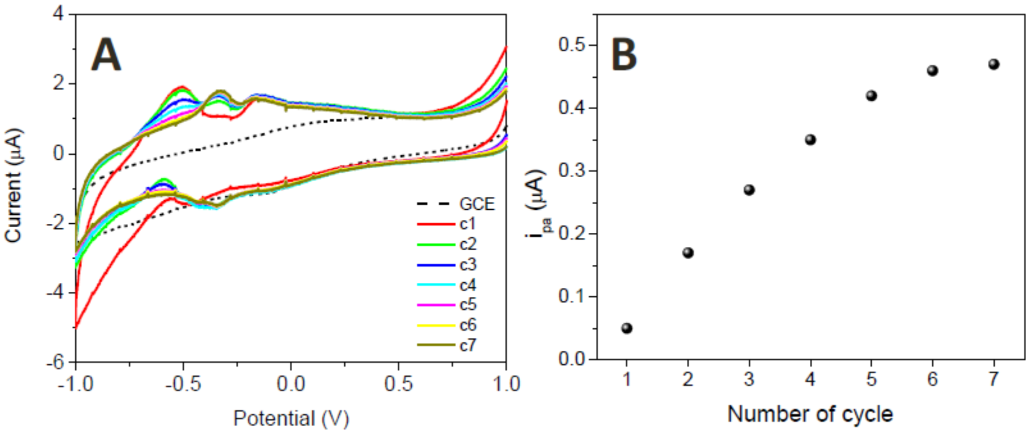

Figure 3.9: A) Cyclic voltammograms of successive cycles measured on GCE/Fe@MWCNTs in 0.10 M phosphate buffer solution pH 7.40. **B)** Analysis of the anodic peak current in function of the number of cycles.

The oxidation peak shifted to less negative potential as the number of cycle increased. From the 6th cycle, both position and intensity of the anodic and cathodic peaks remained constant indicating that it reached a stable situation where the processes of reduction and oxidation occurred unchanged in each further cycle.

3.2.1.4 ORR investigations

The catalytic activity of t-Fe@MWCNTs towards ORR was first investigated by CV in O_2-saturated 0.1M phosphate buffer solution (pH 7.4) at 0.1 V s^{-1}. The comparison between t-Fe@MWCNTs-GCE, HCl-Fe@MWCNTs-GCE, MWCNTs-GCE and bare GCE is reported in figure 3.10. O_2 activation occurred with higher current and at the lowest cathodic potential when GCE was modified with the hybrid t-Fe@MWCNTs. In table 3.2, the values of the peak potential and the relative current are reported.

	E peak (V)	i peak(mA)
GCE	0.45	0.19
MWCNTs/GCE	0.35	0.22
HCl-Fe@MWCNTs/GCE	0.45	0.51
t-Fe@MWCNTs/GCE	0.25	0.99

Table 3.2: The values of the peak potential and relative currents are reported for each sample. The potential values are referred to RHE reference electrode.

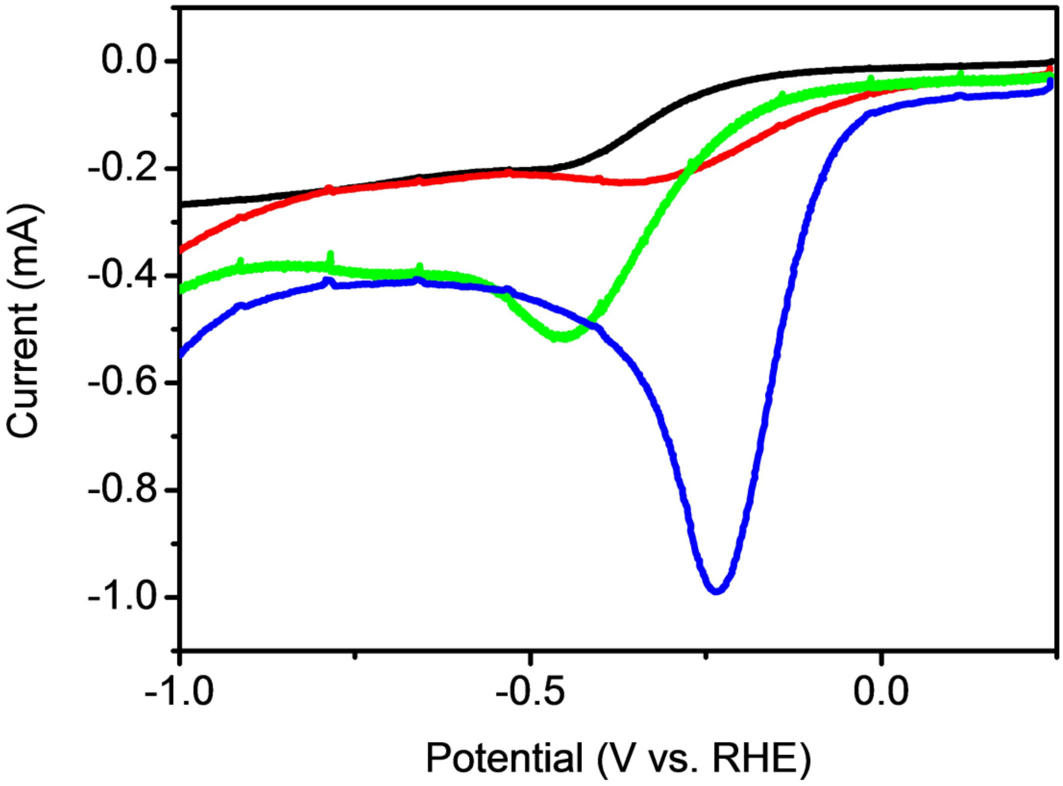

Figure 3.9: Forward CV segment at bare (–), MWCNT- (–), HCl-Fe@MWCNT- (–) and t-Fe@MWCNT-modified GCE (–) in 2.5 mgL^{-1} O_2 dissolved in phosphate buffer solution. Scan rate: 0.10 Vs^{-1}.

These findings suggested that Fe-encapsulated into the inner cavity of MWCNTs was available to the O_2, and played a crucial role for the occurrence of the reaction. Using HCl-Fe@MWCNTs-GCE, a rise in i_{peak} was observed. The shift of the peak potential to less negative potential, and the current increase using t-Fe@MWCNTs suggested a non-innocent role of the organic moieties, which have been introduced by the radical addition procedure. These results were in agreement with the results reported by Deng et al., who studied a similar system based on iron nanoparticles confined inside pea-pod-like CNTs exhibiting high activity and selectivity as ORR catalyst in polymer electrolyte membrane fuel cells (PEMFC). The high activity was attributed to the decrease of the local work function on the carbon nanotubes surface, due to electron transfer processes from the inner Fe-encapsulated to the graphitic shells. (12)

Thus, based on the present results and on previously reported examples, the enhancement of the ORR electrocatalytic activity of t-Fe@MWCNTs could be explained as follows:

1) The exohedral functionalization of the outer nanotubes wall resulted in the formation of defects, that enhanced the absorption of O_2 onto the nanotubes, increasing the substrate concentration in the vicinity of the Fe catalytic phase;
2) The presence of cross-linking defects allowed better electronic communication between the internal Fe and the outer graphitic shells, making possible electron transfers through the CNTs walls.

In order to validate these two hypotheses, more in depth analysis of ORR activity were performed by measuring: a) CVs in presence of increasing O_2 concentrations, obtaining information on the affinity of the different materials towards the O_2, and b) electrochemical impedance experiments, gaining information on the charge-transfer resistance for each material.

When the CVs in presence of increasing O_2 concentration were measured (figure 3.10 A), a linear correlation between the peak currents and the O_2 concentration was obtained in the range between 0 and 2.5 mg $L^{-1.}$ Based on the obtained calibration curve (figure 3.10 B), the sensitivities towards O_2 were determined for each material, calculated as the slope of the calibration curve. Table 3.3 reports sensitivity, limit of detection (LOD),associated to the lowest amount of oxygen detectable, and linear range for each material. The LOD associated to HCl-Fe@MWCNTs and t-Fe@MWCNTs were the lowest. When t-Fe@MWCNTs-GCE was used, the corresponding linear range, the range in which the current increased linearly increasing the amount of oxygen, was the widest: 0.1-3.1 mg L^{-1}. These findings supported our first hypothesis, claiming that the exohedral functionalization favored the O_2 absorption, aided by the introduction of additional defects.

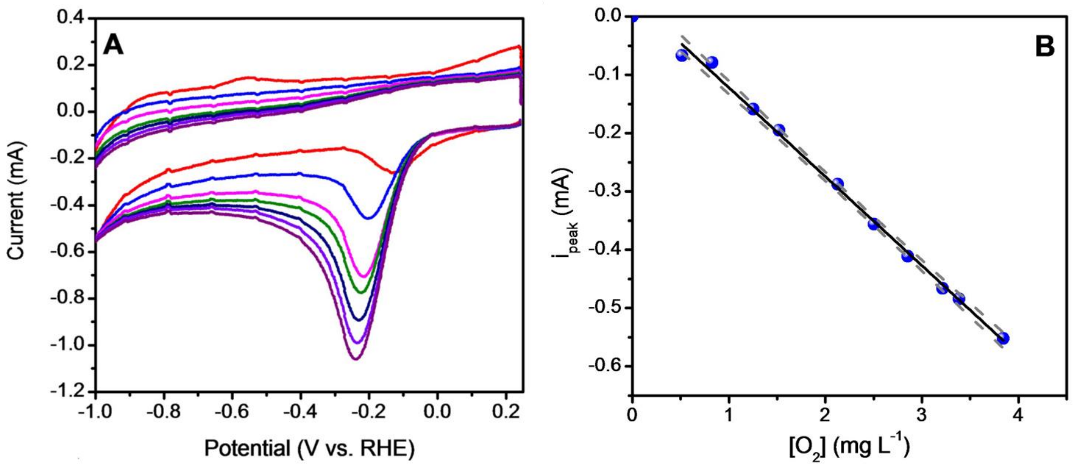

Figure 3.11: A) CVs at t-Fe@MWCNT-modified GCE in phosphate-buffer solution with increasing amounts of dissolved O_2. Scan rate: 0.10 Vs¢1. B) Calibration curve obtained from the results in A). Experimental points (●), best linear fit (solid line) and 99% confidence bands (dashed line).

	LOD (mg L^{-1})	Linear Range (mg L^{-1})	Sensitivity (10^2 µA L $mg^{-1}cm^{-2}$)
GCE	1.02	3.0-4.1	0.11
MWCNTs	0.6	0.2-4.0	3
HCl-Fe@MWCNTs	0.6	0.09-2.5	4.6
t-Fe@MWCNTs	0.3	0.1-3.1	8.1

Table 3.3. The values of LOD (mg L^{-1}), Linear range (mg L^{-1}) and sensitivity (µA L mg^{-1} cm^{-2}) are reported for each sample.

Electrochemical impedance spectroscopy (EIS) analysis was performed for each material, studying the response in $K_3[Fe(CN)_6]/K_4[Fe(CN)_6]$ solution as redox probe, and under ORR conditions. EIS experiments were performed in the frequency range between 10^5 to 10^{-2} Hz, with a potential perturbation of 0.01V and a working potential of -0.20 V. By the Nyquist spectra analysis, Randles and R(RC) circuits were found as the best equivalent circuits for the investigated electrochemical systems. the schematic representation of the equivalent circuits are reported are represented in figure 3.12.

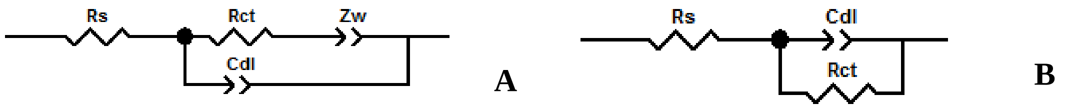

Figure 3.12: representation of A) Randles circuit and B) R(RC) circuit.

The circuit elements are: C_{dl}, corresponding to the double-layer capacitance, R_{ct} corresponding to the charge-transfer resistance, Z_W representing the impedance due to mass transfer of the redox species to the electrode described by Warburg, and R_S is the solution resistance.

By the Nyquist plots in figure 3.13 emerged that the charge transfer resistance decreased after the exohedral functionalization, meaning that the electron transfer was favored. These results are in very good agreement with all the other results, and supported the second hypothesis claiming that the electronic communication was enhanced by cross-linking defects created after the exohedral functionalization.

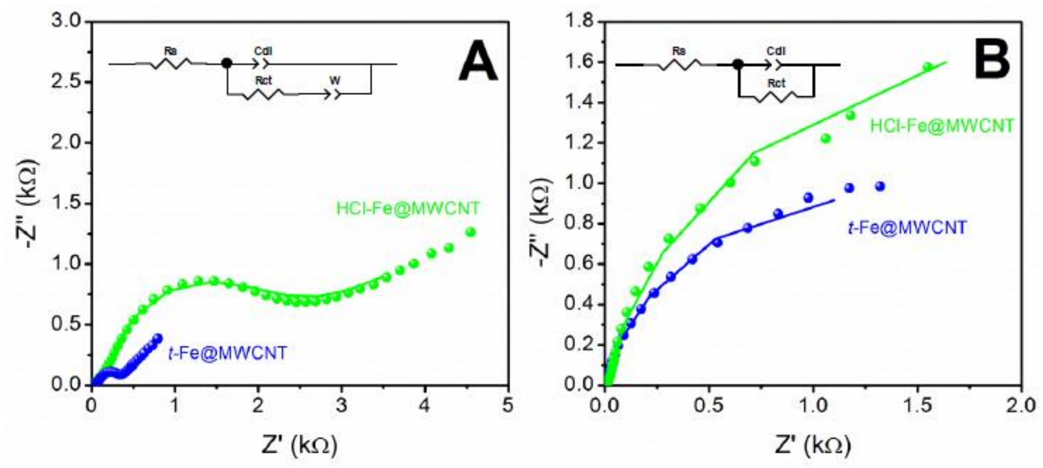

Figure 3.13: Nyquist plot obtained at GCE/HCl-Fe@MWCNT (●) and GCE/t-Fe@MWCNT (●). Dots are experimental points and the lines the fit obtained with the corresponding circuit (inset). Experimental conditions: **A)** 20 mM K3$[Fe(CN)_6]/K_4[Fe(CN)_6]$ equimolar solution prepared in phosphate buffer solution pH 7.40. **B)** ORR conditions in phosphate buffer solution pH 7.40.

The main variations in the fitting values were observed for R_{ct}. In $[Fe(CN)_6]^{3/4-}$ solution, the R_{ct} determined at HCl-Fe@MWCNT (1.3 ± 0.1) kΩ is bigger than that of *t*-Fe@MWCNTs (0.23 ± 0.06) kΩ. Under ORR conditions, the R_{ct} also decreased from (4.1± 0.3) kΩ to (3.1 ± 0.2) kΩ by adding the carboxylic functionalization on Fe@MWCNTs. This behavior was related to a favored discharge of the redox species on the electrode surface. These results were consistent with the lower potential necessary for the ORR reaction using t-Fe@MWCNTs. The increase in the density of the states near the Fermi level after the functionalization leads to a decrease in the local work function on the walls of the nanotubes and an increase in the electrochemical activity. (20)

An important parameter to characterize an ORR electrocatalyst is its selectivity. As already mentioned above, the O_2 reduction in most cases leads to two different products: H_2O_2 as 2-electrons reduction product and H_2O as 4-electrons reduction products. In order to recognize the reduction product, rotating disk electrode (RDE) experiments were carried out. Linear sweep voltammetry (LSV) curves were collected using a RDE modified by t-Fe@MWCNTs and HCl-Fe@MWCNTs changing the rotation speed (ω) of the RDE. The current density values reported in figure 3.14 A have been calculated normalizing by the geometric area of the RDE.

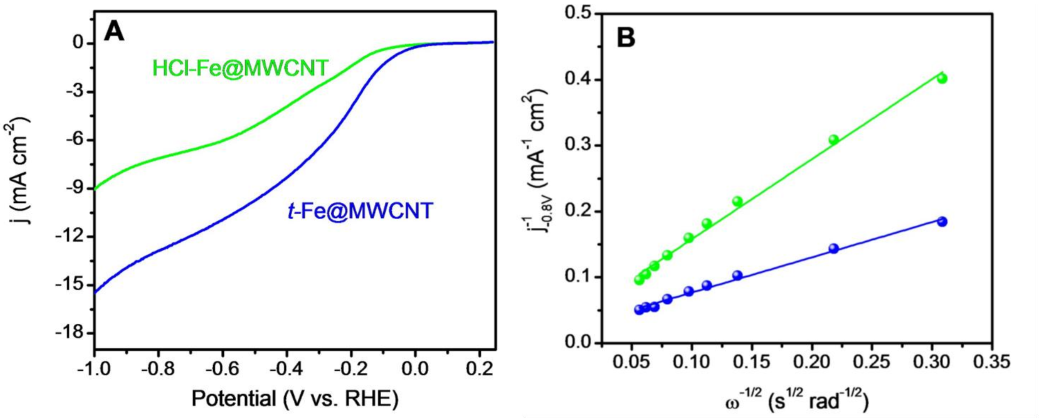

Figura 3.14: A) LSV curves of HCl-Fe@MWCNT (–) and t-Fe@MWCNT (–) modified GCE in O_2-saturated 0.10m phosphate buffer solution (pH 7.40) at 1500 rpm. Scan rate: 0.005 Vs^{-1}. B) Corresponding K–L plots at -0.8 V versus RHE. The dots represent the experimental points and the lines the best linear fits.

Plotting the inverse of the current density j^{-1} at -0.8V vs RHE, which is the potential where the current reaches the plateau and the process is mass transport limited, in function of $\omega^{-1/2}$ the Koutechy-Levich (K-L) plots were obtained; they are reported in figure 3.14 B. The K-L plots can provide informations on the number of electrons involved in the redox process and the reaction order respect to O_2. A linear dependence between j^{-1} and $\omega^{-1/2}$ were obtained, implying a first order reaction towards the O_2 dissolved in solution. (21) Using equations reported below the number of electrons can be calculated.

$$1/j_D=1/j_k + 1/ B\omega^{1/2} \qquad (1)$$

$$B=0.2\ n\ FAv^{-1/6} C_{O2} D_0^{-2/3} \qquad (2)$$

Equation (1) is known as K-L equation for RDE, where j_D is the diffusion limited current density, jk is the heterogeneous rate constant limited density current, ω is the RDE rotation speed in rad/s and B is the proportional coefficient between j_D and ω. The slope of the fitting line corresponds to 1/B. Using equation (2), n, the number of electrons involved in the reduction, can be calculated. The others parameters in equation (2) are: A, the geometric area of the RDE (0.0752 cm^2); v, which is the kinematic viscosity in cm^2 s^{-1} (0.01 cm^2 s^{-1}) ; C_{O2} which is the O_2 concentration in the bulk solution (0.26 $x10^{-3}$ M)

in mol cm^{-3} and D, which is the diffusion coefficient of O_2 in cm^2 s^{-1} (2x10^{-5} cm^2 s^{-1}). The value of n was 2 for HCl-Fe@MWCNTs and 4 for t-Fe@MWCNTs. The different selectivity can be correlated to the presence of exohedral functionalization. These results agreed with the work of Tse et al., the organic functionalization created a less hydrophobic environment around the t-Fe@MWCNTs, this local hydrophilicity change could affect the rate of proton transfer to the O_2-, slowing it. Hence, the resulting rate of proton transfer became comparable to the rate of O-O bond breaking, thus favoring the yield in H_2O production instead of H_2O_2. (22)
A deeper investigation of the LSV curves obtained in O_2 saturated phosphate buffer 0.1M (pH7.4) was conducted. When working in the potential range between 0.25V to -1V vs RHE at 0.005 V s^{-1} and rotation rates from 100 to 3000 rpm, further insights on the kinetics of the ORR catalysis by t-Fe@MWCNTs were achieved. A K-L behavior is observed, the limiting current increased linearly increasing the square root of the rotation speed. Extrapolating the K-L lines, non-zero intercepts were obtained, indicating that the process was under mixed kinetic-diffusion control. (21)

3.2.1.5 Conclusion

Looking for highly sustainable technology for the activation of ORR avoiding Pt-based catalyst, a novel functional nano-catalyst based on earth abundant metal such as Fe has been designed. Opportunely interfacing MWCNTs and Fe through encapsulation of the metal within the inner nanotubes cavity, we achieved a novel system where the carbon nanostructure phase protected the encapsulated-Fe without affecting its availability for the electrocatalysis. By further functionalizing the outer CNT sidewalls, we achieved important boosts of performance in the ORR at near neutral pH with E_{onset}: 0.02V vs RHE and a sensitivity 8.9x10^{2}μA L mg^{-1} cm^2. The addition of benzylic acid moieties enhanced hydrophilicity of the material and density of defects onto the carbon nanostructure, positively affecting the reduction of the O_2. The affinitity of t-Fe@MWCNTs for the O_2 absorption was improved as the sensitivity and the LOD value indicates; cross-linking defects enhanced the electronic communication and favored the electron transfer processes in agreement with impedance experiments; the proton transfer rate was decelerated leading to an increase of selectivity towards the H_2O production by t-Fe@MWCNTs catalyst, in contrast with a more selective H_2O_2 formation when the less hydrophilic HCl-Fe@MWCNTs was used.

3.3 N-doped graphitized carbon nanohorns (g-N-CHNs) as novel electrocatalyst for the selective production of H_2O_2 from O_2 reduction

As already mentioned, hydrogen peroxide (H_2O_2) is an essential chemical. Its annual production is very large and figures around the 4 x 10^6 tons. It is used in many industrial sectors, due to its benign oxidant properties, as well as being a bleaching and sanitizing agent. The main applications are in pulp and paper production, manufacture of sodium perborate and sodium percarbonate as detergent bleaches, textile bleaching (cotton fabric and wool) and chemical water treatment to make the water drinkable. In the last decades, H_2O_2 has been also considered a sustainable energy carrier to feed new generations of fuel cells. (23) Despite its wide use, the currently adopted H_2O_2 industrial production method still suffers from a low sustainability, based on the anthraquinone process, a multistep sequence where the precursor undergoes first hydrogenation on Pd, and after an oxidation step. In the final step, H_2O_2 is extracted by the reaction medium. (24) In order to find a greener method, other approaches for the H_2O_2 synthesis have been proposed up to now, such as the direct production by H_2/O_2 electrolysis onto Pd/C and the plasma assisted or metal catalyzed H_2/O_2 reactions. (25) (26) However, these approaches are rather dangerous and restrictive, as the H_2 and O_2 gases have to be kept outside the explosive regime. In this context, the two electron electroreduction of O_2 to the selective production of H_2O_2 comes across as a very appealing alternative process. In order to be industrially competitive, the reaction requires an adequate catalyst operating at low overpotentials and with high selectivity. A further desirable feature is the ability to perform the process in a wide range of pH, given the various application fields. For instance, solutions of H_2O_2 in NaOH are used for the pulp bleaching while H_2O_2 in H_2SO_4 finds application as oxidant agent. Moreover, the possibility of performing the reduction by the same catalyst in a wide pH range would be very desirable in view of alkaline and hybrid metal-air batteries (27) (28) or acid fuel cells. Up to now, benchmark catalysts for ORR are based on precious metals. H_2O_2 production can be driven by Au and Pd based alloys with high faradaic efficiency (FE%) in acidic medium, pH 1, but at rather negative potential (-0.5V vs SCE (-0.2V vs RHE)). (29) Another example is the Pt-Hg nano-alloy which drives the process at 0.1-0.3V vs RHE with 70 FE% in 1 hour. (30) Table 3.4 encloses most recent state of the art electrocatalysts reported in literature, including two of the most interesting examples of metal free porous carbon based catalysts.

Catalyst	**Ref.**	**medium**	**Working potential**	**FE% of H_2O_2**
Pd-Hg/C	(6)	0.1M $HClO_4$	0.35-0.75V vs RHE	95
Mesoporous N-doped carbon [a]	(31)	0.1M HClO4	0.1 vs RHE	65.15
Hierarchical porous carbon [b]	(32)	pH1-7	-0.5V vs SCE	81.8-70.8
Pd-Au	(29)	pH1	0.1-0.3 V vs RHE	92.5
Pt-Hg	(30)	pH1	0.1-0.3 V vs RHE	70.8
C@Pt	(33)	1M HClO4	0.1V vs RHE	41

Table 3.4: Summarizing table reporting the most promising catalyst applied for the selective reduction of O_2 to H_2O_2.

In the above investigations, the ORR was generally studied in acidic environment, and only in one of them neutral pH conditions were applied with some success. In such case, the specific catalyst, proposed by Liu et al., was based on porous N-doped carbon materials. However, the synthesis, consisting in the use of a Zn-modified metalorganic framework (MOF) graphitized at 900 °C, was not trivial, which strongly limits the opportunity for a real industrial scale up. (32) The material herein includes single walled carbon nanohorns (SWCNHs) modified by a N-doped-graphitic layer achieved via a fast and easy synthesis, preferable from an industrial point of view.

3.3.1 Result and discussion

3.3.1.1 Synthesis

g-N-CNHs was synthesized using the reaction scheme reported below (on the top of figure 3.15)

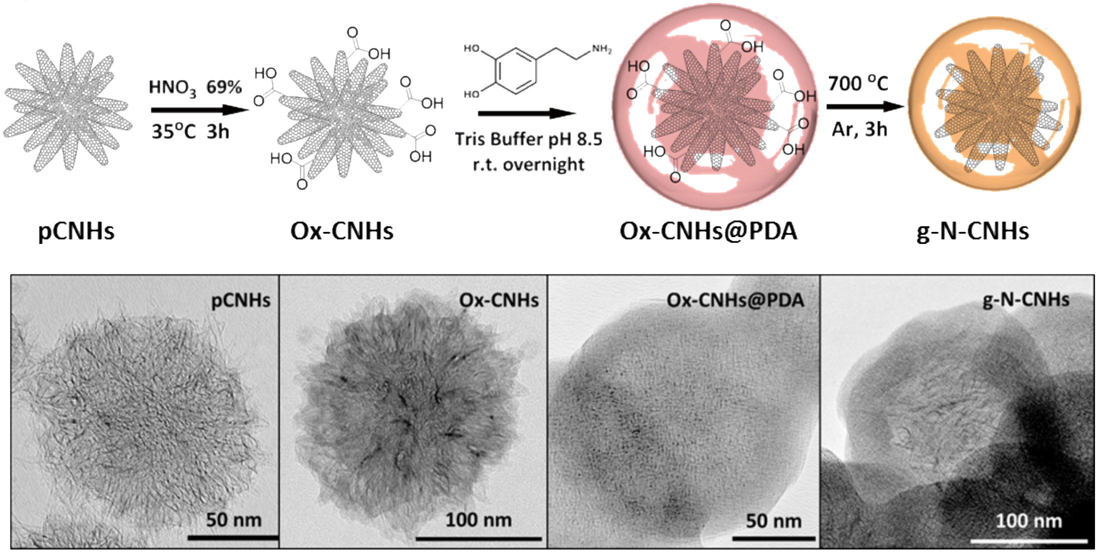

Figure 3.15: Top: Scheme of the synthetic protocol to obtain g-N-CNHs. Bottom: TEM images relative to each material at each stage of the synthesis.

Pristine CNHs were first oxidized by HNO_3 4M, yielding ox-CNHs. The mild oxidation treatment opened the conical tips and increased the available surface and at the same time introduced oxygenic groups such as COOH, OH, epoxydes or carbonyl, without damaging to a large extent the polyaromatic scaffold, thus preserving good electronic properties of the SWCNHs. In particular, the COOH groups played an essential role for the anchoring of the poly-dopamine, the N-doped graphite layer precursor, around the carbon nanostructure. Hence, ox-CNHs were combined with dopamine hydrochloride, which polymerized directly onto the carbon nanostructure creating a shell of polymer. The as obtained material, ox-CNHs/PDA, underwent a thermal treatment under an argon flow, at 700°C, which allowed graphitization of the PDA layer with simultaneous preservation of the CNHs structure. The temperature was chosen as the minimum necessary temperature to graphitize the PDA layer restoring the conductivity. Lower temperatures did not cause graphitization of the PDA layer, resulting in an insulated material.

3.3.1.2 Macroscopic and microscopic characterization

Each reaction step was characterized by morphologic analysis using TEM. (figure 3.15).
After the oxidation step, the TEM images did not exhibit important changes in the carbon nanostructure morphology, while, after the coating with the PDA layer, change in morphology appeared clear, the sea-urchin like shape was blurred and a sphere-like structure appeared, confirming the polymer coating.
Graphitization of the PDA polymer became evident in the final material where a thick shell was observed by TEM, which embedded uniformly the carbon nanostructure, still

well visible at the core. A statistical analysis of the composite material showed that the average diameter of ox-CNHs@PDA particle decreased from 100 nm to 50 nm after the annealing. Further morphological and compositional insights were gained through energy dispersive X-ray spectroscopy (EDX) analysis, which confirmed the presence and colocation of the C, N, O atoms. (figure 3.16).

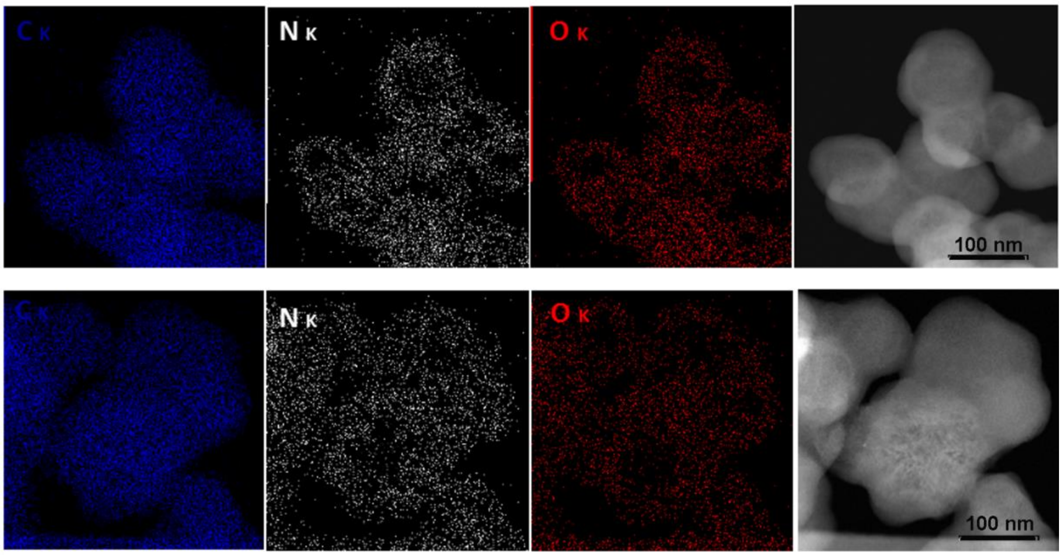

Figure 3.16. EDX mapping of the three elements C, N, O and HAADF-STEM of Ox-CNHs@PDA (Top) and g-N-CNHs (Bottom).

Thermogravimetric analysis (TGA) provided important information on the material thermal stability. TGA curves were performed under N_2 and under air flow (figure 3.17). By TGA analysis under N_2 flow a weight loss of 7% has been evaluated for ox-CNHs, due to the removal of the oxygenic groups. TGA did not allow the quantification of PDA amount because the polymeric layer was not fully decomposed within the temperature range studied. TGA under air flow showed that the graphitized material g-N-CNHs decomposed at lower temperature (400°C) than ox-CNHs and ox-CNHs@PDA. The weight loss step for g-N-CNHs appeared sharper than for ox-CNHs@PDA, indicating that g-N-CNHs was more homogeneous than its fresh precursor, ox-CNHs@PDA. Under air flow none of the TGA profiles showed residual weight, indicating that no metals were present, emphasizing the high purity of the employed carbon nanostructure. This crucial aspect was later confirmed by X-ray photoelectron spectroscopy (XPS) and inductively coupled plasma optical emission spectrometry (ICP-OES) analysis.

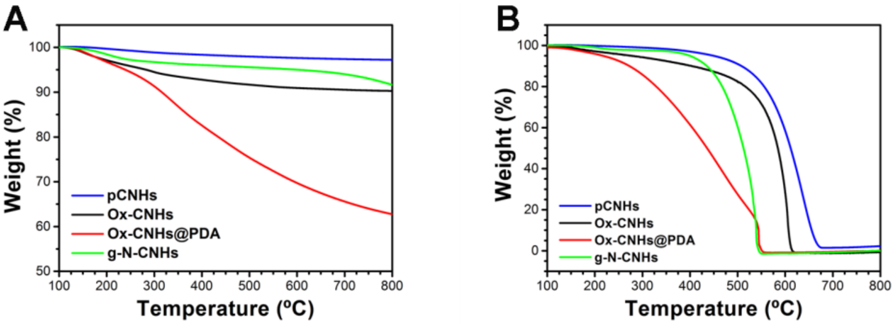

Figure 3.17. A) TGA curves performed under N_2 flow; B) TGA curves performed under air flow.

The N-doping can introduce different types of N-based moieties as shown in figure 3.18 below. Mainly, the N-species generally observed are: a) graphitic N located inside the graphitic plane, b) pyrrolic N and c) pyridinic N which are placed at the edge of the graphitic plane. Pyrrolic N atom is part of pentagon moiety defects across the sp2-conjugated framework; graphitic N and pyridinic N are part of six membered rings, with the difference that graphitic N forms three N-C bonds. N-O species have also been recognized and reported in literature. (34)

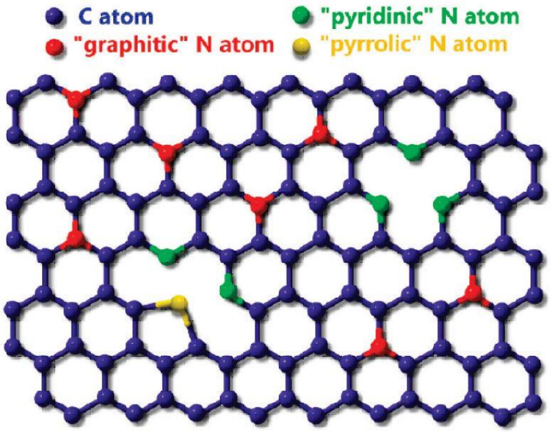

Figure 3.18: Schematic diagram of the three types of doped N atoms in N-graphene (Reprinted with permission from D. Wei, Y. Liu, Y. Wang, H. Zhang, L. Huang, G. Yu, Nano Lett., 2009, 9, 1752-1758. Copyright 2017 American Chemical Society)

XPS analysis was carried out on the materials at all the stages of the synthetic procedure (figure 3.19) p-CNHs XPS spectra showed only peaks ascribed to the C=C aromatic pattern in the C_{1s} binding energy (BE) range. The oxidation treatment introduced oxygen-containing groups, peaks in the O_{1s} BE range confirmed the right course of this step. After the PDA covering, a new peak in the N_{1s} BE range (400.0eV) appeared due to the amine functionalities of the PDA polymeric layer, and attributed to a N-C bond type. Interestingly, in agreement with the theoretical N/O ratio of the dopamine molecule, we find a N:O = 1:2 ratio in the ox-CNHs@PDA material (after subtracting the 5.49% contribution for the O atoms due to the first oxidation step).

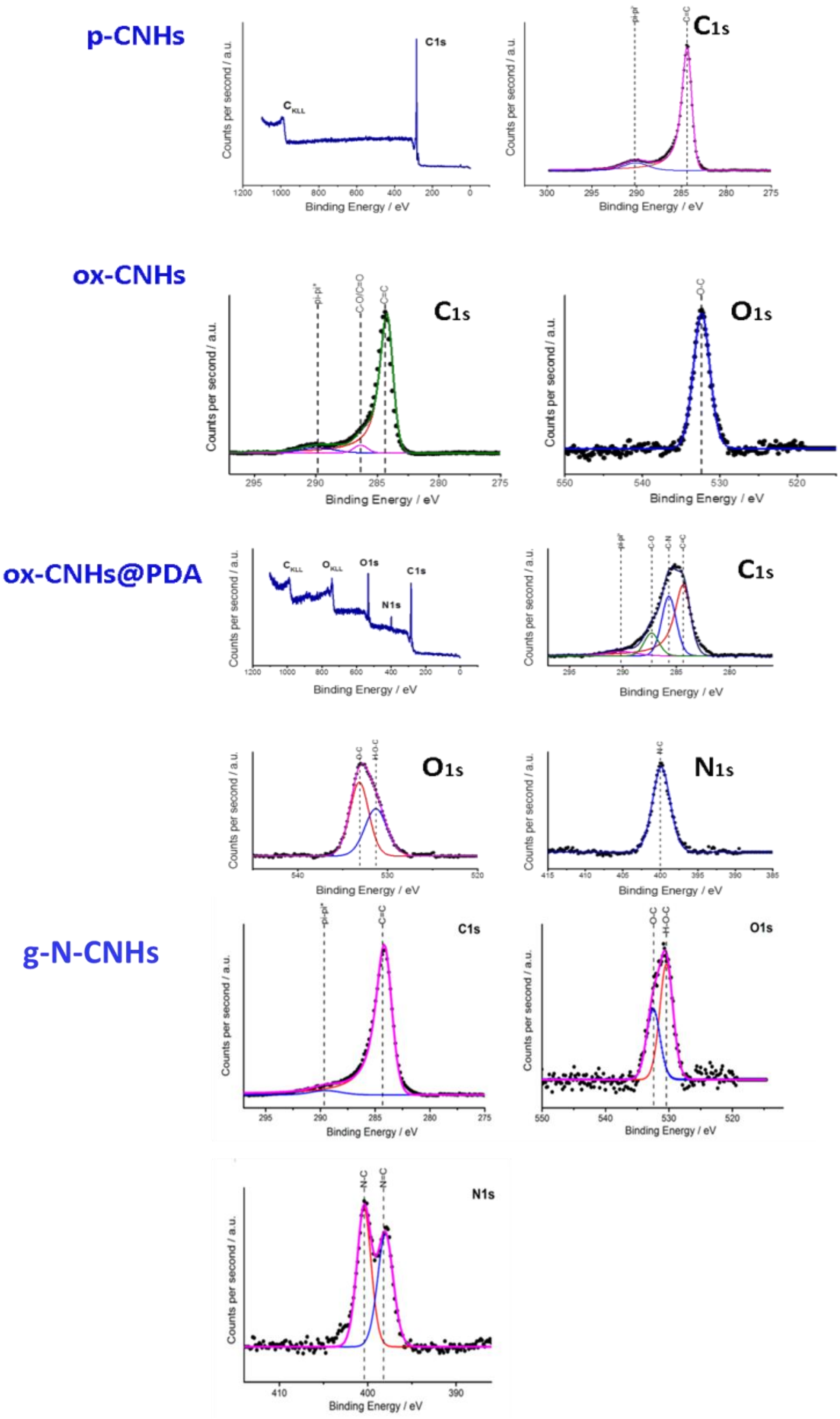

Figure 3.19. XPS analysis of **g-N-CNHs and its precursor nanomaterials** in the C_{1s}, O_{1s} and N_{1s} BE ranges.

Sample	Core	Atomic %
p-CNHs	C_{1s}	99.10
	O_{1s}	0.90
	N_{1s}	-
Ox-CNHs	C_{1s}	94.51
	O_{1s}	5.49
	N_{1s}	-
Ox-CNHs@PDA	C_{1s}	73.08
	O_{1s}	19.45
	N_{1s}	7.47
g-N-CNHs	C_{1s}	90.63
	O_{1s}	3.80
	N_{1s}	5.56

Table 3.5 Atomic % of the three constituent atoms for the four materials as calculated by XPS analysis.

As expected, the XPS spectra resulted deeply changed after the annealing treatment. In the first instance, the N/O relative amounts was changed, following the total removal of the ox-CNHs functional groups. Hence, only O and N doping atoms of the graphitic shell are left in the material. In agreement with literature, the annealing also decreased the total N and O percentages. (35) (36) A more refined analysis of the N peaks of g-N-CNHs displayed the existence of two peaks in the N_{1s} BE range, the first at 400.3 eV, assigned to a N-C bond type, and corresponding to pyrrolic N atoms; the second at 398.9 eV attributed to a N=C consistent with pyridinic N atoms. (37) Importantly, no graphitic N peak was present, indicating that the thermal treatment resulted only in formation of pyrrolic and pyridinic N atoms. It is also worth noting that no peaks relative to metals were found in the whole range of BEs. The absence of metal was unequivocally confirmed by ICP-OES analysis on the g-N-CNHs sample.

Raman spectra collected for each material showed the characteristic peaks of the nano-carbon component CNHs: the distinctive D and G bands respectively at 1350cm^{-1} and 1558cm^{-1} and the 2D band at 2700 cm^{-1}. The I_D/I_G ratio can be used as a semi-quantitative data to confirm the SWCNH functionalization. (38) The I_D/I_G ratio slightly increased after the oxidation treatment, confirming the occurrence of covalent functionalization and the introduction of defects onto the π-extended framework. However, as the increase was not dramatic, we could assume that oxidation only caused a limited perturbation of the aromatic framework, thus not compromising the electronic properties of CNHs to large extent. The D, G and 2D peaks became broader upon the PDA covering, while the graphitization treatment restored the sharpness present for the p-CNHs and ox-SWCNHs materials, indicating a crystallization of the carbon shell (Figure 3.20).

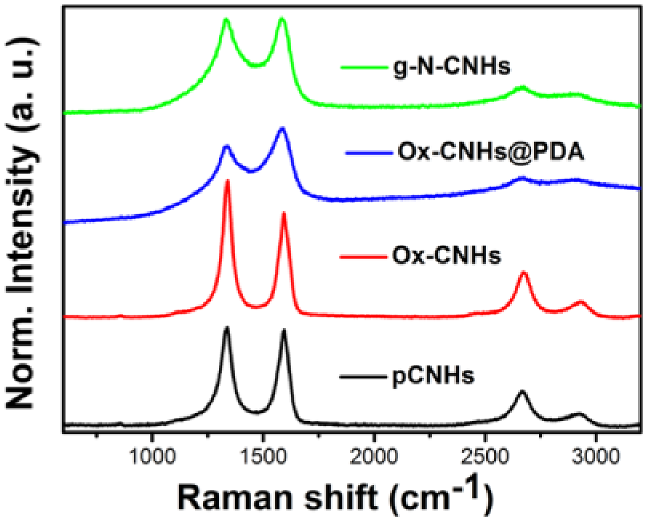

Figure 3.20. Raman spectra performed for the obtained materials at each synthetic steps.

Analysis of the textural properties of the final material g-N-CNHs by N_2 physisorption at the liquid nitrogen temperature revealed a high Langmuir surface area of 481 m^2/g. The material presented a considerable microporosity, with a type I isotherm according to IUPAC recommendations. (39)

As reported in figure 3.21 B, the isotherm did not present hysteresis and had a microporous volume accounting to 0.15 cm^3/g. The external surface area calculated from the t-plot was very low (26 m^2/g) and therefore the greatest contribution to the total surface area came from the microporous surface area (455 m^2/g), as calculated from the difference between the total surface area and the external surface area. In comparison, N_2 physisorption analysis of the ox-CNHs (Figure 3.21 A) indicates an extensive microporosity, but with a higher Langmuir area (928 m^2/g), as a consequence of the tip opening process caused by the oxidation treatment, which makes available the CNHs internal channels (40) As expected, the graphite coating blocks the CNHs internal space and therefore causes a decrease in surface area. Overall, however, the final material's area remains high enough to guarantee an efficient adsorption of the O_2 molecule.

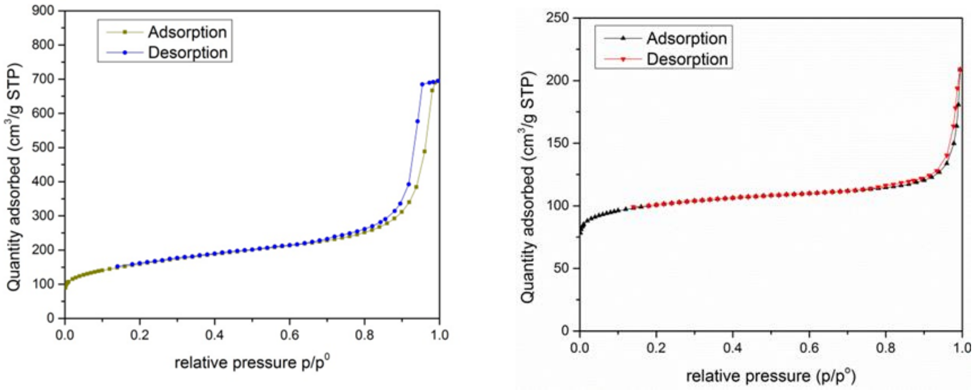

Figure 3.21 N_2 physisorption isotherm of **ox-CNHs** (left) and **g-N-CNHs** (right), measured at Liquid Nitrogen temperature.

3.3.1.3 Electrochemical characterization

The redox behavior of each material has been characterized by electrochemical techniques, in the first instance using cyclic voltammetry (CV). The electrochemical response was studied in the potential range between -0.34 V and 1.65 V vs RHE in N_2-saturated phosphate buffer solution 0.1M pH7.4 using a scan rate of 0.05 V s^{-1}. The limits of the potential range screened correspond respectively to the onset of reduction and oxidation of water.

Figure 3.22 reports a comparison of **ox-SWCNHs, ox-SWCNHs@PDA** and **g-N-CNHs** modified glassy carbon electrode (GCE). The capacitive current of **ox-CNHs@PDA** was lower than either that **ox-CNHs** and **g-N-CNHs**, presumably given that the PDA layer embedding the carbon nanostructure scaffold acted as an electrical insulator, slowing down the charge mobility onto the modified electrode. Upon thermal treatment, the capacitive current increased again. Hence, the PDA layer after the graphitization became a highly conductive N-doped graphitic layer. **ox-CNHs** modified GCE exhibited an oxidation peak involving the oxygen containing groups at 0.82V. The CV trace of **g-N-CNHs** displayed a reversible process centered at $\boldsymbol{E_{1/2}} = \frac{\boldsymbol{E_{p\,an}+E_{p\,cat}}}{\boldsymbol{2}} = \boldsymbol{0.60\,V}$. This reversible process has been attributed to a process involving nitrogen functionalities decorating the graphitic layer.

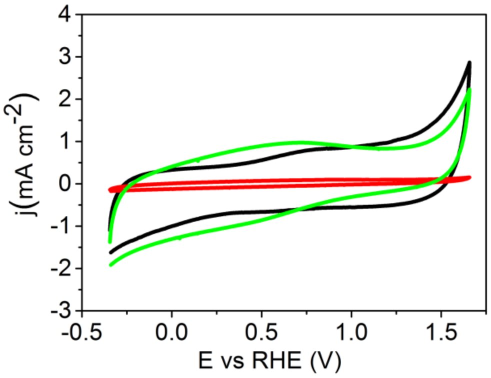

Figure 3.22. CVs obtained on GCE modified with ox-CNHs (▬), Ox-CNHs@PDA (▬) and g-N-CNHs (▬) in 0.10 M phosphate buffer solution pH 7.4 under N_2. Scan rate: 0.05 V s^{-1}.

In order to gain further insights into the redox behavior and the stability of the material, 20 consecutive CVs were carried out for each material (figure 3.23).

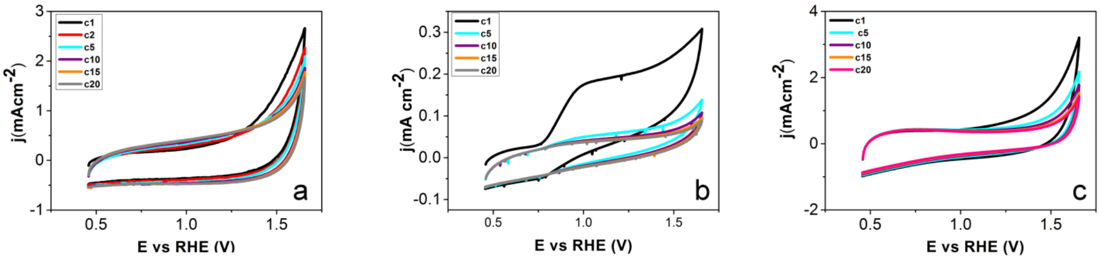

Figure 3.23. Multicycle (up to 20 cycles) CVs obtained on GCE modified with a) Ox-CNHs, b) Ox-CNHs@PDA and c) g-N-CNHs in 0.10 M phosphate buffer solution pH 7.40 under N_2. Scan rate: 0.05 V s^{-1}.

For ox-CNHs and g-N-CNHs, negligible changes characterized the respective CVs profiles by the 2nd to the 20th cycles; the first cycle was different because of the stabilizing processes occurring at the electrode surface. In contrast, ox-CNHs@PDA showed a very different behavior, with a change in the first cycle much more pronounced, and a concomitant CV shape change. In particular, the first cycle was characterized by a broad oxidation peak related to a oxidation process, consistent with oxidation/reduction of dopamine/dopaminequinone relative to the presence of non-covalently adsorbed poly-dopamine domains. (41) (42) This process completely disappeared after the 5th cycle, denoting that all the supramolecular domains reacted and were oxidized and polymerized.

3.3.1.4 Electrocatalytic performance of g-N-CNHs nano-hybrid for selective O_2 reduction to H_2O_2

Preliminary study on the electrocatalytic activity of ox-CNHs, ox-CNHs@PDA and g-N-CNHs, were carried out in the potential range between 1.20 V to -0.35V vs RHE in 0.1M phosphate buffer solution pH 7.4, using a scan rate of 0.05 V s^{-1}. Phosphate buffer solution has been chosen because allowed a wider available potential range. As reported in figure 3.24 ORR occurred on g-N-CNHs nanohybrid at higher current and at lower potential than the precursor materials ox-CNHs and ox-CNHs@PDA. In table 3.6 peak potential and relative currents are reported.

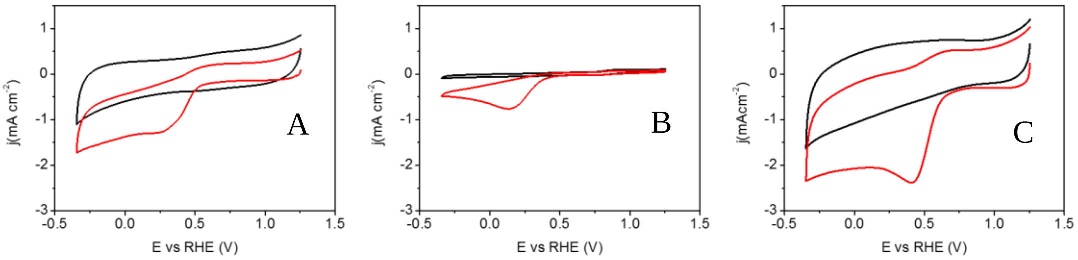

Figure 3.24: Study of ORR in N_2 saturated (–) and O_2 saturated (–) 0.1M phosphate buffer pH 7.4 at A) ox-CNHs, B) ox-CNHs@PDA and C) g-CNHs modified GCE. RE:Ag/AgCl. CE: Pt wire. Scan rate: 0.05V s^{-1}.

	Onset potential (V)	E_p (V)	j_p (mA cm^{-2})
ox-CNHs	0.49	0.25	-1.3
ox-CNHs@PDA	0.41	0.05	-0.025
g-N-CNHs	0.53	0.40	-1.79

Table 3.6 Summarizing table of the onset potential and peak potential and current obtained by CV experiments in O_2 saturated solution using ox-CNHs, ox-CNHs@PDA and g-N-CNHs. The potential values reported in the table are referred to the RHE reference electrode. The current density values are normalized by the electroactive surface area (EASA) obtained using hydroquinone as redox probe. Further normalization by the amount of catalyst is also reported.

A deeper analysis of the electrocatalytic properties of g-N-CNHs towards ORR was then carried out by changing pH conditions. The selective reduction of O_2 to H_2O_2 is highly dependent on the pH values applied and the potential used. (43) It is well known that

H_2O_2 chemical stability decreases increasing the pH and that more cathodic potential can lead to the further reduction of H_2O_2 to H_2O. (44)
The selected pH values are 0.1M H_2SO_4, pH 7.4 in 0.1M PBS and pH 13 in 0.1M NaOH. Comparison of the CV curves of g-N-CNHs at each pH value is shown in Fig 3.25.

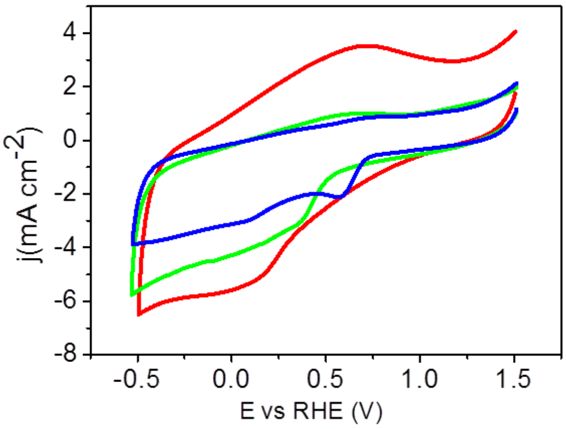

Figure 3.25. CVs obtained on GCE modified with **g-N-CNHs** at pH 1.0 in 0.1 M H_2SO_4 (–), at pH 7.4 in 0.10 M phosphate buffer solution (–) and at pH 13.0 in 0.1 M NaOH (–) under O_2. Scan rate: 0.05 V s^{-1}.

O_2 activation occurred at all pH values explored, each with a specific peak potential (E_p) value and specific current. These findings indicated that the pH profoundly influence the mechanism of the O_2 reduction. In table 3.7 the onset potential values, the Ep and the current normalized either by the electroactive area or by the milligrams of catalyst are reported. The electroactive surface area (EASA) has been calculated using the Hydroquinone (HQ) as redox probe. The detailed procedure is reported in the experimental chapter.

pH	**ORR$_{\text{onset}}$ (V)**	**E_{peak} (V)**	**j_{peak} (mA cm^{-2})**	**j_{norm} mA mg^{-1}**
1.0	0.40	0.18	-3.6	8.7
7.4	0.53	0.40	-2.3	5.5
13.0	0.71	0.59	-1.79	4.3

Table 3.7. The potential values reported in the table are referred to the RHE reference electrode. The current density values are normalized by the electroactive surface area (EASA) obtained using hydroquinone as redox probe. Further normalization by the amount of catalyst is also reported.

The total current densities increased when passing from alkaline pH to acidic pH. However, subtracting the capacitive currents, the faradaic current appeared similar for the three different pH conditions, suggesting that the activity of g-N-CNHs did not suffer by the pH change. The most positive onset potential (0.71V vs RHE) has been found when working at pH 13. However, the onset potentials at pH 1 and pH 7.4 are also positive, respectively 0.40V and 0.53V vs RHE, highlighting that the catalyst can work at very favourable potentials at all three pH, underpinning the high flexibility of the system.

In order to determine the number of the electrons involved in the reaction, and recognize the major product, rotating disk electrode (RDE) experiments were performed at each pH condition. The K-L plots (figure 3.26) have been obtained plotting the reverse of j (j^{-1}) versus the rate of the electrode rotation (ω) as $\omega^{-1/2}$. The values of j were collected performing linear sweep voltammetry (LSV) experiments in the potential range from 1.2V to -0.35V vs RHE, at 0.005 V s^{-1}.

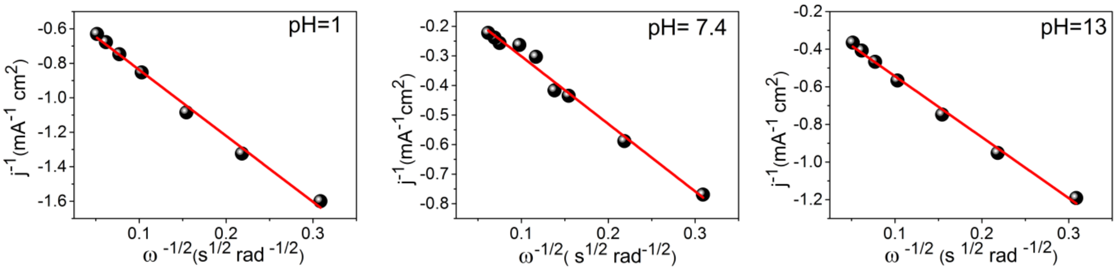

Figure 3.26. the calculated K-L plots for the ORR performed in a) pH 1 in 0.1 M H_2SO_4; b) pH 7.4 in 0.1 M PBS; c) pH 13 0.1 M NaOH. The current density j is normalized by the geometric area of the RDE.

The linearity of the K-L plots implies a first order reaction toward dissolved O_2 at each pH condition. (21)The calculated number of involved electrons from equation (3) was 2.6±0.2 at pH 1, 2.0±0.1 at pH 7.4 and 3.1±0.2 at pH 13, suggesting a lower selectivity at pH 13.0, where the 4-electron reduction to water becomes a competitive pathway. The differences in selectivity as a function of pH supported the view that ORR is driven by a proton-coupled electron transfer mechanism and that the amount of protons surrounding the O_2^- formed after the first electron transfer strongly influences the reaction direction to a 2-electron pathway or to a 4-electron pathway, as as also indicated by kinetic studies reported in literature. (22)

Rotating Ring Disk Electrode experiments (RRDE) were performed under the same pH conditions to corroborate selectivity of the process. The number of electrons *n* calculated (equation 3) from the ratio of disk and ring currents are 2.4 and 3.2 at pHs 1.0 and 13.0, respectively (Table 3.8 and Table 3.9). The values are consistent with the RDE experiments.

$$n = 4 - 2\,(I_R / N) / I_D \qquad (3)$$

pH	ORR $_{onset}$ (V)	E_{peak} (V)	j_{peak} (mA cm^{-2})	j_{norm} mA mg^{-1}	Ne^- (RRDE)
1.0	0.40	0.18	-3.6	8.7	2.4
7.4	0.53	0.40	-2.3	5.5	2.1*
13.0	0.71	0.59	-1.79	4.3	3.2

* The RRDE experiments performed in neutral media were affected by instability problems of the ring current attributed to phosphate surface adsorption; the Ne^- value was derived from Koutecky-Levich plots obtained with the same experimental setup.

Table 3.8. The potential values reported in the table are referred to the RHE reference electrode.

The current density values are normalized by the electroactive surface area (EASA) obtained using hydroquinone as redox probe. Further normalization by the amount of catalyst is also reported.

pH	E_{onset} (V_{RHE})	E_{stop} (V_{RHE})	$E_{1/2}$ (V_{RHE})		Ne^-	Ne^- (average)
13	0.797	0.554	0.694	Potential	E = 0.364 V(a)	E = 0.464 ÷ 0.214 V(b)
				K.L.	2.97	2.89
				RRDE	3.17	3.22
7.4	0.484	0.244	0.354	Potential	E = 0.244 V(e)	E = 0.134 ÷ -0.116 V(b)
				K.L.	1.96	2.14
				RRDE	3.4(d)	N/A(d)
1.0	0.466	0.192	0.366	Potential	E = -0.044 V(a)	$E_{K.L.}$ = -0.014 ÷ 0.416V(c) E_{RRDE} = -0.384 ÷ -0.094 V(c)
				K.L.	N/A(f)	2.79
				RRDE	2.74	2.4

(a) The potential was chosen according to the position of limiting current plateau.
(b) The potential range was chosen according to the value of the correlation constant $R^2 > 0.995$
(c) The potential range was chosen according to the position of limiting current plateau.
(d) Values were undefined due to instability of the ring current value.
(e) Vertex potential.
(f) Low R^2 (< 0.995).

Table 3.9: Relevant data obtained by Rotating Ring-Disk Electrode (RRDE) experiments.

Fixed potential bulk electrolysis experiments were performed at the three different pH, using three different potentials for each pH, to quantify products and assess stability. The potential values were chosen from the CV profiles for each pH conditions. Such additional experiments were performed to compare the material versus those of other several reported studies, where it was found that more cathodic potential were less selective towards H_2O_2 production. (43) (32) (44) Figure 3.27 reports faradaic efficiencies (FE) found for each applied potential at each pH value. The FE was calculated over 1h long experiments.

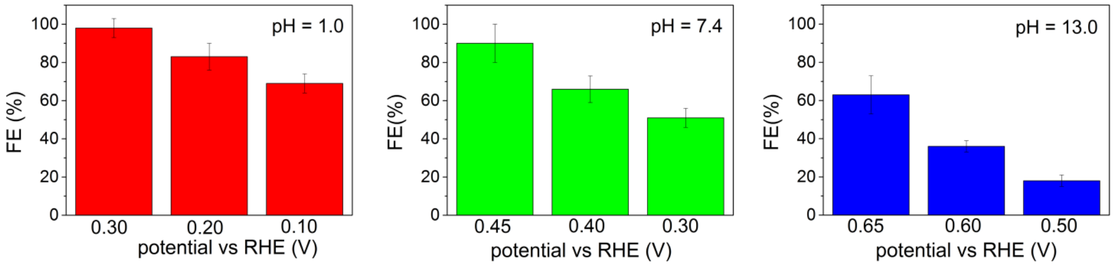

Figure 3.27. FE% of H_2O_2 produced using **g-N-CNHs** modified electrode at pH 1.0 (a), pH 7.4 (b), pH 13.0 (c) at three different potential values for each medium.

The amount of H_2O_2 was determined by permanganometric titration, and further validated by an electro-sensing method recently developed within our group. (45)

The electrocatalytic performances were evaluated using three different materials batches, suggesting a high reproducibility of the system. Highest FE at each pH were obtained at the potential included between the onset potential and the Ep. Comparing the FE in function of the pH, the best FE was obtained at pH 1, while pH 13.0 resulted in the lowest FE, although still very good (63±10)% after 1h. Considering the best working potentials and the obtained FE, g-N-CNHs nano-hybrid material outperformed the state-of-the-art catalysts, both metal-free or based on precious metals, as summarized in table 3.2.

The long term performance of the catalyst was also evaluated by extended chronoamperometry experiments, the relative graphs are reported in figure 3.28.

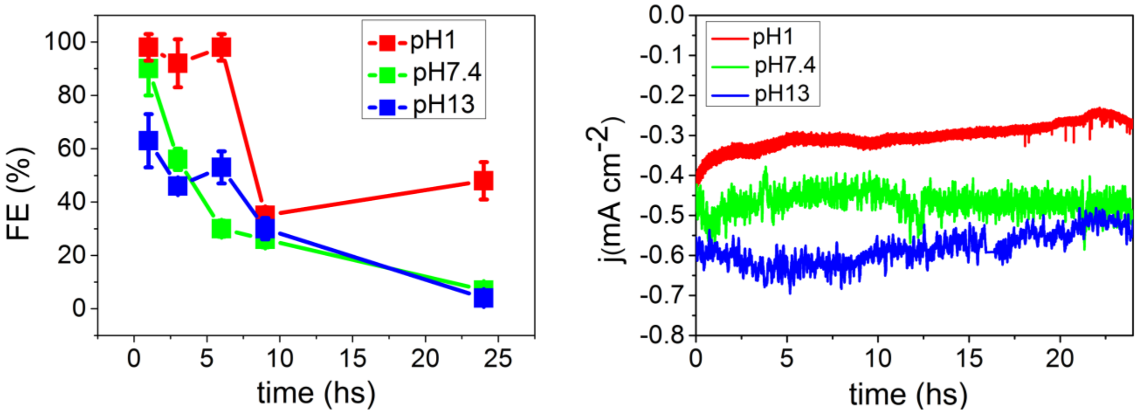

Figure 3.28. left: Plots of FE% vs time, right: stability test at pH 1.0, pH 7.4 and pH 13.0 over 24 h collected using a three electrode cell: working electrode made of **g-N-CNHs** modified glassy carbon, Counter Electrode made of Pt net separate from the bulk solution using a porous membrane and reference electrode Ag/AgCl.

FE within the first 6 hours of experiment remained constant at pH 1 and pH 13, suggesting high stability of the electrocatalyst at acidic and basic condition. FE decrease in these two working environments became appreciable after the 6th hour. Despite the decrease of H_2O_2, after 24hs of experiment the H_2O_2 evolution can be still considered good at acidic pH, approaching a value of (48±7)%.

When operating at pH 7.4, FE drops much more rapidly, decreasing to a (30±3)% after the 6th experiment hour. However, the current densities exhibited a very stable profile over the 24hs suggesting that the catalyst activity should not change by much after long experiment time. Thus, the FE decrease should not be related to the catalyst's efficiencybut likely to the gradual decomposition of H_2O_2 over long time experiment.

The long-term performance for the selective H_2O_2 production can be strongly influenced by reaction conditions. In particular harsh conditions such as very acidic or very basic pH can gradually age the electrocatalyst. Moreover, the accumulation of H_2O_2 during the electrolysis experiments slowly decomposes to release OH· and OOH· radicals, that can result aggressive towards the electrocatalyst, contributing to the aging of the catalyst with consequent decrease of activity and selectivity. (44) However, the observed behavior of the FE over time at acidic and alkaline pH together with the stable current densities calls for minor modification of the catalyst over time, but rather to a decomposition of the H_2O_2, which has been already reported for other catalytic systems.

The mechanism by which O_2 reduction occurs using metal-free N-doped nano-carbon materials is still under debate. Literature findings suggest that the porosity, the amount and the hybridization of N atoms play a critical role. (34)

Electrochemical impedance spectroscopy (EIS) experiments were performed in order to gain some insights into the mechanism. The impedance responses were screened in O_2 saturated electrolyte, at the potential value corresponding to the optimal FE in H_2O_2, by superimposing an alternate current (AC) signal of 0.01 V amplitude over the frequency range from 10^5 to 10^{-2} Hz.

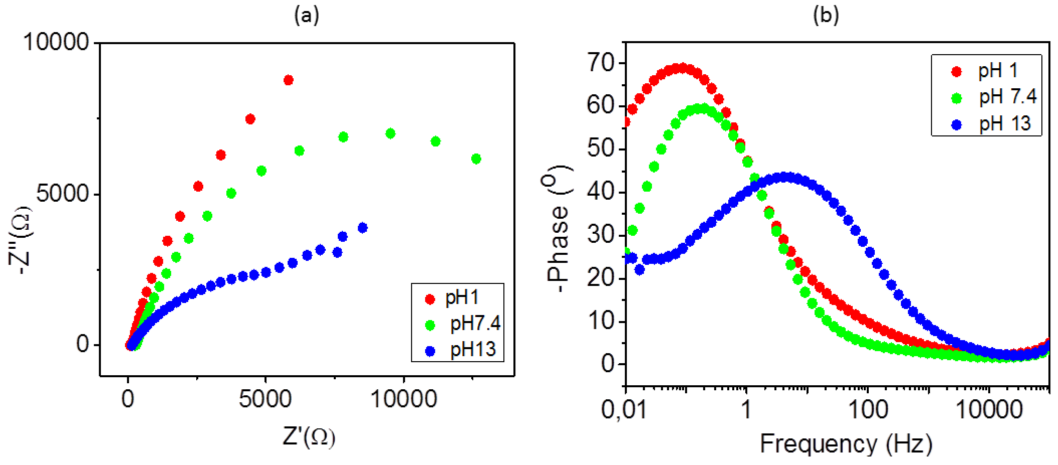

Figure 3.29. Nyquist (a) and Bode (b) diagrams obtained in the O_2 saturated electrolyte solution: 0.1 M H_2SO_4 (●), 0.1 M PBS (●) and 0.1 M NaOH (●).

In figure 3.29 the Nyquist and the Bode-phase plots for each pH are compared. The real and imaginary components of Nyquist diagrams diminished in the sequence pH 1 > pH 7.4 > pH 13; furthermore, Nyquist and Bode plots exhibited different shapes, probably related to different electrochemical processes. Unlike at pH 1 and pH 7.4, two loops and two time constants in Nyquist and phase diagrams appeared at pH 13. These findings were consistent with the results obtained by the K-L plots: at pH 13 the involved electrons were 3.1, in agreement with the concomitance of 4-electrons and 2-electrons pathways. At pH 13.0 the first time constant can be associated to the reduction of O_2 and the formation of H_2O_2, meanwhile, the second time constant can be attributed to a second electron transfer step, presumably the further reduction of H_2O_2 to the formation of H_2O. The lowest selectivity for H_2O_2 formation in NaOH environment was also justified by lower FE than those observed in H_2SO_4 and PBS electrolytes. In contrast, the further reduction of H_2O_2 to H_2O appeared strongly disfavored in H_2SO_4 and PBS based-electrolytes, in agreement with the higher FEs.

The material here reported bears a large microporosity, which influenced the mass transfer and electron transfer processes. The N-doping affects hydrophilicity, basicity and surface electronic properties increasing the mobility of the charge carriers onto the nano-carbon surface. N-doping affects also the work function at the C/O_2 interface, lowering it and favouring the O_2 physisorption onto the g-N-CNHs surface. Moreover, high activity for the ORR should be considered as the result of the synergy between the carbon nanoscaffold used, which assured highly available surface and appropriate electrical properties and the N-doping. (34) (46) In particular, as the XPS analysis points, there were only pyridinic and pyrrolic N, the most reactive N species towards ORR, able to promote it at lower overpotentials. The N-doping plays a crucial role towards the ORR catalysis. In the study reported by Quao et. al the increase of quaternary N was associated to an increase in H_2O production. Based on this findings, the formation of only pyridinic and pyrrolic N could be associated to the high selectivity towards H_2O_2, suggesting that the quality of N-moieties strongly affects the process.

It can be reasonably hypothesized that one key aspect for ensuring high selectivity (especially at acidic pH) was closely associated to the operative conditions applied, in particular the fact that the catalyst was active at very low overpotentials. The vast majority of the other studies operated at more negative applied potentials, obtained mixed products or only H_2O. This was proved by the drop in FEs when the bulk electrolysis experiments were performed at less positive potential, where there was higher competition with the 4-electron pathway. In addition, the microporosity of the material also played a crucial game, as the presence of micropores decreased the residence time of the H_2O_2 on the material, contributing to prevent the further reduction to water. It was however notable that the pH strongly influenced the mechanism, which was likely different when passing from acid to alkaline electrolytes. To prove this, we calculated Tafel plots from RDE experiments at the three pHs (figure 3.30). The catalyst exhibited linear Tafel plots in acidic, neutral and alkaline media. The corresponding Tafel slopes were found to be 95 mV dec^{-1} for the pH = 1.0, 84 mV dec^{-1} for the pH = 7.4 and 71 mV dec^{-1} for the pH = 13.0. At lower potentials, the curves were bent downwards and there were no well-defined linear region found in the plot.

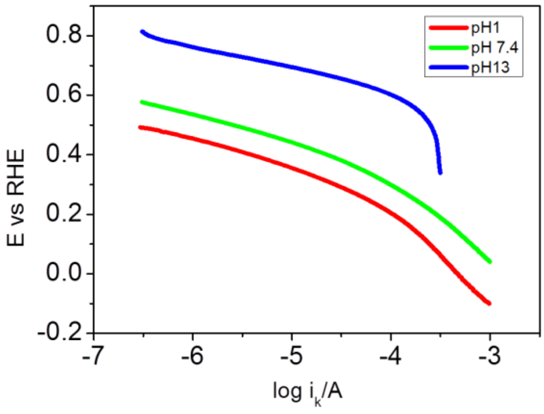

Figure 3.30 Tafel plots of log I_K vs. E (V) for the ORR on the g-N-CNHs electrode in oxygen-saturated solution at pH 1.0 (🟥), at pH 7.4 (🟩) and at pH 13.0 (🟦) under O_2. Scan rate: 0.05 V s^{-1}. RDE rotation rate: 1200 rpm.

The Tafel plots strongly indicated a different mechanism occurring at higher pH as compared to acidic pH. The different Nernstian slopes obtained well agree with previous data reported in literature and referred to heteroatom–doped carbon based catalysts for the ORR process (60-120 mV dec^{-1}) (47) (48) (49)[.Accordingly to RRDE results, a Tafel slope decrease from 95 mV dec^{-1} (acid environment) to ca. 70 mV dec^{-1} (alkaline environment) is consistent with the change in the reaction pathway from 2e- to (2+2)e- transfer process and the corresponding rate determining step.

Given its complexity, the complete mechanism of the ORR catalyzed by N-doped carbon materials is still under open discussion. Hence, the findings found in this work may shed new light and allow a more convergent view.

3.3.1.5 Conclusion

A novel hierarchical material has been designed and developed conjugating the electronic and structural properties of the SWCNHs as carbon nanoscaffold, and the catalytic properties of an N-doped graphitic layer. The final material named g-N-CNHs**,** consisted of a CNHs core enveloped into a highly doped graphitic shell, with extended microporosity and high surface area, which contributed to O_2 adsorption. The electronic properties of the carbon core and shell allowed an improved conductivity and a facilitation of electron transfer processes. The N-doping and the types of introduced N atoms, played a crucial role in driving the O_2 reduction decreasing the working potentials, and the work function at the interface C/O_2, In particular, the catalyst was able to drive O_2 reduction to selective formation of H_2O_2 with high efficiency, under different reaction environments.

The catalytic performance in particular, were comparable or in most cases superior to state-of-the art catalysts. g-N-CNHs was able to trigger the O_2 reduction at very positive potentials, 0.40 V at pH 1.0, 0.53 V at pH 7.4, 0.71 V at pH 13.0 with high FE, 98% at pH 1. The high stability over long time experiment and the high flexibility to operate in a wide pH range (1-13) make it a forefront electrocatalyst in the development of industry focused setups for the production of H_2O_2 and simultaneously as a prominent cathodic material for fuel cell applications.

3.4 References

1. J. Snyder, K. Livi, J. Erlebacher, *Adv. Funct. Mater.,* **2013**, Vol. 23, p. 5494-5501.

2. C. Samanta et al. ,*Appl. Catal. A,*. **2008**, Vol. 350, p. 133.

3. F. Jaouen, E. Proietti, M. Lefevre, R. Chenitz, J. P. Dodelet, G. Wu, H. T. Chung, C. M. Johnston, P. Zelenay, *Energ. Environ. Sci.,* **2011**, Vol. 4, p. 114-130.

4. M. Winter, R. J. Brodd**,** *Chem. Rev.,* **2004**, Vol. 104, p. 4245-4269.

5. S. C.Thomas, X. Ren, S. Gottesfeld, P. Zelenay, *Electrochimica Acta,* **2002**, Vol. 47, p. 3741-3748.

6. Arnau Verdaguer-Casadevall, Davide Deiana, Mohammadreza Karamad, Samira Siahrostami,Paolo Malacrida, Thomas W. Hansen, Jan Rossmeisl, Ib Chorkendorff, Ifan E. L. Stephens, *Nano Lett.*, **2014**, p. 1603-1608.

7. F. Jaouen, E. Proietti, M. Lefevre, R. Chenitz, J. P. Dodolet, G. Wu, H. T. Chung, C. M. Johnston, P. Zelenay,**.** *Energy Environ. Sci.,* **2011**, Vol. 4, p. 114-130.

8. M. Winter, R. J. Brodd**,** *Chem. Rev.* **2004**, Vol. 104, p. 4245-4269.

9. S. C. Thomas, X. Ren, S. Gottesfeld, P. Zelenay**,** *Electrochim. Acta.,* **2002,** Vol. 47, p. 3741-3748.

10. D. W. Kim, O. L. Li,N. Saito, *Phys. Chem. Chem. Phys.,* **2014**, Vol. 16, p. 14905-14911.

11. Jiayuan Li, Guoxiong Wang, Jing Wang, Shu Miao, Mingming Wei, Fan Yang, Liang Yu, Xinhe Bao, *Nano Res. ,***2014**, Vol. 7, p. 1519-1527.

12. D. Deng, L. Yu, X. Chen, G. Wang, L. Jin, X. Pan, J. Deng, G. Sun, X. Bao, *Angew. Chem. Int. Ed.,* **2013**, Vol. 52, p. 371-375.

13. Y. Cheng, C. Xu, L. Jia, J. D. Gale, L. Zhang, C. Liu, P. K. Shen, S. P. Jiang, *Applied Catalysis B: Environmental.***,** **2015**, Vol. 163, p. 96-104.

14. B. E. Logan, J. M. Regan, *Environ. Sci. Technol.,* **2006**, Vol. 40, p. 5172-5180.

15. B. E. Logan, B. Hamelers, R. Rozendal, U. Schroeder, J. Keller, S. Freguia,P. Aelterman, W. Verstraete, K. Rabaey**,** *Environ. Sci. Technol.,* **2006**, Vol. 40, p. 5181-5192.

16. C. Picioreanu, I. M. Head, K. P. Katuri, M. C. M. van., *Water. Res.,* **2007**, Vol. 41, p. 2921-2940.

17. J. Bahr, J. M. Tour**,** *Chem. Mater.,* **2001**, Vol. 13, p. 3823-3824.

18. H.Z. Geng, X.B. Zhang, S.H. Mao, A. Kleinhammes, H. Shimoda, Y. Wu, O. Zhou, *Chem. Phys. Lett.,***. 2004,** Vol. 399, p. 109-113**.**

19**.** M. Hoefer, P. R. Bandaru,, *App. Phys. Lett.*, **2009,** Vol. 95, p. 183108/1-183108/3.

20.. S. Agrawal, M. S. Raghuveer,H. Li, G. Ramanath, *Appl. Phys. Lett.,* **2007,** Vol. 90, p. 193104/1-193104/3.

21. A. J. Bard, L. R. Faulkner, *Electrochemical methods, Fundamentals and Applications.*. New York : s.n., **2001.**

22. E. C. Zimmerman, C. J. Barile, N. A. Kirchschlager, Y. Li, P. Gerwats, S. C. Zimmerman, A. Hosseini, A. A. Gewirth, *Nature Mater.,* **2016,** Vol. 15, p. 754-759.

23. S. Fukumi, Y. Yamada, K. D. Karlin,. *Electrochim. Acta,***.** **2012,** Vol. 82, p. 493.

24. *Hydrogen peroxide " Ullman's Encyclopedia of industrial Chemistry".* Goor, G., Glenneberg, J. e Jacobi, S. s.l. : Weinheim: Wiley-VCH, **2007.**

25.Y. Izumi, *US Patent 4009252,* **1978.**

26. L. W. Gosset *, US patent 4681751,* **1988.**

27. R. Black, B. Adams, L. F. Nazar,. *Adv. Energy Mater.* **2012,** Vol. 2, p. 801.

28. R. Cao, J. S. Lee, M. L. Liu, J. Cho, *Adv. Energy Mater.,* **2012,** Vol. 2, p. 816.

29. J. S. Jirkovsky, I. Panas, E. Ahlberg, M. H. Halasall, S. Romani, D. J. Schiffrin, *J. Am. Chem. Soc.,* **2011,** p. 19432-19441.

30. S. Siahrostami, A. Verdaguer-Casadeval, M. Karamad, D. Deiana, P. Malacrida, B. Wickman, M. Escudero-Escribano, E. A. Paoli, R. Frydendal, T. W. Hansen, I. Chorkendorff, I. E. L. Stephens, J. Rosmeisl, *Nat. Mater.,* **2013,** Vol. 12, p. 1137-1142.

31. T. P. Fellinger, F. Hasché, P. Strasser, M. Antonietti, *J. Am. Chem. Soc.,* **2012,** Vol. 134, p. 4072-4075.

32. Y. Liu, X. Quan, X. Fan, H. Wang, S. Chen, *Angew. Chem. Int. Ed.***,** **2015**, Vol. 54, p. 6837-6841.

33. C. H. Choi, H. C. Kwon, S. Yook, H. Shin, M.Choi, *J. Phys. Chem. C,* **2014,** Vol. 118, p. 30063-30070.

34. D. Guo, R. Shibuya, C. Akiba, S. Saji, T. Kondo, J. Nakamura, *Science,* **2016,** Vol. 351, p. 361-365.

35. A. Koòs et al., *Phys. Chem. Chem. Phys.,* **2013,** Vol. 43, p. 19446-19452.

36. al., A. Dorjgotov et al., *J. Appl. Electrochem.,* **2013**, Vol. 43, p. 387-397**.**

37. W. Ding, Z. Wei, S. Chen, X. Qi, T. Yang, S. Hu, D. Wang, L. J. Wan, S. F. Alvi, L. Li, *Angew. Chem. Int. Ed.***,** **2013,** Vol. 52, p. 11755-11759**.**

38. A. Dimitru, M. Mamlouk, K. Scott, *Electrochim. Acta,* **2014,** Vol. 135, p. 428-438.

39. A. Hashimoto et al., *Proc. Natl. Acad. Sci. U.S.A.,* **2004,** Vol. 23, p. 8527-8530.

40. Proc. Natl. Acad. Sci. U. S. A., **2004,** Vol. 23, p. 8527-8530.

41. Bernsmann, F. *J. Phys. Chem. C.***,** **2009,** Vol. 13, p. 3914-3919.

42. F. Bernmann, J. C. Voegel, V. Ball, *Electrochem. Acta,* **2011,** Vol. 56, p. 3914-3919.

43. V. Perazzolo, C. Durante, R. Pilot, A. Paduano, J. Zheng, G. A. Rizzi, A. Martucci, G. Granozzi, A. Gennaro, *Carbon,* **2015,** Vol. 95, p. 949-963

44. Frédéric Hasché, Mehtap Oezaslan , Peter Strasser ,Tim-Patrick Fellinger, *J. Energ. Chem,* **2016,** 10.1016/j.jechem.2016.01.024.

45. M. V. Bracamonte, . Mechionna, A. Giuliani, L. Nasi, C. Tavagnacco, P. Fornasiero, M. Prato, *Sens. Actuators B,* **2017,** Vol. 239, p. 923-932.

46. K. Wan, Z. Yu, X. Li, M. Liu, G. Yang, J. Piao, Z. Liang, *ACS Catal,* **2015,** Vol. 5, p. 4325-4332.

47. T. Shinagawa et al., *Sci. Rep,.* **2015,** Vol. 5, p. 13801.

48. Feng, Xinliang. s.l. : Wiley-VCH Verlag Gmbh&Co, **2015.**

49. T. Lopes et al., *ChemElectroChem.* **2016,** Vol. 3, p. 1580-1590.

50. A. Verdaguer-Casadevall, D. Deiana, M. Karamad, S. Siahrostami, P. Malacrida, T. W. Hansen, J. Rossmeisl, I. Chorkendorffand, I. E. L. Stephens, *Nano Lett.,* **2014,** Vol. 14, p. 1603-1608.

CHAPTER 4
A new highly sensitive and versatile H_2O_2 sensor based on carbon nanohorns/cerium dioxide hybrids

4.1 Introduction

Hydrogen peroxide (H_2O_2) is a ubiquitous molecule involved in many processes. It is a signaling molecule in enzymatic processes, and extensively used in food, pharmaceutical, and clinical industry. (1) (2) (3) (4) For this reason, H_2O_2 detection represents a crucial topic of research from a number of perspectives. Several methods based on titration and fluorescence, (5) chemiluminescence (6) and spectrophotometry (7) have been employed. Nevertheless, each of these methods suffer from important drawbacks. The most common reactants for titration ($KMnO_4$ and $CeSO_4$) oxidize the organic matter present in the sample matrix, thus altering results. On the other hand, spectrophotometric methods exhibit incompatibility with samples containing dispersed particulate or dissolved species, which can absorb light in a broad wavelength range. Electrochemical methods for sensing H_2O_2 are particularly advantageous due to their robustness, simplicity and sensitivity. (8)

This chapter focuses on the design, synthesis and characterization of a novel nanohybrid based on the well-suited interfacing of single-walled carbon nanohorns (SWCNHs) and cerium dioxide (CeO_2), named ox-SWCNHs@CeO_2, which shows high effectiveness for the selective electroreduction of H_2O_2, thus being a competitive candidate for its sensing . In particular, ox-SWCNHs@CeO_2 exhibited higher selectivity, reproducibility and sensitivity than the bare CeO_2, which has already been reported as a H_2O_2 amperometric sensor. The electrocatalyst has been also tested in real case studies such as washing liquids and milk and was confirmed to be a robust and highly selective material, being not affected by the presence of complex matrices. The high recovery confirmed its excellent specificity and flexibility.

4.2 General aspects on catalytic systems for electrochemical H_2O_2 sensing

H_2O_2 amperometric sensors developed until now can be classified in enzymatic sensors and non-enzymatic sensors. Enzymatic amperometric sensors show excellent sensitivity, due to the high selectivity of the enzyme selected as active site, mainly horseradish peroxidase (HRP), catalase, cytochrome c, hemoglobin, microperoxidase and myoglobin. (9) (10) However, the use of enzyme based amperometric sensors suffers from some critical disadvantages; they are a) sensitive to denaturation processes due to the operating environment conditions; (11) b) expensive because of their purification protocols; (12) c) the immobilization procedures are complicated (13) and, d) they are hampered by slow electron transfer communication between the electrode surface and enzyme active site, because of the insulating protein surrounding the active site. (14) The development of non-enzymatic amperometric sensors has therefore gained increasing interest. In table 4.1, some recent examples of some non-enzymatic amperometric sensors are reported.

Catalyst	***E_{ap} (V vs Ag/AgCl)$^{a)}$***	***Linear range (mM)***	***Sensitivity (µA mM^{-1} cm^{-2})$^{c)}$***	***LOD (µM)***	***Ref***
PSCN$^{b)}$	n.r.	0.008–0.07	n.r.	3.4	(15)
Co_9S_8/GC	-0.4	0.0001-11.11	267.2	0.02	(16)
Cu-MOF	-0.2	0.001–0.9	0.019 uA mM^{-1} $^{d)}$	1.0	(17)
N-GrNRs	−0.4	0.005–0.085	525	1.72	(18)
Magnetite	−0.2	0.001–2.5	40.00 uA mM^{-1} $^{d)}$	7.3	(19).
Cobalt ferrite	−0.2	0.002–1.5	7.03 uA mM^{-1} $^{d)}$	14.0	(19)
Nickel ferrite	−0.2	0.002–1.5	5.23 uA mM^{-1} $^{d)}$	9.2	(19)
Mb/CeO_2/ITO	−0.3	n.r.	5.4	0.6	(20)
Au–MnO_2–rGO	−0.2	0.022-12	101.6	0.05	(21)
Fe@Fe-O@Ag	−0.4	0.005 - 1	0.460	0.005	(22)

Table 4.1 : Summary table of electrochemical performance of different hydrogen peroxide sensors using metal and metal oxides.

In principle noble metal-based nanomaterials for electrodes modification could be easier to handle than enzymatic sensors, however, they present other disadvantages: a) cost b) high overpotentials either for reduction and oxidation of H_2O_2, c) slow kinetics. (23) These reasons have motivated scientists to develop catalysts based on non-precious metals such as CuO, TiO_2, MnO_2, Fe_3O_4, Co_3O_4, MoS_2, and CuS, which bring assets in terms of cost, natural abundance and environmental friendliness. (24) In order to develop non precious metal catalysts, it is important to solve problems related to the tendency to agglomeration, which lowers surface area, and the abundance of the active sites.

The design of the catalyst described herein follows the concept of a hierarchical organization. A catalyst support made by carbon nanostructure, in particular SWCNHs, can avoid the agglomeration of the nanoscaled active sites, while improving the conductivity of the resulting nanohybrid. Among the various metal oxides used for catalysis, Cerium oxide (CeO_2), has gained a prominent role in view of its free scavenging and redox properties, finding application in biology, medicine, environmental and energy related applications. As far as electrochemistry is concerned, CeO_2 is particularly intriguing due to the presence of highly mobile lattice oxygen which facilitates the interconversion Ce^{3+}/Ce^{4+}. (25) (26) (20) In the context of H_2O_2 sensing, nano-CeO_2 can play the role of either an oxidation catalyst or a reduction catalyst depending on the reaction conditions. It has been considered as an artificial enzyme depending on Ce^{3+}/Ce^{4+} ratio: at high ratios, it functions in a way similar to the superoxidase enzyme (SOD) which operates the dismutation of O_2^- in water and H_2O_2; at low Ce^{3+}/Ce^{4+} ratios, it works as a catalase enzyme (CAT) which lead to the decomposition of H_2O_2 in H_2O and O_2. (27)

Here, nano-CeO_2 opportunely supported onto ox-SWCNHs, was used as catalyst for H_2O_2 detection via a reduction process. The nano-hybrid ox-SWCNHs@CeO_2 was prepared using a sol-gel method that allows a uniform covering of the SWCNHs and an intimate contact of the two phases. This approach has the advantage to make most of the CeO_2 available for the H_2O_2 interaction and improve its electronic and catalytic properties because of the high surface-volume ratio of ox-SWCNHs and their high conductivity**.** ox-SWCNHs@CeO_2, as obtained, showed better sensitivity than the individual components, nano-CeO_2 and ox-SWCNHs.

4.3 Results and discussion

4.3.1. Synthesis

ox-SWCNHs@CeO_2 were obtained using a sol-gel protocol. Prior to hybridization of the two phases, pristine SWCNHs were first oxidized ifor three specific reasons: 1) to introduce oxygen containing groups such as as –OH, COOH, epoxyde carbonyls able to drive and anchor CeO_2 layering,; 2) to improve dispersibility of the material in liquid media; 3) to open the tips and increase the available surface. The mild oxidation, being the same as that described in Chapter 2, allows a good preservation of the electronic properties of the carbon scaffold. Scheme 4.1 provides a graphical description of the synthesis

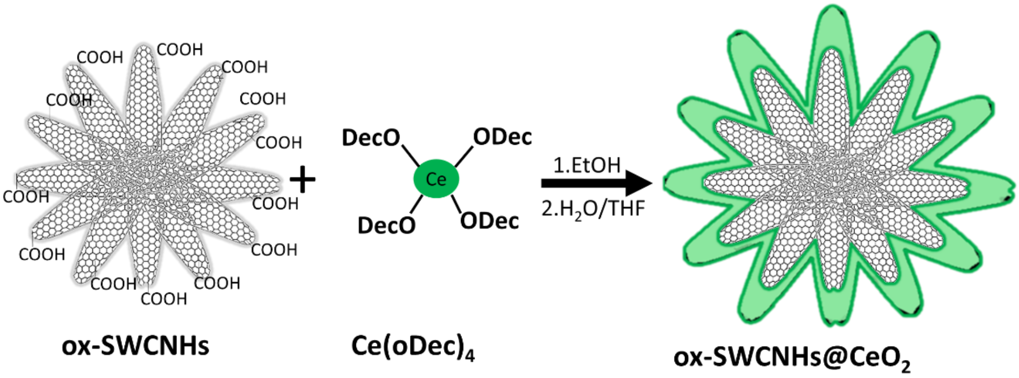

Scheme 4.1. Scheme of the reaction between ox-SWCNHs and $Ce(ODec)_4$.

$Ce(ODe)_4$ (ODe =decyloxide), CeO_2 precursor, was slowly added to the suspension of ox-SWCNHs in EtOH. The reaction was kept under sonication for 30 minutes. During this time, $Ce(ODe)_4$ underwent ligand exchange with the oxygenic groups of the ox-SWCNHs thus resulting in an homogeneous coating of the carbon support. A slow addition of H_2O/THF mixtures allowed final hydrolysis of the Ce precursor to form amorphous CeO_2. The final material was then isolated by filtration, and washed in succession with H_2O/EtOH, and with pure EtOH. Before the use, the material was dried at 80°C overnight.

In order to evaluate the possible increase of activity by having a crystalline CeO_2 phase, some of the material was subjected to a thermal treatment at 250 C. The temperature for the calcination was chosen based on TGA data (see below), in order to guarantee crystallization without removing the carbon scaffold.

4.3.2 Microscopic and macroscopic characterization

The final hybrid material was fully characterized using a combination of techniques. Thermogravimetric analysis (TGA) under air flow were performed in order to define the real amount of CeO_2 onto ox-SWCNHs**.** By the TGA profile of ox-SWCNHs@CeO_2 reported in figure 4.2a, two distinct weight losses can be observed. The first weight loss at 200°C, was due to combustion of the organic residues of CeO_2 precursor, and the carboxylic groups deriving by the oxidation of the carbon nanostructure. The second weight loss, much more pronounced and occurring between 300°C to 400°C, was ascribed to the combustion of the carbon nanostructure. The residue for the **ox-SWCNHs@CeO_2** is 18%, attributed to CeO_2. It must be noted that the temperature of combustion of the carbon nanostructure is higher (around 600 °C) when they are free standing. The reason of the decreasing of the combustion temperature is attributed to the tight contact between ox-SWCNHs and CeO_2, and therefore the oxidation ability of the CeO_2 shell aids the combustion by a faster oxygen transfer. (28)

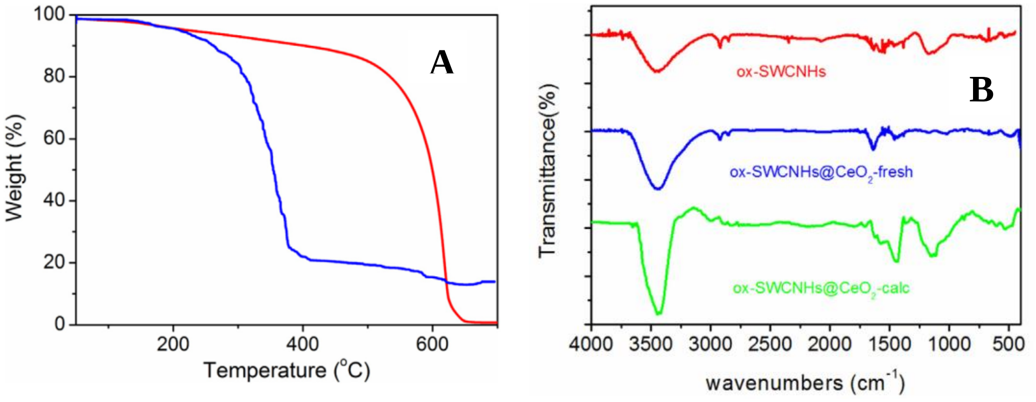

Figure 4.2: A) TGA plots of the (—) ox-SWCNHs and (—) ox-SWCNHs@CeO_2 in air; B) FT-IR spectra of (—) ox-SWCNHs, (—) ox-SWCNHs@CeO_2 and (—) calcined ox-SWCNHs@CeO_2.

FT-IR spectra of ox-SWCNHs (red trace), ox-SWCNHs@CeO_2 (blue trace) and ox-SWCNHs@CeO_2 calcined at 250°C (green trace) are reported in Figure 4.2 B. For each spectrum the broad band due to the –OH stretching is present (3450 cm^{-1}), relative to the presence of adsorbed water molecules. The small band at 494 cm^{-1} observed for ox-SWCNHs@CeO_2 and calcined ox-SWCNHs@CeO_2 is due to the Ce-O stretching mode, which is indicative of the formation of the CeO_2 shell around ox-SWCNHs. The Ce-O band became more intense after the thermal treatment because of the full crystallization of the metal oxide. On the other hand, the spectrum of ox-SWCNHs confirmed the successful mild oxidation treatment. The band at 1637 cm^{-1} due to the stretching of C=O bond and the band at 1170 cm^{-1} due to the C-O stretching confirm the presence of –COOH groups attached to ox-SWCNHs.

Raman spectroscopy (figure 4.3A) shows the characteristic bands of nano-carbon materials: the D (1330 cm^{-1}) and G band (1580 cm^{-1}) and the 2D band (2665 cm^{-1}). By the ratio between the D and G intensity (I_D/I_G), a semi-quantitative information about the functionalization degree of the ox-SWCNHs can be obtained, this is correlated to the introduction of defects into the aromatic pattern, as also described in previous chapters. The I_D/I_G was 1.27 for ox-SWCNHs and did not change after the CeO_2 functionalization, suggesting that –COOH groups drove the CeO_2 functionalization of ox-SWCNHs. No peaks associated to CeO_2 modes were detected, implying that the metal oxide was amorphous. However, increasing the power of the laser, a local crystallization of the CeO_2 could be induced, producing the appearance of the characteristic CeO_2 peaks, in particular the F_{2g} mode is very evident , occurring at 461 cm^{-1}(figure 4.3B) (29).

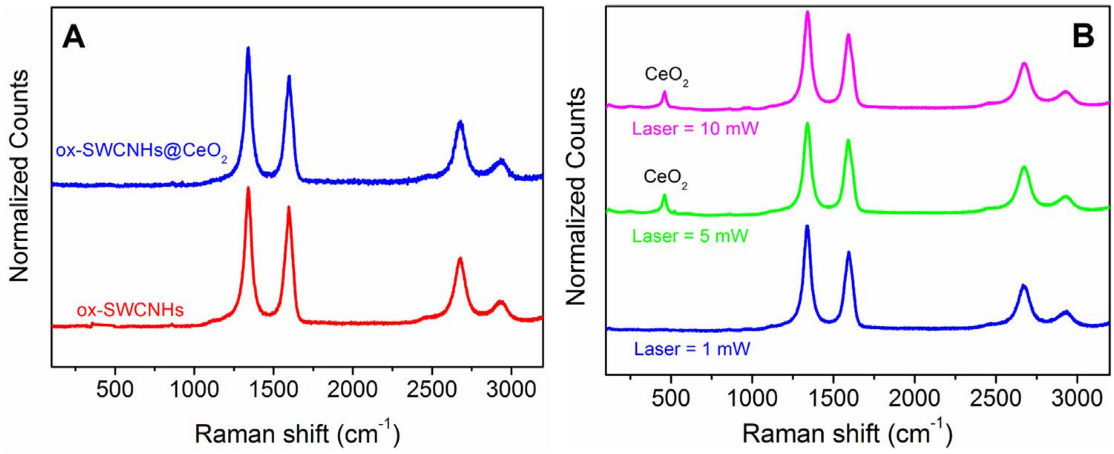

Figure 4.3: A) Raman spectra of the (—) ox-SWCNHs and (—) ox-SWCNHs@CeO_2; B) Raman spectrum of ox-SWCNHs@CeO_2 at different laser powers 1, 5 and 10 mW.

The morphology and composition of the material was investigated by Scanning Transmission Electron Microscopy with High-Angle Annular Dark-Field detector (HAADF-STEM) Energy-Dispersive X-ray spectroscopy (EDX), and Atomic Force Microscopy (AFM).

Figure 4.4 reports the HAADF-STEM and EDX images. A perfect attachment of CeO_2 onto ox-SWCNHs is clearly observed, with no isolated aggregates of CeO_2 . EDX confirms the collocated presence of C, Ce and O atoms.

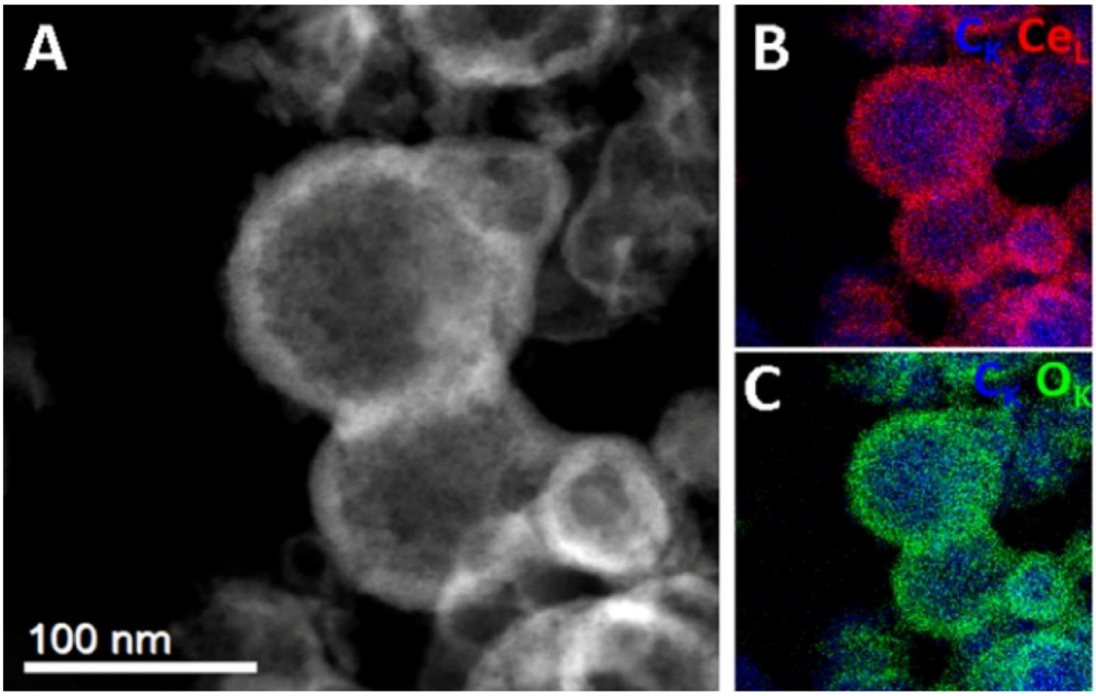

Figure 4.4: A) Representative HAADF-STEM of ox-SWCNHs@CeO2; B) EDX mapping of C and Ce atoms; C) EDX mapping of C and O atoms.

AFM image are reported in figure 4.5. The sample was prepared by drop casting of ox-SWCNHs@CeO_2 solution onto solid support (mica foil). Profile analysis of several particles of ox-SWCNHs@CeO_2 have revealed a size ranging between 50-80 nm, together with some minor smaller aggregates. This has important consequences on the homogeneous covering and the improved efficiency of the catalyst-modified electrode. Thus, the as-prepared nanomaterial dispersions are suitable candidates for more advanced electrode surface modification techniques able to generate single layers of catalyst, thus maximising efficiency.

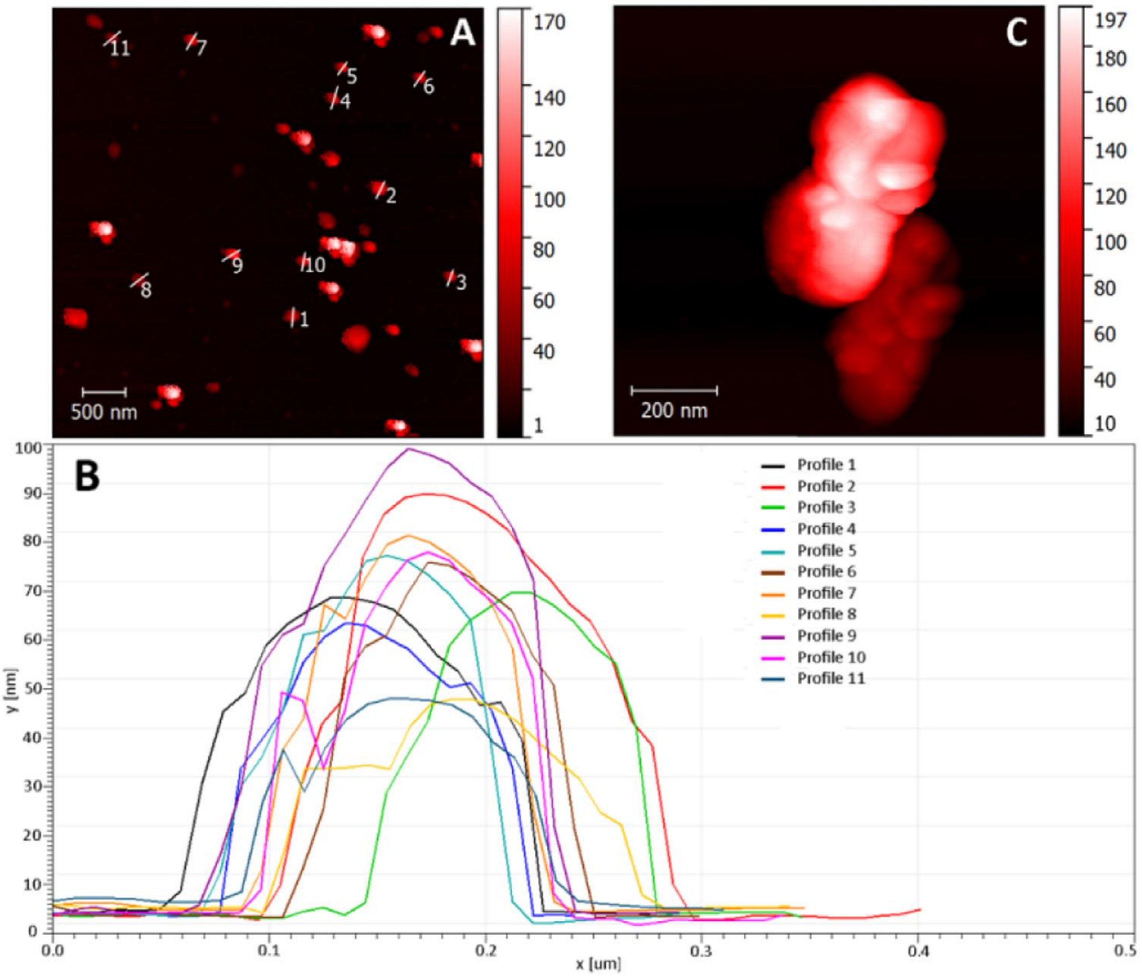

Figure 4.5: A) Representative AFM image of a typical window of the drop casted sample. B) Corresponding heights profile measured on 11 particles (indicated in A). C) AFM expansion of a typical small aggregate where single SWCNHs@CeO_2 can be recognized.

4.3.3. Electrochemical characterization

The electrochemical behavior of the material was first checked by cyclic voltammetry using a three-electrode electrochemical cell. The working electrode, a glassy carbon electrode modified by drop casting with 2.5mg/mL of ox-SWCNHS@CeO_2, was investigated within a potential window -0.5V to 0.9V vs Ag/AgCl in a N_2-saturated buffer solution of 0.1M TRIS-HCl pH 7.4, with a scan rate of 0.10 V s^{-1}. The response of ox-SWCNHs@CeO_2 are compared with the CV responses of ox-SWCNHs and bare GCE electrodes are reported. Only capacitive currents were observed for the bare GCE and the ox-SWCNHs modified GCE, confirming that these materials have no redox response in the explored potential window. Using ox-SWCNHs@CeO_2-modified GCE, the capacitive current increases with concomitant appearance of two peaks: an anodic peak at -0.02V and a cathodic peak at -0.14V vs Ag/AgCl both relative to the redox process Ce^{4+}/Ce^{3+} (30) (31).

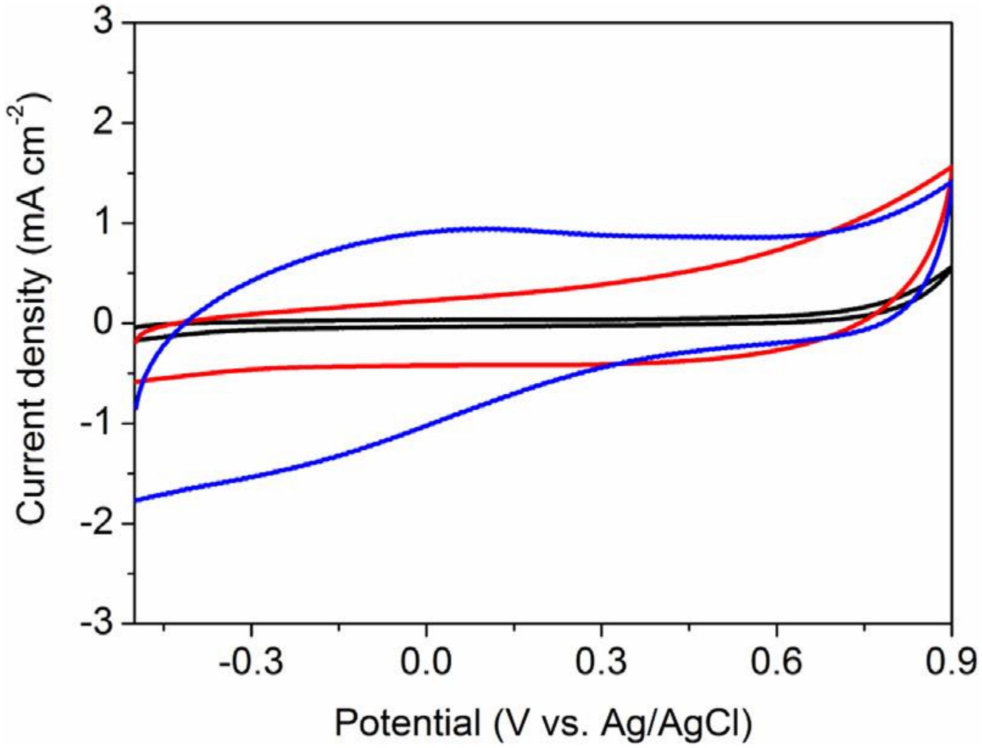

Figure 4.6: CVs obtained on bare (—) and modified GCE with ox-SWCNHs (—) and ox-SWCNHs@CeO2 (—) in 0.10 M TRIS-HCl buffer solution pH 7.40 under N_2. Scan rate: 0.10 V s−1 between −0.50 V and 0.90 V vs Ag/AgCl.

4.3.4 Electrocatalytic response toward H_2O_2 by ox-SWCNHs@CeO_2 modified glassy carbon electrodes

The electrocatalytic response toward H_2O_2 was then evaluated by means of CV. The experiments were performed at neutral pH in a N_2-saturated buffer solution 0.1M TRIS-HCl pH 7.4 in absence and in presence of 5mM H_2O_2. As a term of comparison, the CV profile of bare CeO_2, prepared using the same procedure employed for the synthesis of the hybrid but without the presence of ox-SWCNHs, was also explored and confirmed its poor activity, suggesting that the electron transfer rate at the interface between CeO_2 and GCE was disfavored. In contrast, for ox-SWCNHs/GCE, the cathodic current increased in presence of H_2O_2, with an onset potential of -0.24V vs Ag/AgCl indicating the reduction of H_2O_2 catalyzed by the carbon nanostructures. By conjugation of CeO_2 and ox-SWCNHs to form the hybrid, the cathodic current exhibited a remarkable increase and the onset of H_2O_2 activation moved to lower cathodic potential: -0.11V vs Ag/AgCl.

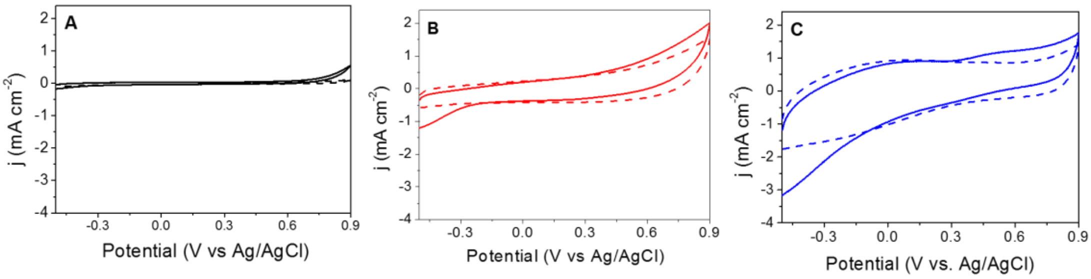

Figure 4.7: CVs at GCE modified with bare CeO_2 (A), ox-SWCNHs (B) and ox-SWCNHs@CeO_2 (C) in 0.10 M TRIS-HCl buffer solution without (dash line) and with (solid line) 5mM H_2O_2. Scan rate: 0.10 V s^{-1}.

Overall, the faradaic currents increased in the order CeO_2< ox-SWCNHs< ox-SWCNHs@CeO_2 at -0.30V vs Ag/AgCl, The fast transition between Ce^{4+} and Ce^{3+}, changing the oxygen vacancies in the CeO_2 formed a n-type hybrids. Moreover, the combination with the nanocarbon component, which incremented the active area and reduced the energy barrier for the electron transfer, crucially contributed to the enhanced activity of ox-SWCNHs@CeO_2 toward the H_2O_2 reduction.

Further electrochemical insights were gained by means of electrochemical impedance spectroscopy (EIS). EIS experiments were performed in the frequency range between 10^5 to 10^{-2} Hz, with a potential perturbation of 0.01V and a working potential of -0.20 V. The experiments were carried out in a solution 25mM H_2O_2 in 0.1M TRIS-HCl pH 7.4 at -0.20 V vs Ag/AgCl using GCE modified with ox-SWCNHs and ox-SWCNHs@CeO_2. The resulting Nyquist plots are reported in figure 4.8.

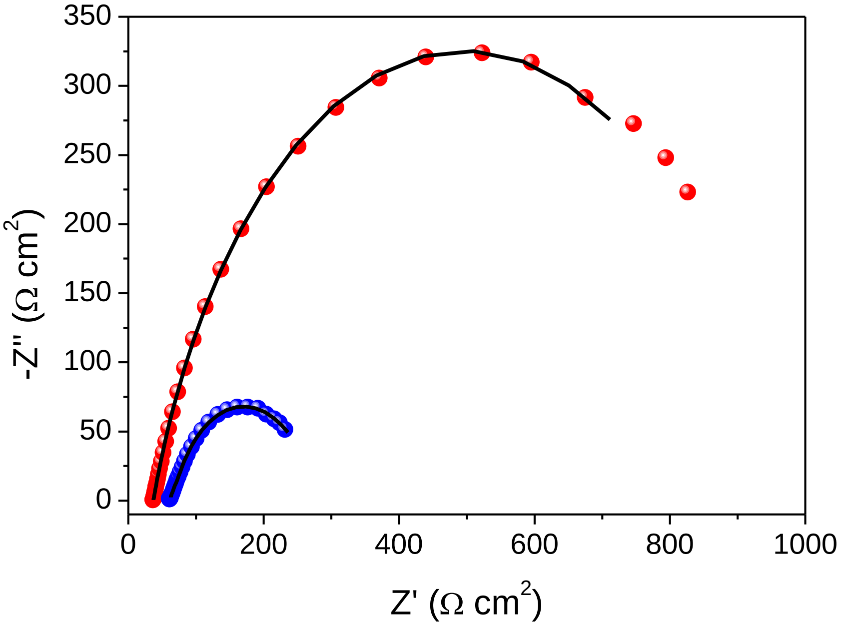

Figure 4.8: Nyquist plots obtained for ox-SWCNHs/GCE (●) and ox- SWCNHs@CeO2/GCE (●). Points indicate the experimental data, lines the corresponding fit with the equivalent circuits presented as an inset.

The equivalent circuit used for the fitting of the Nyquist plot relative to ox-SWCNHs/GCE was different from the equivalent circuit used to fit ox-SWCNHs@CeO_2/GCE. In particular the former can be described as (R_s (R_{ct} C_{dl})), where R_s is the solution resistance, in series with the charge transfer resistance R_{ct} and the constant phase element that represents the double layer capacitance (C_{dl}). In contrast, the equivalent circuit for the latter is represented as (R_s (R_{ct} C_{dl} (R_{ct}^{II} C_{dl}^{II})), with two additional elements arisen from the presence of nano-CeO_2 phase: the C_{dl}^{II}, the capacitance element, and R_{ct}^{II}, the charge transfer resistance element (figure 4.9).

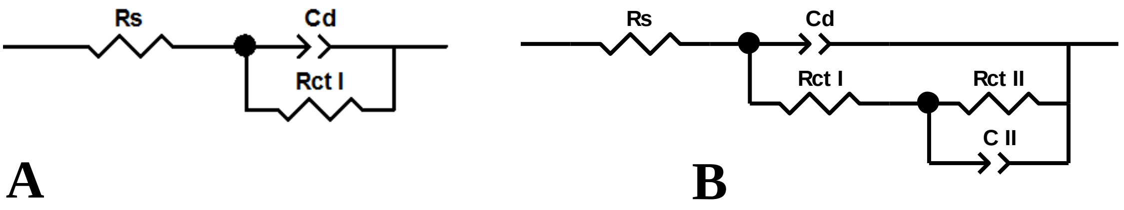

Figure 4.9: Equivalent circuit used to fit the Nyquist plots obtained for ox-SWCNHs@CeO_2 and ox-SWCNHs.

Based on the Nyquist plots, the charge transfer resistance for ox-SWCNHs@CeO_2/GCE was remarkably lower than ox-SWCNHs/GCE. with values of R_{ct} 922±3 Ω cm^{-2} for ox-SWCNHs and 188±4 Ω cm^{-2} for ox-SWCNHs@CeO_2 equal to the sum of R_{ct}+R_{ct}^{II}. These results further highlight the electrochemically favourable combination of ox-SWCNHs and nano-CeO_2, with the intimate contact between the carbon and inorganic phase facilitating the charge transfer between H_2O_2 and the modified electrode surface.

The analytical performance of the final hybrid was evaluated by amperometry collecting the current- time profile obtained at -0.20V for successive additions of 20µL of 50mM H_2O_2 solution (figure 4.10A). The response of ox-SWCNHs@CeO_2 were compared with the responses recorded using CeO_2/GCE and ox-SWCNHs/GCE in the same conditions. The calibration plots obtained from the amperometric experiments are reported in figure 4.10B.

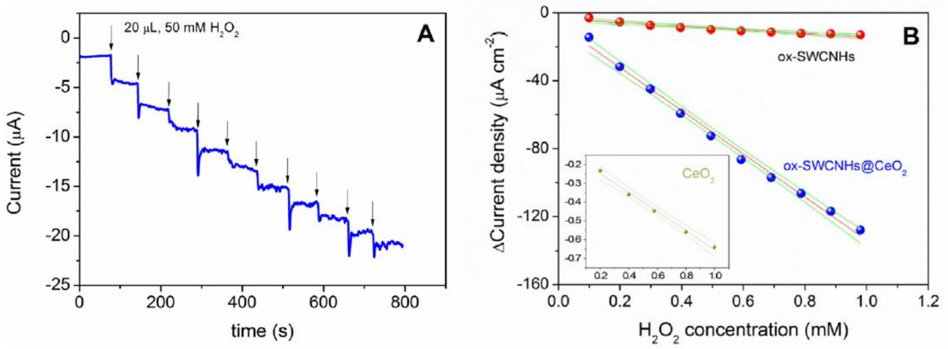

Figure 4.10 A) Amperometric plot for additions of 0.05M H_2O_2 solution using ox-SWCNHs@CeO_2/GCE. Arrows indicate the addition. B) Calibration plots obtained from the amperometric response presented in A with ox-SWCNHs@CeO_2 (●) and from ox-SWCNHs/GCE (●). For clarity, the inset present the calibration plot (on a different current density scale) obtained with CeO_2/GCE. (–) is the linear fit to the data and (–) indicate the 95% confidence bands.

For all the materials, the calibration plots obtained presented a linear relationship between the density of current and the hydrogen peroxide concentration in the concentration range investigated. The average sensitivity measured at -0.2V for the GCE modified with ox-SWCNHs@CeO_2 was 160±20µA cm^{-2} mM^{-1}, higher than the electrodes modified with neat CeO_2 or ox-SWCNHs, for which the average sensitivities were 0.4±0.1µA cm^{-2} mM^{-1} and 20±3µA cm^{-2} mM^{-1} respectively. Thus, the hybridization produced an increase of almost three orders of magnitude with respect to CeO_2 alone and one order of magnitude with respect to free ox-SWCNHs.

The sensitivity obtained for the electrode modified with neat CeO_2 was lower than the data reported in literature by Ujjain et al. They reported the sensing activity of protected CeO_2 nanoparticles had a sensitivity of 20µA cm^{-2} mM^{-1}. (8) The reasons for the lower sensitivity of CeO_2/GCE than the reported system stemmed from the higher amount of CeO_2 used by Ujjain, and the protecting groups used to avoid aggregation of the CeO_2 nanoparticles.

It is also worth noting that the average sensitivity of ox-SWCNHs was higher than the sensitivity of other metal-based materials investigated as H_2O_2 sensors and reported in table 4.1. This finding stemmed from the improved electron transfer at the interface between the nanostructured domains and the H_2O_2 in solution, as also the EIS results and the CV experiments suggested. The sensors based on nanoscaled materials usually suffer from aggregation phenomena, inducing low performances over long experimental time and for several consecutive measurements.

The influence of thermal treatment on sensitivity was also evaluated. Thermal treatment can severely affect the Ce^{3+}/Ce^{4+} ratio and crystallinity of the CeO_2, and it can induce changes in the CeO_2 nanoparticle size. ox-SWCNHs@CeO_2 was kept at 250°C for 5hs under air flow. The effect of the calcination was investigated and compared with the performance of the fresh ox-SWCNHs@CeO_2.

After calcination, the sensitivity towards H_2O_2 decreased to 55±30 µA cm^{-2} mM^{-1}. The reason of this change in sensitivity arose from the decrease of O-Ce^{3+} groups as Chen et al reported. (32) Moreover, the thermal treatment increases the crystallinity of the nano-CeO_2, and the amount of Ce^{4+}. Karakoti et al. reported that CeO_2 could catalyze the H_2O_2 decomposition operated by Ce^{4+} content (33) , as the reactions below show:

$$Ce^{4+} + H_2O_2 \rightarrow \ Ce^{3+} + HOO^{\cdot} + H^+ \quad (1)$$

$$Ce^{4+} + HOO^{\cdot} \rightarrow \ Ce^{3+} + O_2 + H^+ \quad (2)$$

The decrease in sensitivity, thus, stemmed from the increase of Ce^{4+} content, which favored the decomposition of H_2O_2 prior to the electrochemical detection.

In principle, change of performance could presumably be related to changes in the surface area of the final material. To this purpose, N_2 physisorption isotherms were recorded at liquid N_2 temperature over the fresh and the calcined material. Although the pores diameter did not change after the thermal treatment, the surface area increased from 212 m^2 g^{-1} for the fresh sample to 517 m^2 g^{-1} for the calcined sample. The surface area increase was expected, as calcination removed all the organics, however, the sensitivity decrease could not be associated to changes in surface area and pores volume. Hence, it is more likely that following the thermal treatments there is a decrease of polar functionalities concentration, such as –COOH and –OH groups, which are involved in adsorption of polar H_2O_2 molecules.

H_2O_2 can produce several degradation products, including oxygen radicals, which are aggressive towards the catalyst. The stability of ox-SWCNHs@CeO_2/GCE was therefore tested by measuring the sensitivity of calibration plots obtained from amperometric experiments at -0.20 V for 14 consecutive days. ox-SWCNHs@CeO_2 retained the 82% of the average sensitivity after two weeks of continuous experiments, suggesting a high robustness of the present sensor. This data makes ox-SWCNHs@CeO_2 promising for H_2O_2 real sensor development. The loss of ~20% in sensitivity could be attributed to partial detachment of nanomaterial from the GCE surface, calling for an optimization of the deposition techniques, possibly through more advanced casting strategies on the electrode surface. The main loss of sensitivity was recorded after the first experiment, suggesting that the major detachment occurred during the first experiment maybe due to the re-hydration of the electrode after the drying upon the modification of GCE.

The selectivity is an essential parameter to characterize the reliability of a sensor response. The interference of common compounds used in daily commercial products like ascorbic acid (AA), glucose (Glu) and paracetamol (PA) was investigated through amperometric experiments at -0.2V. At a solution 0.2mM H_2O_2 the interfering compounds were added, and the relative current –time profile is reported in figure 4.11.

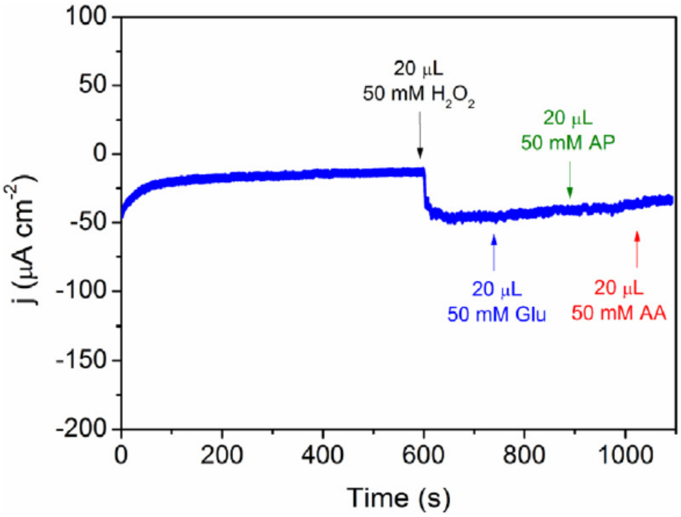

Figure 4.11: Current-time profile at ox-SWCNHs@CeO_2/GCE for one addition of H_2O_2 in order to reach a final concentration of 0.2mM, followed by the same additions of ascorbic acid (AA), glucose (Glu) and acetaminophen (AP).

As shown in Figure 4.11, no current drop occurred upon the addition of the interfering compounds, while the addition of H_2O_2 induced an instantaneous drop of current implying the fast detection of the analyte in the sample. This experiment demonstrates the high selectivity of ox-SWCNHs@CeO_2/GCE towards H_2O_2 detection.

The performance of the catalyst was finally validated in real samples, such as milk and cleaning liquids, where the presence of many additives makes the H_2O_2 detection more challenging.

As mentioned previously, H_2O_2 is widely used both in food factory and daily personal care products manufacturing. H_2O_2 usage in food factory and in particular in milk manufacturing, is important because H_2O_2 inhibits the microbial proliferation and milk spoilage. In the United States, Brasil, and other countries, the addition of H_2O_2 to milk is not allowed, and constitutes a fraud. (34) (35) Milk is a mixture of several compounds, and may interfere on the H_2O_2 detection. Samples made by Italian UHT milk (3.5% fat content), were employed as matrix to investigate the selectivity of ox-SWCNHs@CeO_2 as sensor. The sample matrices were prepared diluting 10 µL of milk in 10 ml of 0.1M TRIS-HCl pH7.4. Known amount H_2O_2 were added, and their recoveries were determined by amperometric measurements. The analysis showed a recovery percentage of 110% with 8% of relative standard deviation. A similar protocol was used for the experiments carried out with cleaning liquids. H_2O_2 is usually employed as bleaching agent and disinfectant in these products. However, H_2O_2 tends to fast decompose to water and oxygen, in spite of the quality of the products. As for the milk case, the several ingredients constituting the cleaning liquid formulation, such as dymethil adipate, dimethyl glutarate, dimethyl succinate, C12-C14 Pareth-X, MEK, poly(oxy- 1,2-ethanediyl), alpha-isotridecyl-omega-hydroxy, C16-18 alcohols and C18 unsaturated alcohol can interfere with the analysis. The cleaning liquid sample was prepared diluting it 625 times with 0.1M TRIS-HCl pH 7.4 and adding known amounts of H_2O_2. The recoverydetermined by amperometric experiments was 109 with 5% of RSD.

The recovery percentage is the sensor response obtained from an amount of the analyte added to the matrix, compared to the sensor response for the true concentration of the pure analyte. The obtained results for the real samples have demonstrated the selectivity and the reliability of the ox-SWCNHs@CeO_2 application to H_2O_2 sensing also in commercial products bearing complex matrices.

4.3.5 Conclusion

As the obtained results have demonstrated, the choice of a hierarchical design for the development of an H_2O_2 sensor emerged as a winning strategy. The conjugation of ox-SWCNHs and CeO_2, has yielded a final nanostructured hybrid with properties better than the two single precursors. The tight contact between the nanocarbon and the nano-CeO_2 phase has been studied and confirmed using several techniques: TGA, Raman, AFM, HR-TEM and EDX mapping.

The sensitivity reached towards the H_2O_2 detection (160±20 µA $cm^{-2}mM^{-1}$), was three orders of magnitude higher than the sensitivity corresponding to neat CeO_2 (0.4±0.1 µA $cm^{-2}mM^{-1}$), suggesting that the application of hierarchical strategy allowed to design and develop an effective sensor using low amounts of nanostructured CeO_2 without the necessity of further protecting groups to avoid CeO_2 aggregation. The use of ox-SWCNHs not only plays an essential role in CeO_2 shell stability, it also drives faster mobility of the electrons from the GCE surface to the nanocatalyst domains, increasing the electron transfer rate towards H_2O_2 analyte molecules. The obtained material exhibits high stablility (82% stability after 2 weeks of continuous use) and reproducibility. Moreover, the test carried out in presence of interfering compounds and in real matrices such as milk and mouthwash liquids confirmed the high selectivity of the ox-SWCNHs@CeO_2, and the good tolerance towards matrix effects. Taking into account the obtained results with the CeO_2, it is possible to consider the employment of this strategy for the development of novel materials based on other metal oxides integrated with SWCNHs, leading to a novel class of commercial sensors for H_2O_2 detection able to compete with the enzyme-based sensors.

4.4 Reference

1. P. Tundo, V. Esposito, *Green Chemical Reaction.* Netherlands : Springer, **2008.**

2. M. S. Quintino, H. Winnishofer, K. Araki, H. E. Toma, L. Agnes, *Analyst,* **2005**, Vol. 130, p. 221-226.

3. C. Reichardt, T. Welton, *Solvents and solvent effect in organic chemistry .* New Jersey, United States : John Wiley & Sons Inc., **2011**.

4. J. R. Stones, S. Yang, *Antioxid. Redox Signal,* **2006**, Vol. 3, p. 243-270.

5. A. L. Hu, Y. H. Liu, H. H. Déng, G. L. Hong, X. H. Xia, W. Chen, *Biosen. Bioelectron,* **2014,** Vol. 61, p. 374-378.

6. Y. B. Tsaplev, *J. Anal. Chem,* **2012**, Vol. 67, p. 506-514.

7. H. A. Khorami, J. F. Botero-Cadavid, P. Wild, N. Dijali, *Electrochimc. Acta,* **2014**, Vol. 115, p. 416-424.

8. S. K. Ujjain, A. Das, G. Srivtava, P. Ahuja, M. Roy, A. Arya, K. Bhargava, N. Sethy, S. K. Singh, R. K. Sharma,M. Das, *Bioinerphases,* **2014**, Vol. 9.

9. Y. Hu, Z. Zhang, C. Yang, *Anal. Chim. Acta,* **2007**, Vol. 601, p. 95-100.

10. A. J. S. Ahammad, *J. Biosens. Bioelectron.,* **2013**, Vol. 9, p. 1-11.

11. E. Shji, M. S. Freund, *J. Am. Che. Soc.,* **2011,** Vol. 123, p. 3383-3384.

12. R. Breslow, *Acc. Chem. Res.,* **1995**, Vol. 28, p. 146-153.

13. W. Chen. S. Cai, Q. Q. Ren, W. Wen, Y. D. Zhao, *Analyst,* **2012**, Vol. 137, p. 49-58.

14. M. Moumene, A. Tabet-Aoul, M. Gouis, D. Rochefort, M. Mohamedi, *Int. Electrochem. Sci.,* **2014**, Vol. 9, p. 176-184.

15. J. Sofia, G. Muralidharan, *Mater. Res. Bull.,* **2015**, Vol. 15, p. 315-320.

16. B. Zhang, X. Zhang, D. Huang, S. Li, H. Yuan, M. Wang, Y. Shen, *Talanta,* **2015**, Vol. 141, p. 73-79.

17. D. Zhang, J. Zhang, R. Zhang, H. Shi, Y. Guo, X. Guo, S. Li, B. Yuan, *Talanta,* **2015**, Vol. 144, p. 1176-1181.

18. L. Shi, X. Niu, T. Liu, H. Zhao, M. Lan, *Microchimica acta,* **2015,** Vol. 182, p. 2485-2493.

19. J. Jaime-Gonzalez, E. Mazario, N. Mendez, J. Sanchez-Marcos, A. Munoz-Bonilla, P. Herrasti, *J. Electrochem. Solid. State,* **2016**, Vol. 20, p. 1191.

20. C. Sun, H. Li, L. Chen, *Energ. Environ. Sci.,* **2012**, Vol. 5, p. 8475-8505.

21. G. Nie, X. Lu, J. Lei, L. Yang, X. Bian, Y. Tong, C. Wan,**.** *Electrochim. Acta,* **2013**, Vol. 99, p. 145-151.

22. P. Jakubec, V. Urbanova, Z. Markova, R. Zboril**,** *Electrochim. Acta,* **2015**, Vol. 153, p. 62-67.

23. X. Chen, G. Wu, Z. Cai, M. Oyama, X. Chen, *Microchim. Acta,* **2014**, Vol. 181, p. 689-705.

24. C. Ray, S. Dutta, A. Roy, R. Shoo, T. Pal**,** *Dalton Transaction,* **2016,** Vol. 45, p. 4780-4790.

25. T. Montini, M. Melchionna, M. Monai, P. Fornasiero, *Chem. Rev.,* **2016**, Vol. 116, p. 5987-6041.

26. A. Trovarelli, P. Fornasiero, *Catalysis by Ceria and related Materials.* s.l. : Imperial College Press, **2013**.

27. R. Guo, Y. Wang, S. Yu, W. Zhu, F. Zheng, W. Liu, D. Zhang, J. Wang, *RSC Adv.,* **2016**, Vol. 6, p. 59939-59945.

28. A. Beltram, M. Melchionna, T. Montini, P. Fornasiero, *Catal. Today,* **2015**, Vol. 253, p. 142-148.

29. M. S. Dresselhaus, A. Jorio, M. Hoffman, G. Dresselhaus, R. Saito, *Nano Lett.,* 2010, p. 751-758.

30. Y. B. Tsaplev, *J. Anal. Chem.,* **2012**, Vol. 67, p. 506-514.

31. A. K. Yagati, T. Lee, J. Min, J. W. Choi, *Biosens. Bioelectron.,* **2013**, Vol. 47, p. 385-390.

32. J. C. Chen, W. Chen, Y. T. Tien, C. J. Shih, *J. Alloy Compd.,* **2010**, Vol. 496, p. 364-369.

33. A. Karakoti, S. Singh, J. M. Dowding, S. Sealac, W. T. Self, *Chem. Soc. rev,* **2010**, Vol. 39, p. 4422-4432.

34. http://www.accessdata.fda.gov/scripts/cdrh/. [Online] US Food and Drug Administration, Code of Federal rRegulation 21,3, cite:21CFR184.1366.

35. R.A.B. Silva, R.H.O. Montes, E.M. Richter, R.A.A. Munoz, ***Food Chem.,*** 2013, Vol. 133, p. 200.

36. http://www.cosmeticsinfo.org/ingredient/hydrogen-peroxide-0. *Cosmeticsinfo.org.* [Online]

Chapter 5
Conclusions

During this research project, hybrid materials based on carbon nanostructures have been synthesized using a hierarchical approach. The prepared multicomposites-multifunctional materials have been used as electrocatalysts in energy and sensing related preocesses. In order to gain information about their morphology and interaction between each component, a combination of macroscopic and microscopic techniques including TEM, HR-TEM, -EDX, STEM, AFM, TGA , FTIR, and Raman spectroscopy have been carried out.

Moreover, for each nano-material a systematic electrochemical characterization has been conducted, unravelling the redox properties and the relative electrocatalytic properties of the nanocatalysts. The work targeted three specific catalytic processes: O_2 reduction reaction (ORR) and CO_2 reduction reaction (CO_2RR) related to energy applications, and H_2O_2 reduction related to sensing applications.

1)CO_2RR arose great interest during the last decades due the possibility to employ CO_2, side product of fossil fuels use, as cheap carbon source for the manufacturing of high value products.

Two catalytic systems were prepared and screened as CO_2 reduction electrocatalysts: Pd@TiO_2/ox-SWCNHs and NiCyclam@BMIM/p-SWCNHs. The former comprises Pd@TiO_2 core-shells nanoparticles linked to ox-SWCNHs through a sol-gel method. This system has shown good selectivity towards the conversion of CO_2 to $HCOO^-$ at very small overpotentials (applied potentials as low as -0.05 vs RHE) with FE as high as 40% when operating in 0.50 M $NaClO_4$. These conditions were optimized studying the catalytic properties in other electrolytes such as PBS and $NaHCO_3$. The FE decrease over time evidences the presence of deactivation pathways. Such deactivation may be explained in several terms, such as an adsorption of reaction intermediates onto specific catalytic sites or the successive decomposition of the as formed formate. However, comprehensive experimental proofs are still being established. Notably, the deactivation is only temporary and the catalytic properties can be restored, as recycling tests have demonstrated.

NiCyclam@BMIM/p-SWCNHs was obtained exploiting the dispersive forces acting between the ionic liquid and the carbon nanostructure, creating a supported ionic liquid phase (SILP). The well-known molecular catalyst NiCyclam has been successfully entrapped within the ionic liquid layer, providing an interesting example of heterogenized electrocatalyst for the reduction of CO_2 in aqueous medium. Using CV the redox properties of NiCyclam have been evaluated confirming that the catalyst were still electroactive after the confinement. In particular the surface concentration of NiCyclam reached was 2.7×10^{-7} mol/cm^2, which was higher than the values till now reported in literature. Catalytic tests have demonstrated that the catalyst retains its catalytic activity towards the conversion of CO_2 to CO with a FE reaching 50% after 1 h of bulk electrolysis.

2) ORR is a multi-electron reduction reaction, as mentioned in Chapter 3 it generally leads to formation of H_2O_2 or H_2O (generally their mixtures). This process is strictly associated to the development of fuel cells and, in case of H_2O_2, industrial manufacturing. The ORR investigations were based on the utilization of two catalytic materials, t-Fe@MWCNTs and g-N-CNHs.

t-Fe@MWCNTs was achieved by covalent functionalization of the precursor Fe@MWCNTs with benzoic acid groups. The Fe-filled MWCNTs precursor was supplied by Prof. Bonifazi's group. Using macroscopic techniques and microscopic techniques the endohedral confinement of Fe inside the MWCNTs was confirmed and the outer walls' functionalization was displayed. In particular the amount of Fe confined in the tubes figured 27% by TGA analysis. Electrochemical characterization by means of CV reveals the availability of Fe to engage redox reactions, implying the role of the CNTs as electron mediator between the electrode surface and the confined Fe. CV experiments also highlighted that the organic functionalization on the outer wall did not affect the redox behavior of Fe. t-Fe@MWCNTs was effective as ORR electrocatalyst at neutral pH, enabling the conversion of O_2 to H_2O with higher current (0.99 mA) than the reference materials and triggering the process at lower potential (0.25 V). Furthermore, electrochemical impedance spectroscopy (EIS) demonstrates that the organic functionalization of the outer wall of the MWCNTs can positively influence the ORR catalysis facilitating the absorption of oxygen onto the tubes and allowing a more efficient inter-wall electron trafficking thanks to the as introduced defects.

g-N-CNHs was supplied by the Dott. Daniel Isperilla-Iglesias consist of SWCNHs enveloped into an N-doped graphitic shell. The catalytic properties of g-N-CNHs towards O_2 reduction have been evaluated at three different pH, 1, 7.4 and13. The electrocatalyst has demonstrated high selectivity toward H_2O_2 evolution over all the pH range, exerting the process at very positive potentials and with high efficiency: 95% pH1, 90% pH7.4 and 63% pH13. Moreover, the stability over long time experiment has been evaluated collecting the current-time profile over 24hours of electrolysis experiment at fixed potential, displaying a very good stability.

3) The detection of H_2O_2 has an important role either in daily used products quality control, than for clinical applications. A novel sensor made by the hybrid ox-SWCNHs@CeO_2 has been synthetized and characterized. The amperometric sensor obtained using ox-SWCNHs@CeO_2, demonstrated higher sensitivity (160±20 $\mu A\ cm^{-2} mM^{-1}$) than its relative reference materials, in particular three orders of magnitude bigger than the sensitivity corresponding to neat CeO_2 (0.4±0.1 $\mu A\ cm^{-2} mM^{-1}$).

By consecutive measurements carried out on a period of 14 days, the robustness could be positively assessed. Common H_2O_2 interferents in several products such as ascorbic acid, glucose and paracetamol did not affect the sensing ability of the catalyst toward H_2O_2, highlighting its selectivity. ox-SWCNHs/CeO_2 has been also successfully employed for the detection of H_2O_2 in real samples, such as milk and washing mouth liquids, confirming the high selectivity towards H_2O_2also in highly complex matrices made by several ingredients.

A common evaluation that can be proposed from the results obtained by this work is that the employment of carbon nanostructures for the development of hierarchical electrocatalytic systems bring great advantages due to the improved electronic communication between each component. This research may be of inspiration for the design of new nanomaterials for energy related applications and sensing.

Appendix A: Review of the experimental methods used and experimental procedures

A1. Electrochemical techniques.

Electrochemical techniques such as Cyclic Voltammetry (CV), Linear sweep Voltammetry (LSV), Chrono-amperometry (CA) and Impedance Electrochemical Spectroscopy (EIS) in particular have been extensively applied for the characterization and the investigation of the catalytic properties of the nanomaterials reported in this thesis.

A.1.1 Set-up of the electrochemical cell used

The set-up cell used for the experiment was a three-electrodes cell assembly: working electrode (WE), counter electrode (CE), reference electrode (RE). A gas-tight cell has been employed for the experiment of bulk electrocatalysis.
WE was a glassy carbon electrode modified by drop casting with the studied material, CE was a Pt electrode and RE was an Ag/AgCl electrode.

A.1.1 WE preparation

Here the procedure used to assembly the modified GCE electrodes using the materials presented in this thesis are reported.
Glassy carbon electrode before the modification has been polished using 1 µm alumina slurry for 1 minute, 0.3 µm alumina slurry for 1 minute and washed with milliQ water. The alumina residue has been removed sonicating the GCE 30 seconds in milliQ water.

A.1.1.1. Electrode modified with Pd@TiO_2/ox-SWCNHs

The working electrodes here used, after polish treatment were modified using a 20µL drop of 3mg ml^{-1} suspension of **Pd@TiO2/ox-SWCNHs**. The suspension was prepared sonicating the material powder in 1:0.9:0.02 H_2O:EtOH:Nafion (2.5% vol in EtOH) solution for 1.5h.
For the bulk electrolysis experiments, the electrode were prepared by drop casting of 4 drop 50µl each one (two for side) on Toray paper.

A.1.1.2. Electrode modified with NiCyclam@BMIM/p-SWCNHs

The working electrodes here used, after polish treatment were modified using a 20µL drop of 5 mg ml^{-1} suspension of **NiCyclam@BMIM/p-SWCNHs**. The suspension was prepared sonicating the material powder in 1:0.9:0.02 H_2O:EtOH:Nafion (2.5% vol in EtOH) solution for 1.5h.
For the bulk electrolysis experiments, the electrode were prepared by drop casting of 2 drop 100µl each one (two for side) on slide (0.8 cm x 1 cm) of glassy carbon plates.

A.1.1.3. Electrode modified with t-Fe@MWCNTs

The working electrodes here used, after polish treatment were modified using a 30µL drop of 3mg ml^{-1} suspension of **t-FeMWCNTs**. The suspension was prepared sonicating the material powder in 1:0.9:0.02 H_2O:EtOH:Nafion (2.5% vol in EtOH) solution for 1.5h. Subsequently, the dispersion was centrifuged at 500 rpm for 6 min to remove residual bundles remaining in solution.

A.1.1.4. Electrode modified with g-N-CNHs

The working electrodes used, after a polishing protocol, were modified with a 10µL drop of 2mg ml^{-1} dispersion of **g-N-CNHs**. The dispersion was prepared sonicating the material powder in milliQ water for 1.5h.
For the bulk electrolysis experiments, the electrode were prepared by drop casting of 2 drop 100µl each one (two for side) on slide (0.8 cm x 1 cm) of glassy carbon plates.

A.1.1.5 Electrode modified with ox-SWCNHs@CeO$_2$

The working electrodes here used, after polish treatment were modified using a 10µL drop of 2.5mg ml^{-1} suspension of **ox-SWCNHs@CeO$_2$**. The suspension was prepared sonicating the material powder in 50:50 H_2O: EtOH solution for 30 mins.

A.1.2. Linear Sweep Voltammetry

Linear sweep voltammetry (LSV) has been used coupled with rotating disk electrode experiment and for the characterization of CO_2 activation using NiCylam@BMIM/p-SWCNHs, in chapter 3.
LSV is a potential sweep technique, in which the current at the WE is collected in the screened potential range varying the potential linearly with the time using the desired scan rate *v*, depending of the designed experiment. Below figure A.1 reports the potential-time profile and its relative current-potential profile.

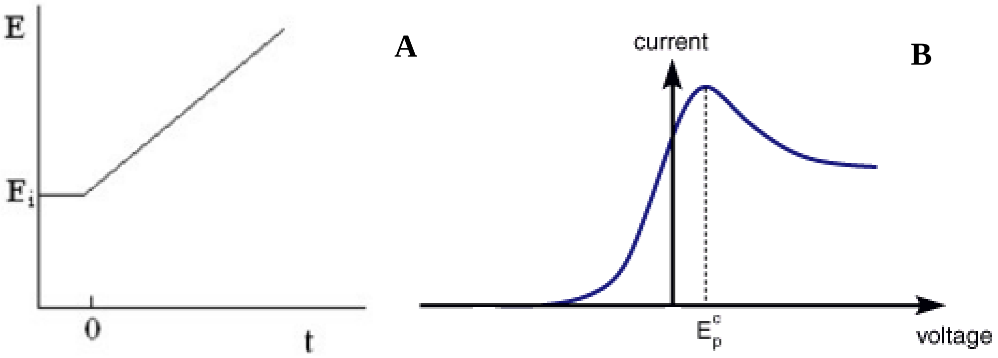

Figure A.1. A) LSV potential-time profile. B) LSV recorded signal, current-potential profile.

Changing *v*, the current potential profile changes. Decreasing *v* the time taken to scan the investigated potential range is longer and the diffusion layer become big. Consequently, the mass flux to the electrode surface is smaller when the scan rates is small, thus, the current will be lower because it is proportional to the flux. When v is higher, the current is higher.

A.1.3 Cyclic Voltammetry

Cyclic Voltammetry (CV) has been employed for each material to characterize their redox behavior.
As well as LSV, CV is a potential sweep technique. As LSV, the current evolved generated at the working electrode is collected scanning the potential range studied using the desired scan rate, depending on the designed experiment. However, the potential varied through a triangular impulse. Considering the potential range from V1 to V2, the potential is swept first from V1 to V2, and then from V1 to V2. Figure A.2. reports the potential-time profile and the relative signal recorded.

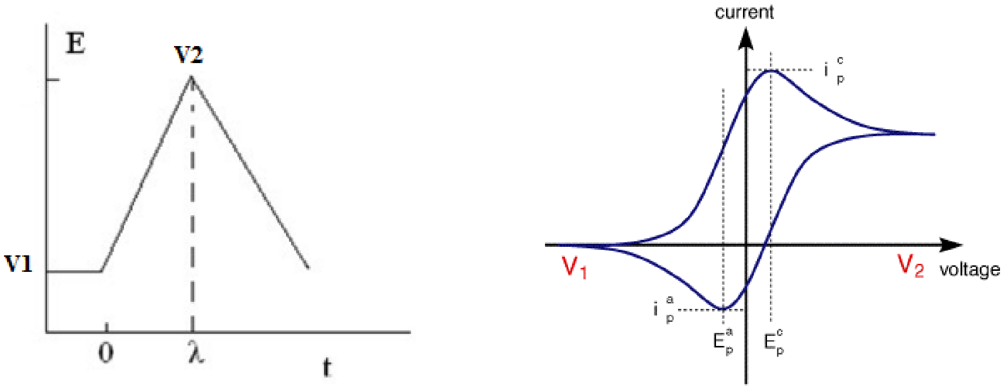

Figure A.2. A) CV potential-time profile. B) CV recorded signal, current-potential profile.

CV is very sensitive towards low concentration of the ionic species in solution, and is a non-destructive, fast and ease method for the characterization of the redox behavior of molecules and materials. Looking Figure A.2 B), going from V1 to V2, following the oxidation sweep, the current increases approaching E_{pa}, at this potential the oxidation process is limited by diffusion of the substrate to the electrode surface. After E_{pa}, the current decrease due to the depletion of the substrate concentration at the electrode surface. The reduction sweep from V2 to V1, can be discussed in the same way. The redox process reported in figure A.2, is relative to a reversible system. In a reversible system the product of the oxidation, underwent reduction, and the ratio of the current peaks, (i_{pa}/i_{pc}) is 1.

A.1.4 Impedance electrochemical spectroscopy

In order to gain further insight about the redox behavior, Electrochemical Impedance Spectroscopy (EIS).
EIS provides information about the resistive and capacitive properties of materials as response to a perturbation of the system caused by a small alternate current (AC) sinusoidal excitation signal. Collecting the impedance value varying the perturbation frequency, the Nyquist plot and the Bode plot can be obtained. By the elaboration of the Nyquist plot the equivalent circuit can be deduced, from which resistive and capacitive parameters can be calculated.

A.1.4.1 Basic Knowledges

Impedance is defined as the opposition to AC flow in a complex system. If the system is purely resistive, the impedance is correspondent to the resistance calculate as the ohm law:

$$R = \frac{V}{I}$$

Where R is the resistance, V is the potential and I is the current.
However, a pure resistive material is ideal, and a modified Ohm Law is used to calculate the impedance:

$$Z = \frac{V\,(t)}{I(t)} = \frac{V_0\cos(\omega t)}{I_0\cos(\omega t - \phi)} = Z_0\frac{\cos(\omega t)}{\cos(\omega t - \phi)}$$

where Z is the impedance, t is the time, ω is the radial frequency and ϕ is phase shift. Z has a real component and an imaginary component, as the following equation reports:

$$Z = \frac{V}{I} = Z_0\exp(j\phi) = Z_0\exp(cos\phi - j\sin\phi)$$

Using this equation the Nyquist plot can be obtained, where the imaginary component of the impedance is plotted in function of the real component. In figure A.3 a Nyquist plot example is reported.

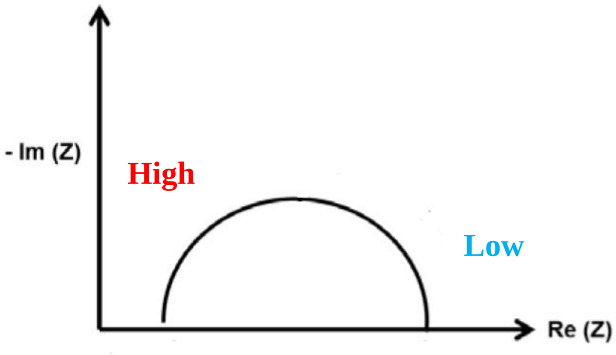

Figure A.3 Representation of Nyquist plot.

Each point of the Nyquist plot is the impedance collected at a specific frequency. Two different region can be distinguished in the Nyquist plot, the right side of the graph is the low frequency side, and the left side is the high frequency side. The diffusion transport of the redox species to the electrode surface plays an important role. At high frequencies, the effect of the diffusion transport is smaller than at low frequencies.

A.1.4.2 Equivalent circuits

The equivalent circuit used to fit the EIS data, is composed by three fundamental elements: the resistive element (R), the capacitive element (C), and the inductive element (L).
In an electrochemical cell can be considered resistive element the solution resistance, and the resistance to the charge-transfer at the electrode surface.
The solution resistance defined by the following equation, is dependent by the ionic concentration of the solution and geometric area of the electrode.

$$R_s = \rho \frac{l}{A}$$

where ρ is the solution resistivity , l is the length carrying a uniform current and A is the geometric area of the electrode surface.

The resistance to the charge transfer is dependent by the exchange current and the number of the electrons involved, it can be calculated using the equation reported below:

$$R_{CT} = \frac{RT}{nFi_0}$$

where R is the gas constant, T is the temperature, n is the number of the electrons involved, F is the Faraday constant and i_0 is the current density.

The electrical double layer is characterized by capacitive elements and inductive elements which represent charge-space separation regions. Other elements can take part to the circuit: the constant phase element (CPE) and the Warburg element (Z_w). The Warburg elements is used to represent the diffusion and mass transport effect on the impedance. It is calculated as reported below:

$$Z_w = \sigma(\omega)^{-1/2}(1-j)$$

CPE derives from a capacitor which has a non-ideal behavior.

In the table A.1. the common circuit elements are reported and their current versus potential relationship, and their impedance.

Circuit element	Relationship	Impedance
R	$V = IR$	$Z_R = R$
C	$I = C\frac{dV}{dt}$	$Z_C = \frac{1}{j\omega C} = -\frac{1}{\omega C}$
L	$V = L\frac{dI}{dt}$	$Z_L = j\omega L$

Table A.1: List of the common circuit elements.

A1.4.3 Data elaboration

As mentioned above, EIS data are represented by Nyquist plot and Bode plot. The Nyquist plot relates the imaginary component of Z to the real component and the relation of the impedance by the frequency is implicit. The Bode plot reports the dependence of the impedance by the frequency. The Nyquist plot can contain more than one semicircle, the shape of the semicircle defines the physical characteristics of the investigated system.

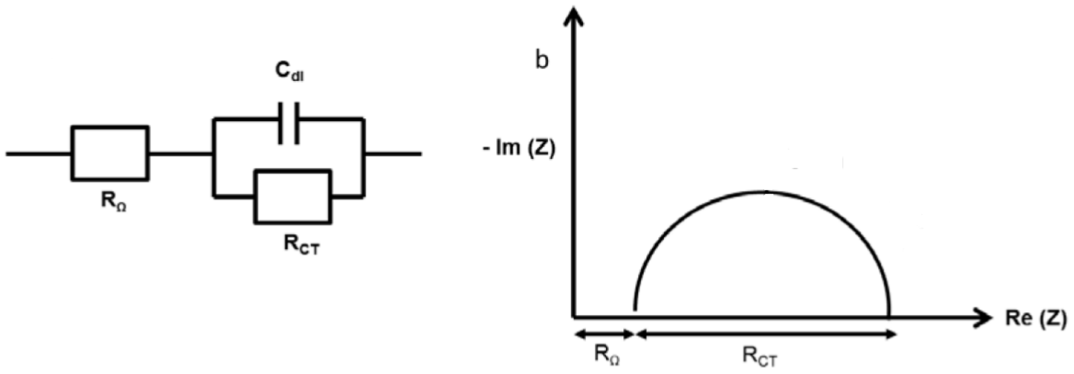

Figure A.4 Representation of the Randles model circuit and the relative Nyquist plot.

For the simplest equivalent circuit, the Randles circuit, the Nyquist is reported in figure A.4. The circuit is made by a resistive element associated to the solution resistance in series with a capacitive and a further resistive element representing respectively the double layer capacitance and the charge transfer resistance. The solution resistance is determined by the x-intercept of the semicircle on the left side of the plots. The diameter of the semicircle is the charge transfer resistance. Bode plot, is a powerful tool when more than one charge transfer resistance at high frequency are presented.

A1.5 Rotating disk electrode technique (RDE)

Rotating Disk Electrode (RDE) method have been employed to characterize ORR. In particular by means of this technique the number of the electrons involved in the ORR process has been calculated and further information on the kinetic feature of ORR catalyzed by Fe@MWCNTs and g-N-CNHs has been gained.
RDE theory, was developed by Benjamin Levich in the XX century.
RDE is a hydrodynamic working electrode. It is attached to an electric motor that can fine regulate the rotation rate of the electrode. During the experiment, LSV is carried out at slow scan rate (usually 0.005 V s^{-1}) under forced convection condition. The rotation generates a laminar flow, which assures a constant flow of fresh solution from the bulk solution to the electrode surface. The bulk solution far from the electrode surface remains well-stirred, meanwhile the solution closer to the electrode rotate with it. If the rotating electrode is taken as reference system the solution near the electrode appears stagnant. This condition is known as hydrodynamic boundary layer. The mass transport from bulk solution to the stagnant layer of solution close to the electrode surface occurs by convenction, due to the stirring action of the electrode rotation. When an ionic species or a molecule enters the hydrodynamic layer which is stagnant, the mass transport is dominated by diffusion. The first mathematical treatment of convection and diffusion towards a rotating disk electrode was proposed by Levich. The equation is reported below:

$$i_L = 0.062nFA(D_o)^{2/3}v^{-1/6}C_0\omega^{-1/2}$$

Where i_L is the limiting current observed at the rotating electrode, $C_0$is the concentration of the bulk solution, n is the number of the electrons, A is the electrode geometric area, $D_o$is the diffusion coefficient, ν is the viscosity kinematic coefficient, F is the Faraday constant and ω is the rotation speed of the rotating electrode. This relation is useful when the reaction studied is a reversible process not complicated by sluggish electron transfer kinetic or chemical reaction coupled to the redox reaction. In this case the LSV collected will have a sigmoidal shape regardless the rotation rate and the limiting current linearly increases as ω increases.

When the electron transfer kinetic of the studied reaction exhibits a sluggish kinetic, the LSVs have no more a regular sigmoidal shape, the equation formulated by Levich, is substituted by the Koutecky-Levich equation:

$$\frac{1}{i} = \frac{1}{i_k} + \frac{1}{0.062nFA(D_o)^{2/3}v^{-1/6}C_0}\omega^{1/2} = \frac{1}{i_k} + \frac{1}{B}\omega^{-1/2}$$

In K-L equation a new term *i_k* appears, named kinetic current. i_k would be the current observed in absence of mass transport limitation.

A.1.5.1 experimental procedure for the determination of the number of electrons involved in ORR

The glassy carbon disk of the RDE was modified by drop casting with 5 µL of the material suspension.

During a RDE experiment, several LSVs are collected in O_2 saturated solution, varying the rotation rate, from the lowest to the fastest. The scan rate of LSV, 0.005 V s^{-1}. The K-L plot can be obtained plotting the limiting current values (plateau current) against the square root of rotation rate. When the limiting current is reached, the reaction is not affected by kinetic limitation. The current is limited only by the mass transport. In figure A.5 a) is reported graph with several LSV collected at different ω, and in b) the relative K-L plot.

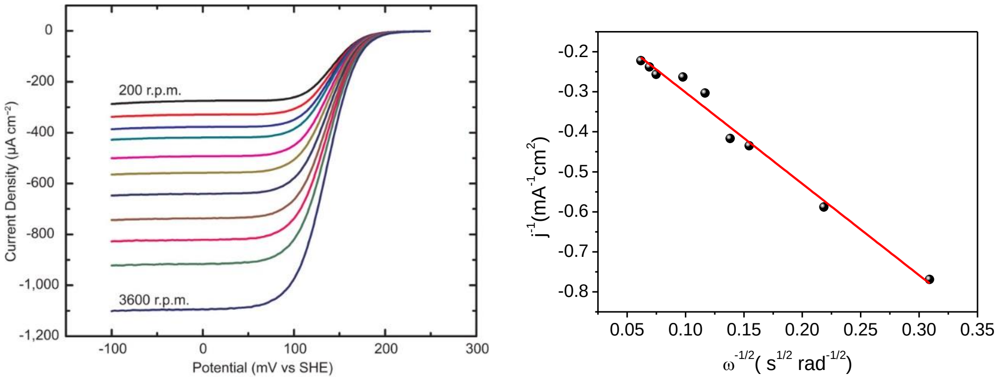

Figure A.5 a) LSVs collected at different ω, and in b) the relative K-L plot.

Using the K-L plots, obtained as explain above, and the K-L equation, the number of electrons involved in the O_2 reduction process have been calculated. The slope of the curve obtained fitting the reciprocal of the current density (j-1) and the reciprocal of the square root of ω correspond to the slope 1/B.

A.1.5.2 experimental procedure for Tafel plot calculation

Tafel plot have been calculated using RDE method. The electrode was prepared as mentioned in the section above. LSV at 0.005 Vs^{-1} have been performed using high rotation rate (bigger than 1600 rpm) in N_2 saturated solution and in O_2 or CO_2 saturated solution.

The LSV collected in N_2 is subtracted from the LSV collected in CO_2 or O_2 saturated solution.

Thus, after log(i) calculation, the Tafel plot is obtained reporting in graph E vs (RHE) in function of log(i).

A.1.6 Chronoamperometry

Chronoamperometry (CA) has been applied to characterize products deriving by the processes (CO_2RR and ORR) and the stability of the electrocatalysts investigated in this thesis.

In CA experiment, a potential value is fixed and the current response is followed during the experimental time. The products evolved by imposing the chosen potential can be analyzed and the yield of the redox reaction can be evaluated. The yield, called faradaic efficiency (FE%) is the ratio between the charge due to the product formation (Q_p) and the total charge flow (Q_{tot}), the mathematical formulation is reported below:

$$FE\% = \frac{Q_P}{Q_{\ tot}}$$

Where:

$$Q_P = n \times F \times mol_P$$

n is the number of electrons involved in the product formation, *F* is the faraday constant (96485 C mol^{-1}) and mol_P is the moles of product evolved during the experiment.

$$Q_{tot} = \int_0^t i\ dt$$

This technique have been employed for the electroactive surface area calculation.

A.1.6.1 EASA calculation

The electroactive surface area (EASA) of the catalyst has been measured using the Hydroquinone (HQ) as redox probe. Using the modified electrode as WE a CV from -0.5V to 1V vs Ag/AgCl has been collected in 0.5mM of HQ in 0.1M PBS. After that, the peak potential of the oxidation peak has been fixed as working potential for a chrono-amperometry experiment long 20 seconds. This is the time necessary to allow the formation of a monomolecular layer of HQ onto the modified GCE electrode. By the integration of the current-time profile obtained by CA experiment the charge (Q) is obtained. Q is plotted in function of the square root of the time, fitting Q in function of $t^{1/2}$, using the slope of the linear fit and the Cottrel equation, the EASA can be calculated.

$$i = \frac{nF\ EASA\ C_0 D^{1/2}}{(\pi t)^{1/2}}$$

Knowing that i=Q/t, it follows:

$$\frac{Q}{t} = \frac{n\,FA\,C_0 D_0^{1/2}}{\pi^{1/2} t^{1/2}}$$
$$\frac{Qt^{1/2}}{t} = \frac{n\,FA\,C_0 D_0^{1/2}}{\pi^{1/2}}$$
$$\frac{Q}{t^{1/2}} = \frac{n\,FA\,C_0 D_0^{1/2}}{\pi^{1/2}}$$
Since $\frac{Q}{t^{1/2}}$ is the slope calculated by the linear fit of Q vs $t^{1/2}$, it is named B, and it follows:
$$EASA = \frac{\pi^{1/2} B}{nF C_0 D_0^{1/2}}$$

Where *n* is the number of involved electron, F is the faradaic constant 96485C mol^{-1}, EASA is the electroactive area, C is the concentration of HQ in mol cm^{-3}; D is the diffusion coefficient $0.8x10^5$ cm^2 s^{-1}, t is the time and π is pi-greek.

A.2 Thermogravimetric Analysis

Thermogravimetric Analysis (TGA) has been used as investigation tool to quantify the amount of functional groups and metal oxides attached onto the carbon nanostructure surface upon the functionalization.

TGA based on the thermal stability of the sample, the information acquired are percentage of weight loss and temperature at which the material components decompose. Each loss in weight in a composite material (as the materials investigated) can be associated to a material component.

During TGA experiment, the change in weight of the sample is monitored as function of the increasing temperature. TGA can be carried out using inert atmosphere (N_2 or Ar flow) or using an oxygen atmosphere. The choice of the atmosphere depends on the material nature. An inert atmosphere is choice when a totally organic material, like a carbon nanostructure functionalized with oraganic moieties, is analyzed. The amount of organic moieties binding the carbon nanostructure can be measured.

TGA operated using oxygen flow is performed when the presence of metals is evaluated. The metal in the sample is converted into the correspondent oxide, and it is associated to the residual weight at the end of the run.

The sensitivity of the technique depends on the precision of the balance and the power supply providing the temperature ramp of the furnace.

The analysis procedure adopted in this thesis is the same for all the samples. An equilibration step followed by the linear temperature ramp. The equilibration step at 100 °C for 20 minutes allow the removal of adsorbed water molecules on the sample. The data collection start simultaneously with the beginning of the linear temperature ramp. The temperature is ramped as 10°C min^{-1}.

A.3 Raman Spectroscopy

Raman spectroscopy is a powerful tool when carbon nanostructure materials are investigated. This technique was employed to characterize all the materials investigated in this thesis.
Raman spectroscopy, is a non-linear spectroscopic technique and based on the inelastic scattering of monochromatic light.
When a monochromatic light, usually a laser beam hits a sample, a light portion is elastically scattered and another portion is inelastically scattered. The elastic scattering, called Rayleigh scattering, it is associated to collision between photon and molecules occurring without energy change, meanwhile the inelastic scattering, called Raman scattering, corresponds to collision between photon and molecules occurring with energy change. Two types of Raman scattering can be distinguish: the Stokes scattering associated to high frequency scattered photon deriving from an energy transfer from the photon to the molecule; and Anti-Stokes scattering, associated to low frequency scattered photon deriving from an energy transfer from the molecule to the photon. The probability to observe a Stokes scattering is higher then the other scattering because at room temperature the molecules population is essentially in its ground-state level.

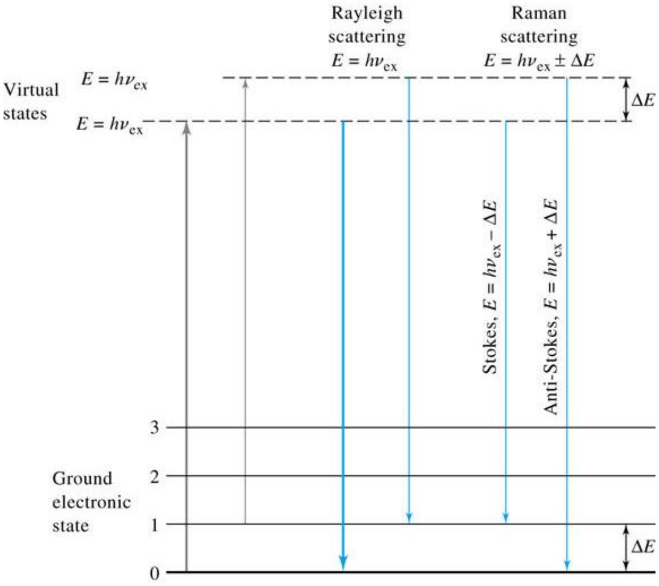

Figure A.6 Schematic rapres.entation of Rayleigh and Raman scattering(Anti-Stokes and Stokes level)

In Raman spectroscopy the spectra collected is reported using the Raman shifts ($\Delta\nu$):

$$\Delta\nu = \nu - \nu_m$$

where ν is the wavenumber (cm^{-1}) of the incident light, and $\nu_m$is the wavenumber (cm^{-1}) of the energy transition between the lowest and first excited vibration energy level.
Generally, a Raman spectroscopy instrument is made by monochromatic laser source, monochromator, filters which allow the detection at very low ($\Delta\nu$), and a detector that usually is a charge coupled detector (CCD).
Graphene based materials such as CNTs or SWCNHs have characteristic Raman bands, which allow to gain semi-quantitative information on the functionalization of the

carbon nanostructure surface. Mainly, the characterization is performed evaluating the presence of the bands called band D and band G.

The band D, called disorder band, occurs 1350 cm^{-1} and it is associated to the presence of sp^3 carbon atoms in the carbon nanostructure. D band can be generated by a second order scattering, in particular to a two photon scattering, or one-phonon and one elastic scattering event. It may stem from decreasing of symmetry due to defects like pentagon rings, typical of CNT caps and SWCNHs tips or introduced by covalently linked functional groups, presence of carbon nanoparticle or amorphous carbon. The intensity of this band depends on the size of graphite microcrystals and the order of the sample

G band, where G indicates graphite, occurs at 1580 cm^{-1}, is associated to a first order transition, generated by a phonon emission. In general, it is the more intense band, and is related to the conductive property of the materials.

The ratio I_D/I_G can be used as tool to gain information about the carbon nanostructure functionalization. Comparing the I_D/I_G of a functionalized materials with the I_G/I_D ratio of the relative pristine is possible evaluate if the functionalization treatment successfully occurred.

A.4 Fourier Transform Infrared Spectroscopy

FT-IR has been used to characterize the occurrence of the material functionalization.

FT-IR spectroscopy is a linear spectroscopic technique, mainly applied for qualitative characterization. It based on the interaction between the sample and IR radiation. The interaction between IR and molecules excites vibrational transitions, associated to a dipolar moment variation. The absorption band stemming by IR radiation absorption are associated to stretching mode and bending movements of atoms sharing a bond. The stretching modes occur at frequencies higher than bending modes. In general the bonds, where one of the atoms is H, have higher frequencies due to the small mass of H. Each bond has a characteristic frequency, which depend by the mass of the atoms and the force constant as reported by the Hooke law:

$$\overline{\nu} = \frac{1}{2\pi c}\sqrt{\frac{K}{\mu}}$$

Where K is the force constant, μ is the reduced mass, π is the pi-greek and c is the rate of the light. The reduced mass is calculated as:

$$\mu = \frac{m_1 \times m_2}{m_1 + m_2}$$

Where m_1 is the mass of the atom 1 and m_2 is the mass of the atom 2.

Consequently, the vibrational mode of a functional group has the own specific frequency. Thus, the functionalization of the carbon nanostructure can be followed by IR, evaluating the appearance of bands associated to the new bonds introduced on the carbon nanostructure. The organic functionalization bands occur in the high frequency region, meanwhile functionalization with metal oxide induce the appearance of broad bands associated to the stretching of the bond between metal atom and oxygen in the low-frequency region, due to the big mass of the metals atoms. The samples for FT-IR spectra have been prepared producing a pills with a little amount of material and KBr.

A.5 Transmission Electron Microscopy

Transmission Electron microscopy (TEM) has been used as tool to evaluate the morphological feature of each material presented in this thesis.

The electron microscope operates under vacuum. The main part of an electron microscope is the column in which the electron gun is placed, the acceleration field and the condensed and magnetic filters, which control the size of the beam. The pictures obtained by the microscope are the results of the elaboration of several type of signals generated by the interaction between the electrons and the matter.

In this thesis, TEM and High resolution-TEM (HR-TEM) have been employed. The specimens were prepared depositing the samples on grids made from a metallic framework and covered with a carbon film. The electrons diffracted after the passage through the specimen are focused by electromagnetic objective lens in the image plane. The HR-TEM allows the detection of differences in phase of the scattered electrons, permitting to highlight nanosized structure such as nanoparticles. HR-TEM allows to perform of Energy Dispersive X-Ray (EDX) analysis, widely used for the further characterization of the hybrids. EDX analysis, enables to gain deeper information about the sample morphology through the elements recognition, and in this thesis has been a powerful tool to investigate on the interface between the components of the hierarchical materials investigated. The elements recognition is ascribed to the X-rays generated by the interaction of the electron beams and the sample, which have characteristic energies for each element.

A6. Atom Force Microscopy

Atom Force Microscopy, have been employed for the morphology characterization of ox-SWCNHs@CeO_2.

AFM analysis is a scanning probe microscopy technique, based on the revelation of forces such as Pauli, Van der Waals or electrostatic between a small tip and the sample. The AFM uses as the probe a sharp tip, placed at the end of cantilever. The laser beam is focused on the back of the cantilever. The reflective laser beam is detected by a four quadrant Position Sensitive Photo Diode (PSPD), which enables to track the laser spot movement while the tip is scanning the sample surface. By means of Hook laws and geometric calculation about the laser movements tracked by the PSPD, information about the interaction occurring between the tips and the sample can be obtained.

A feedback system, over the PSPD, controls the tip-sample interactions, using a fixed set-point during the measurement. The set-point can be measured by two different mode: using a contact mode, based on the cantilever deflection, or the non-contact mode based on the variation of resonance frequency and amplitude at a specific frequency.

The sample of ox-SWCNHs@CeO_2 was prepared by drop casting of a diluted suspension of ox-SWCNHs@CeO_2 in EtOH on a piece of slide of mica foil.

A7. N_2 physisorption analysis

N_2 physisorption analysis is a powerful tool for the characterization of materials surface. Using N_2 physisorption information about properties such as porosity, strength, hardness, permeability, separation selectivity.
Brunauer, Emmett and Teller theory (BET) provides a mathematical model for the process of gas sorption. BET is an extension of the Langmuir theory, because it assume that the gas adsorbed is a molecular monolayer. The physisorption of gas onto a material results by weak interaction such as Van der Waals,
By a physisorption experiment, N_2, is physical adsorbed over the entire surface material exposed, filling also the pores. Estimating the amount of nitrogen adsorbed related in relationship with its pressure, under normal atmospheric pressure and at the boiling point of the liquid N2, the specific surface area can be calculated. The mathematical expression of the BET theory is reported below:

$$\frac{1}{v\left[(p_0/p)-1\right]} = \frac{c-1}{v_{\mathrm{m}}c}\left(\frac{p}{p_0}\right) + \frac{1}{v_m c}$$

Where ***p*** and ***p₀*** are the equilibrium pressure and the saturation pressure of the adsorbates, ***v*** is the amount of gas adsorbed, $\boldsymbol{v_m}$ is the monolayer adsorbed gas quantity, and ***c*** is called BET constant, calculated as reported below:

$$c = \exp\left(\frac{E_1 - E_{\mathrm{L}}}{RT}\right)$$

Where $\mathbf{E_1}$ and $\mathbf{E_L}$ are associated to the heat of adsorption for the first layer of adsorbate and liquefaction heat respectively. The specific area is obtained plotting $\boldsymbol{1/v[(p_0/p)-1]}$ in function of $(\boldsymbol{p_0/p})$, which is called BET plot. The relation between them is linear in the range 0.05< $(\boldsymbol{p_0/p})$>0.35. By the slope and the intercept, $\boldsymbol{v_m}$ and ***c*** values can be calculated. Then the total surface and the specific surface area can be calculated using the following equation:

$$S_{\mathrm{total}} = \frac{(v_{\mathrm{m}}Ns)}{V}$$

$$S_{\mathrm{BET}} = \frac{S_{\mathrm{total}}}{a}$$

Where ***N*** is the Avogadro number, ***s*** is the adsorption cross section, ***V*** is molar volume of the adsorbate gas, ***a*** is the material mass.
The measurement process of physisorption involves chilling the surface of the measured powder, using nitrogen to adhere to the surface-adsorption, then taking the chilling away – leading to desorption.

Appendix B: *Materials & synthesis*

B1. Materials

Single-walled carbon nanohorns (SWCNHs) were provided by Car-bonium S.R.L. Chemicals and solvents for synthesis were obtained from Sigma Aldrich, and they were used without further purification.

B2. Mild oxidation of p-SWCNHs: Synthesis of ox-SWCNHs

Pristine SWCNHs (p-SWCNHs) were dissolved in a 4 M nitric acid solution in order to get a suspension 1 mg mL^{-1}. The suspensions were sonicated for 15 minutes to dissolve the present bundles and then stirred for three hours. This optimized time is the more suitable to obtain the optimal degree of oxygenic groups and the lowest damage on the honeycomb structure surface. The solid was then filtered and washed with distilled water until neutral pH of the washing water (ox-SWCNHs).

B3. Synthesis of Pd@TiO_2/ox-SWCNHs hybrid

The appropriate amount of MUA–protected Pd nanoparticle (Pd-MUA) was dissolved in the needed amount of Titanium butoxide $Ti(OBu)_4$, in order to get the desired ratio components. The solution of Pd@TiO_2 precursor was added dropwise to ox-SWCNHs suspension (0.25 mg mL^{-1} in EtOH) under continuous sonication. The resulting suspension of “Pd@TiO_2/ox-SWCNHs” was vigorously sonicated for 30 minutes. Finally, a mixture of H_2O (1.5 mL) and THF (13.5 mL) was added to ensure the complete hydrolysis of the Ti alkoxide. The mixture was sonicated for further 30 min and then the product was filtered, washed with MeOH/H_2O 2:1 v/v and finally with MeOH. The final materials were dried at 80 °C overnight prior to being used (Pd@TiO_2/ox-SWCNHs). A similar approach was adopted in the absence of Pd-MUA in order to obtain the corresponding Pd-free catalyst (TiO_2/ox-SWCNHs).

B4. Synthesis of Pd/ox-SWCNHs

The right amount of Pd NP precursor (K_2PdCl_4) was added dropwise to ox-SWCNHs suspension(1 mg mL^{-1} in EtOH). The suspension so obtained was kept under sonication for 15 minutes and than the right amount of $NaBH_4$ was added to the suspension. The suspension was kept under sonication for other 15minutes. The material Pd/ox-SWCNHs have been filtered and whashed two time with H_2O, and then with neat EtOH. The final materials were dried at 80 °C overnight prior to being used.

B5. NiCyclam@BIMIM/p-SWCNHs

B5.1 BMIM/p-SWCNHs

The right amount of $BMIMPF_6$ solution in anhydrous THF was mixed with p-SWCNHs suspension (1mg mL^{-1} in anhydrous THF) in order to obtain the desired composition.

After one night under stirring, the mixture was dried by vacuum evaporation. The final materials were dried at 80 °C overnight prior to being used.

B5.2 NiCyclam@BMIM/p-SWCNHs

The right amount of NiCyclam^{2+} have been dissolved in the right amount of BMIMPF$_6$ solution in anhydrous THF. The solution, so obtained have been stirred till NiCyclam^{2+} dissolution (NiCyclam@BIMIM precursor). NiCyclam@BMIM precursor solution have been added to p-SWCNHs suspension (1mg mL^{-1} in anhydrous THF). After one night under stirring, the mixture was dried by vacuum evaporation. The final materials were dried at 80 °C overnight prior to being used.

B6. t-Fe@MWCNTs

B6.1 Synthesis of Fe@MWCNTs and HCl-Fe@MWCNTs

The following synthesis has been performed in the laboratory of the Prof. Davide Bonifazi at the University of Namur. In the 180 cm-long quartz tube of a furnace setup, a 10 cm long quartz substrate was introduced in the temperature region around 1173 K, and a constant flow of 0.2 m3h¢1 of argon was used to purge the system of remaining air. Under this flux, ferrocene (5 g) was introduced in a boat and placed in a region close to 823 K. Toluene vapour was then introduced into the quartz tube of the furnace by the argon purge of 0.2 m3h¢1 for 15 min. The toluene flow was then turned off and the quartz substrate was moved to a cool zone of the 180 cm long quartz tube to allow the sample to cool to room temperature under an argon flux of 0.2 m3h¢1. The black material was then washed with ethanol to remove any residual ferrocene to give pristine Fe@MWCNT (about 2.3 g). The material was then washed with HCl to remove any external Fe or Fe oxide (HCl- Fe@MWCNT). In detail, the as-produced material (250 mg) was placed in a 1 L round-bottomed flask, and methanol (375 mL) was added. The solution was sonicated for 10 min and a 4m aqueous solution of hydrochloric acid (125 mL) was added to the flask. The mixture was sonicated for a further 10 min and the solution was stirred for 24 h at room temperature. The solution was diluted with water (375 mL) and then filtered through a 0.45 mm hydrophobic polytetrafluoroethylene filter. The resulting precipitate was then redispersed by 10 min of sonication in methanol (100 mL), filtered through the same filter, and washed with water (100 mL). This procedure was repeated twice, and the final precipitate was finally washed with few millilitres of methanol to facilitate drying. HCl- Fe@MWCNT was thus recovered as a black powder (about 220 mg).

B6.2 Synthesis of t-Fe@MWCNTs

HCl-Fe@MWCNTs (100 mg) were placed in a 500 mL round-bottomed flask and N-methyl-2-pyrrolidone (NMP, 67 mL) was added. The solution was sonicated for 20 min, p-aminophenylacetic acid (675 mg) was added, the solution was sonicated for another 10 min and diisopropylethylamine (40 mL) was added. After 10 min of further sonication, isoamyl nitrite (1.5 mL) was added slowly and the reaction mixture was stirred at 363 K for 20 h. The solution was cooled to room temperature and was filtered through a 0.45 mm hydrophobic polytetrafluoroethylene filter. The precipitate was redispersed by 10 min of sonication in 100 mL of ethyl acetate and filtered through the same filter. This step was repeated two additional times and the final precipitate was dispersed in 100 mL of methanol by 10 min of sonication, water (200 mL) was added and the suspension was filtered through the same filter. Two additional washing steps with water (50 mL) were performed. The precipitate was finally washed with few millilitres of methanol to facilitate drying. About 85 mg of t-Fe@MWCNT was thus recovered as a black powder.

B7. g-N-CNHs

B7.1 Ox-CNHs

100 mg of p-CNHs were sonicated in 100 ml of HNO_3 (69 %) for 15 min. The resulting dispersion was stirred for 3 h at 35 ^oC. Cold water (200 ml) was then added to the reaction and the crude was filtered through a Millipore membrane (JHWP, 0.45 µm) and washed with deionized water till neutralization of the washings. The black powder was finally washed with MeOH and dried with Et_2O affording 99 mg of ox-CNHs.

B7.2 Ox-CNHs@PDA

Dopamine hydrochloride (400 mg, 2.11 mmol) and ox-CNHs (10 mg) were ultrasonicated in deionized water (40 ml) for 30 min. Tris buffer pH 8.5 (10 ml, 50 mM) was then added and the reaction was stirred for 16 h at room temperature. The crude was filtered through a Millipore membrane (JHWP, 0.45 µm) and washed with cycles of ultrasonication/filtration in water (2 x 50 ml) and ethanol (2 x 50 ml). The black product was rinsed with Et_2O and dried under vacuum affording 50 mg of ox-CNHs@PDA.

B7.3 g-N-CNHs

Ox-CNHs@PDA (140 mg) were annealed under Ar for 3 h to afford g-N-CNHs (92 mg). No further purification was required.

B8. Ox-SWCNHs@CeO_2

ox-SWCNHs@CeO_2 structures were prepared by a sol-gel method. The solution of precursor Ce^{4+}tetrakis(decyloxide) was added dropwise to ox-SWCNHs suspension (0.25 mg mL^{-1} in EtOH) under continuous sonication. The mixture was kept under sonication for 30 min. A mixture of H_2O (1.5 mL) and THF (13.5 mL) was added to ensure the complete hydrolysis of the CeO_2 precursor, and the mixture was sonicated for an additional 30 minutes. The solids were then recovered by filtration and washed with EtOH/H_2O 2:1 and one time with pure EtOH. The final materials were then dried at 80 ◦C overnight prior to being used.

Appendix C: *Apparatus*

C1. Electrochemical apparatus

All electrochemical measurements were performed on a Autolab 302 N electrochemical workstation (Metrohm, The Netherlands) at room temperature, using a conventional three-electrode system composed of a modified glassy carbon electrode(GCE; CH Instrument, CH 104) as a working electrode, a platinum wire as an auxiliary electrode and a Ag/AgCl (3 M NaCl) (CHInstrument, CH 111).

C2. Thermogravimetric apparatus

Thermogravimetric analyses (TGA) of approximately 1 mg of each compound was recorded on a TGA Q500 (TA Instruments).

C3. Raman spectroscopy apparatus

Raman spectra were recorded with an Invia Renishaw microspectrometer (50) equipped with He–Nelaser at 532 nm.

C4. FT-IR spectroscopy apparatus

Fourier Transform Infrared Spectroscopy (FTIR) was measured in a System 2000–Perkin Elmer spectrometer in an optical range of 370–4000 cm^{-1}at a resolution of 4 cm^{-1}.

C5. Transmission Electron Microscopy apparatus

Transmission Electron Microscopy (TEM) measurements were per-formed on a TEM Philips EM208, using an acceleration voltage of100 kV.
High resolution TEM (HRTEM) were acquired on a JEOL 2200FS microscope operating at 200 kV, equipped with an Energy Dispersive Spectrometer (EDX), in-column energy (Omega) filter, and High-Angle Annular Dark-Field (HAADF) detector.

C6. Atomic Force Microscopy apparatus

Atomic Force Microscopy(AFM) measurements were performed using a Nanoscope V micro-scope (Digital Instruments Metrology Group, model MMAFMLN)in tapping mode in air at room temperature, using standard μmasch®SPM probe (HQ:NSC15/AIBS) with tip height 12–18 μm, cone anglen <40◦(Resonant frequency 325 kHz, force constant of ∼40 N m−1). Image analysis has been performed with Gwid-dion software.

C7. N_2 Physisorption apparatus

N2 physisorption at the liquid nitrogen temperature was collected using a Micromeritics ASAP 2020 analyzer. Before analysis, the samples were degassed at 150◦C for at least 12 hat a pressure lower than 10 mHg. The specific surface area of the samples was calculated applying the BET method. Pore size distributions were calculated applying the BJH method to the adsorption branch of the isotherms.

Pubblications list:

1) M. V. Bracamonte, M. Melchionna, A. Stopin, A. Giuliani, C. Tavagnacco, Y. Garcia, P. Fornasiero, D. Bonifazi, M. Prato
Carboxylated, Fe-Filled Multiwalled Carbon Nanotubes as Versatile Catalysts for O_2 Reduction and H_2 Evolution Reactions at Physiological pH. *Chem. Eur. J.* **2015,** 21, 12769 – 12777 doi:10.1002/chem.201501144

2) M. I. Lucio, F. Pichler, J. R. Ramirez, A. de la Hoz, A. Sanchez-Migallon, C. Hadad, M. Quintana, A. Giuliani, M. V. Bracamonte, J. L. G. Fierro, C. Tavagnacco, M. A. Herrero, M. Prato, E. Vazquez
Triazine-Carbon Nanotubes: New Platforms for the Design of Flavin Receptors. *Chem. Eur. J.*, **2016**, 22, 8879-8888, doi: 10.1002/chem.201600630

3) M.V. Bracamonte, M. Melchionna, A. Giuliani, L. Nasi, C. Tavagnacco, M. Prato, P. Fornasiero.
H_2O_2 sensing enhancement by mutual integration of single walled carbon nanohorns with metal oxide catalyst: The CeO_2 case. Sensor and Actuators B, 2017, 239, 923-932, doi: 10.1016/j.snb.2016.08.112

Acknowledgements

PhD has great importance for who is in love with science, it gives you the opportunity to study, ask you questions and then find solutions, using the own creativity and imagination. Sometimes the path is harder, you need several experiments and papers to find a new path with less obstacles, and then everything appears newly clear. Who has not a PhD cannot understand it. Research is exciting, can make you feel part of a great community and at the same time can hurt you when the lights of the lab are turned off, and you have not still an answer to what is happening in your solution, and go at home thinking to it, sometimes alone, sometimes with your lab-mates. This experience has been for me very important, and for this I want to thank my supervisor Professor Maurizio Prato, whom allowed me to join his group and gave me all the tools to carry on my research project, thanks to him, I'm closing this part of my career with a huge baggage full of new knowledge and also friends, and for this the acknowledgements will never be enough.

First of all, I want to thank Dr. Michele Melchionna. I worked very close with him, and all these three years would not be the same without him, he taught me so much about science and life, and even if sometimes we were in disagreement about them, I could count every time on him for everything, and for me it has been very precious.

I want to say thanks to Dr. Victoria Bracamonte, I have worked very close with her, and she taught me so much about science, she always supported me even when we were in disagreement, she always always offered her friendship, and I am grateful to her for it, because she supported me always, even when she is back in Argentina.

I want to say thank to Professor Claudio Tavagnacco, for his help during these three years, for his kindness and goodness, his friendship and his pleasantness, he brought every time a smile, even when the days were blue for everybody, Thank you!

I want to say thanks also to Joey and Dr. Manuela Bevilacqua for their friendship and support.

I want to thank all the people of my research group, because they tolerated me even if I'm not the best person with whom share an office and sometimes a lab. In particular, I want to say thank to Dr. Susanna Bosi, because she had always so much patience with me and she was always friendly and nice with me. I want to say thanks to Dr. Luigi Feruglio, I appreciated a lot being one his "fumetta friend", and I loved disturbed him on skype every time that I could, I want to say thanks to Dr. Zois Syrgiannis for his friendship even when I said sentences without sense at the end of the day, and for the times when with Francesco Rigodanza he bantered me because it was necessary. I want to say thank to Francesco Rigodanza because he listened to me every time I complained about the life, because he has been the best roommate that I could hope to have during the physical chemistry school in Otranto, because he left me the room every morning to make yoga and he never complained about the time that I spent in the bathroom; for his passion for "Obsession" song, and for his great help with Advanced Organic Chemistry course, it has been really fun.

I want to thank Daniel Iglesias-Asperilla because he said my name wrong during the last workshop of the PhD students (I'm kidding), because he has been the best lab and office mate of the world! He tolerated me when I used to listen to the music with headphones so loud that he also listened to my music, when I typed on whatsapp for more than one message because I was not able to turn off the tone of the fingerboard, for all the jokes

with Luigi, and more than everything, because he and Caroline helped me after the party of the first year. Really thank, without them, maybe I would not have found my house even after one month. I want to say thank to Dr. Caroline Hadad for her friendship, for her help and her support every time, in particular when Vicky left, I very appreciated it. Furthermore, I want to thank professor Paolo Fornasiero and his research group for their scientific support and in particular Alessandro Beltram for his patience with me, and the all the time spent chatting in lab. I thank professor Marcella Bonchio and professor Andrea Sartorel from Padua University for their scientific support and kindness.

Besides the lab, a fabulous person I found as my flat mate, Alessia Bassi, and I think that Trieste will remind me always our friendship. She has been very precious to me during my PhD because every day I knew that she was waiting for me to share a cup of hot tea to spend the rest of the day chatting about the day and to confide everything. I enjoyed Trieste with her. Thank you Alessia!

I want to say thanks to my family, because they are my strength and have supported me in every my decision, my parents because without them nothing could be possible, my brothers and Poliane and my little nephew Maria Antonia for the suggestions, the long aperitifs, the squabbles and all the time spent together.

A very big thank goes to Claudio, best friend, boyfriend, and companion of all my best trips, from India to Iceland, passing from Spain or easily from Venice, because he is able to make our life full of adventure in Pomarolo too, because he shares my craziness and he appreciates me also when I’m angry with the world, and after 10 years he is still here. Thank you!

I want to say thanks to all my friends because they never left me alone and accompanied me till this day. Thank you to everybody!